STATISTICAL DYNAMICS OF MULTICOMPONENT QUASI-TWO-DIMENSIONAL COLLOIDAL SYSTEMS

A Dissertation

Presented to the Faculty of the Graduate School

of Cornell University

in Partial Fulfillment of the Requirements for the Degree of

Doctor of Philosophy

by

John Carl Mergo III

December 2017

STATISTICAL DYNAMICS OF MULTICOMPONENT
QUASI-TWO-DIMENSIONAL COLLOIDAL SYSTEMS

John Carl Mergo III, Ph.D.
Cornell University 2017

Colloidal microparticles, particles large and slow enough to be imaged easily using optical microscopes yet small enough to be thermalized in a solvent such as water, provide a unique window into the thermodynamic processes behind phase transitions. Specifically, microparticles can be uniquely identified and imaged throughout the field of view for the duration of an experiment, allowing visualization of both the evolution of the sample as a whole and the activities undertaken by each particle during this evolution. In addition to the high spatial and time resolution of experiments, the ability to control the interparticle interaction in these systems via modification of the particle shape, surface, and the suspending solvent make microparticles an extremely attractive system for modeling the dynamics of crystallization and melting.

In this thesis, I report the results of two experiments using colloidal microparticles, both containing surprising results. Chapter 4 reports on the first recorded instance of catalysis of crystal layer growth via slight size-mismatching colloidal particles, while Chapter 5 describes the dynamics of a nonintuitive finding whereby a high-density facet of a crystal melts faster than its lower-density counterpart. Together, these experiments demonstrate the importance of considering statistical dynamics during phase changes as well as highlight the utility that colloidal systems bring to the table for investigating dynamics during phase changes.

BIOGRAPHICAL SKETCH

John C. Mergo III was born in a suburb of Chicago on November 3, 1985 to John C. Mergo Jr. and Diane Mergo. In second grade, he was promptly transported to Chillicothe, Ohio, where he learned meek midwestern habits, such as being nice, bottling his anger, and taking a surprisingly strong stance that soft drinks are called "pop."

John had his first experience with thermal physics when he was thirteen years old. John lived on a farm, and his job was to burn the weekly garbage. John was so good at his job that he was not only able to burn the entire garbage pile, but also burn down a nearby barn packed full of hay *without even trying*, as he had left the fire unattended to go play video games. John's punishment was a combination of disappointment and disbelief from his family and the chore of having to wake up to check the remains of the hay barn every hour to make sure the fire did not reignite. The physicist in him found the flame jets shooting from the smoldering pile quite beautiful at night, and the engineer in him wondered if automating the task of checking the fire every hour would ultimately save time, allow for the collection of a more dense data set, and be less prone to human error.

John went on to graduate from The Ohio State University with a B.S. in Physics, working with Professor Paul Berger (ECE) on RITDs and his mentor, Professor Robert Perry (Nuclear Theory Group) on Similarity Renormalization Group theory. John then went to graduate school at Cornell in Applied and Engineering Physics. His interest in thermal physics still strong, he perfected the art of smoking meat with Brian Leahy. He also joined the Itai Cohen lab, interested in the statistical physics of colloidal crystallization. Due to various unfortunate circumstances surrounding illnesses in his family and his fiancée,

he took a leave of absence from Cornell starting in 2015[1]. During his leave of absence, he co-founded a branch of a small programming company working internationally and started a family, introducing Ava Jeanette Mergo and Io Rita Mergo to the world.

But, at night, this mild-mannered, midwestern system administrator and programmer had an alter-ego: also John Mergo. With shades drawn, he often worked tirelessly through the night to complete the research project that was left unfinished when he started his leave. This dissertation is the result of ~~countless all-nighters~~ 306 all-nighters, at an average of two per week between January 2015 and October 2017. Unlike most all-nighters, where a looming deadline creates a situation where one needs to sacrifice sleep to finish on time, these were a natural consequence of attempting to think while having two children under two years old in the house. John still cannot believe how rare quiet moments are between 5 AM and 8 PM.

Given the extra year spent awake, John has aged phenomenally.

[1]His grandmother, Rita, passed away during his leave. This dissertation is dedicated to her.

To my family, Dr. Mergo, Dr. Mergo, Dr. Mergo, and Dr. Mergo.

To my incredibly patient and talented wife, Dr. Mergo.

To my daughters, Ava[13] and Io.

To Rita.

ACKNOWLEDGEMENTS

A huge number of people have helped along various stages of my time in graduate school at Cornell. While this is by no means an exhaustive list of people who have contributed to my work, my family, or my sanity, I feel that it is important to name a few of these people here.

First and foremost, I have to thank my wife, Dr. Megan Mergo, who took on many (read: all) of the responsibilities surrounding our home and children during my three-year leave-of-absence from graduate school. Without her, I would never have been able to pull off working a full time job, switch gears, and work nights as a full-time researcher. This is not to say that she only handled the domestic aspect of our lives – she shouldered this responsibility in addition to her full-time job. Thank you for pulling me out of bed every time I wanted to give up, and thank you for telling me to go to bed on the nights that I had been awake for 72 hours. I will probably never be able to make this up to you.

On the subject of my three-year leave of absence, I would like to thank Aperion Information Technologies (and specifically, Mark Comins) for seeing my potential as a business leader and scientist and trusting me to co-found a branch of the company in Ithaca while on leave from Cornell. This was a large leap of faith for a small business. I am thankful for the support, as it enabled me to take on a challenging full-time job in a field I am familiar with while remaining close enough to Cornell to finish my Ph.D.

I especially would like to thank Brian Leahy, who taught me how to dress properly. I deeply appreciate his willingness to come out to my home office and talk physics and programming, every weekend, without fail. Most importantly, Brian helped me perfect my knowledge of the field of ”applied thermal physics” via experiments on low-level heating of large slabs of meat in the presence of

solid aerosols derived from wood. During my leave of absence, Brian was the strongest constant connection I had to Cornell.

I would like to thank Leif Ristroph and Matt Warkentin, who showed me that being a grad student and being yourself were not mutually exclusive. Without the guidance from these two elder graduate students, I likely would have been unable to navigate my life as a graduate student. Along that vein, I would like to thank Dustin Madison, Zach Lamberty, Lena Bartell, Sam Whitehead, Lauren McCloud, and Jessie Killian.

Chelsi Oliver, a recently graduate in Pre-Law from Ithaca College, played an instrumental role in granting my wife and I extra time to work throughout my leave of absence. We hired her to help take care of our one-year-old daughter, Ava, to buy us some extra time for me to finish a paper and this dissertation. Her patience and extreme reliability allowed me to count on having a consistent minimum amount of time to spend on science. Furthermore, her talents in early childhood education lead to my daughter learning sign language, shapes, colors, the alphabet, and how to read a few key words before the age of two.

I would like to thank Stephen "Squade" Doucette for constantly reminding me that I should probably forget about becoming a pro gamer and instead focus on finishing my Ph.D.. Stephen often kept me company on my all-night science sessions, always willing to take me up on my offer to play games while taking a break from my project. More importantly, he was a huge help as a sounding board for my presentations and explanations of my projects.

Finally, I would like to thank Professor Itai Cohen for the opportunity to research in his lab. He has set up a open, collaborative environment within his own group that allows new researchers to thrive via forging personal and professional relationships between one another. I would especially like to thank

him for his ideas on clear scientific communication – a topic on which I regularly needed guidance.

TABLE OF CONTENTS

Biographical Sketch . . . iii
Dedication . . . v
Acknowledgements . . . vi
Table of Contents . . . ix
List of Figures . . . xi

1 Introduction **1**
1.1 Depletion Interaction . . . 2
1.2 Notes to the Reader . . . 5

2 Instrumentation **7**
2.1 Sample Containment . . . 7
2.1.1 Basic Cleaning . . . 8
2.1.2 Constructing Basic Sample Chambers . . . 10
2.2 Solvent and Microparticles . . . 11
2.2.1 Microparticles . . . 12
2.2.2 Solvent . . . 12
2.3 Issues with $C_{12}E_6$ . . . 16
2.4 The Microscope . . . 18
2.4.1 Standard Thermal Control . . . 18
2.4.2 Improved Thermal Control . . . 19

3 Data Analysis **27**
3.1 Introduction . . . 27
3.2 Analysis . . . 29
3.2.1 Particle Sizes . . . 29
3.2.2 Bond Orientation Order Parameter ψ_6 . . . 33
3.2.3 Perimeter Particles . . . 36

4 Catalysis of Single-to-Double Layered Crystal Growth in Bidisperse Colloidal Suspensions **42**
4.1 Abstract . . . 42
4.2 Introduction . . . 42
4.3 Experimental Methods . . . 46
4.4 Results . . . 47
4.5 Discussion . . . 52
4.6 Appendix: Supplemental Information . . . 55
4.7 Appendix: Simulating Particle Promotion . . . 57
4.7.1 Model . . . 57
4.7.2 Random Promotion . . . 59
4.7.3 Comparison to Multinomial Model . . . 59
4.7.4 Promotion at Large Particles . . . 63

4.7.5 Promotion at Crystal Edges . . . 64
4.7.6 Promotion with Bond-Breaking . . . 65

5 Melting on Square and Triangular Lattices 68
5.1 Experiment . . . 68
5.2 Theory . . . 69
5.2.1 Bond Energies for Interstitial Particles . . . 70
5.2.2 Diffusion Path on Different Lattices . . . 74
5.3 Patterned Substrates . . . 78
5.3.1 Background . . . 78
5.3.2 Problems with Previous Process on New E-Beam . . . 81
5.3.3 Modifications to Fabrication Process . . . 82
5.4 Conclusion . . . 83

6 Conclusion 85

A Appendix: Code Snippets 87
A.1 Fast Pair Correlation Function, $\mathbf{g}(\mathbf{r})$ . . . 87
A.2 Fast Orientational Order Parameter, ψ_6 . . . 90
A.3 Distance Matrix . . . 91
A.4 Connectivity Matrix . . . 93

Bibliography 94

LIST OF FIGURES

1.1 Schematic of the depletion interaction. Black particles represent large colloidal particles that are imaged during our experiments, approximately 1.0 µm in diameter. Red "depletant" particles are much smaller, about 30 nm in diameter. The smallest possible separation between the colloids and depletant is represented by the blue halo around the colloidal particles. This is called the depletion zone. (**A**): When colloidal particles are separated by distances larger than the diameter of a depletant particle, the depletion zones do not overlap, and the particles do not interact. (**B**): If the colloidal particles happen to be close enough that their depletion zones overlap, the particles feel a net pressure pinning them together, introducing a small attraction between colloids. . 3

2.1 Phase diagram for SDS-Water mixtures at a given temperature. In these experiments it is important to remain in the micellar phase, which occupies the upper-left region of this plot. Reprinted from [30]. 14

2.2 Phase diagram for $C_{12}E_6$-Water mixtures at a given temperature. Remaining in the micellar phase with this surfactant requires keeping the temperature below 45 °C at the modest 2.0 wt% used in our experiments. Reprinted from [30]. 15

2.3 Custom copper water block used for precise control of the air and surface temperature surrounding a sample. Glass slides are mounted horizontally across the center hole, allowing the objective lens to come in contact with the sample from underneath and transmitted light to enter from the top. Water is pumped in and out through the holes in the top-left of the block, traveling along three trenches running along the outer portion of the block. The block is sealed from above with a plastic cover (not pictured). 20

2.4 Custom aluminum resistive heating block used for directly controlling sample temperature from above. The through-hole allows all light from the condenser to reach the sample. Red wires lead to four buried resistors, equal in resistance with a total device resistance of 40 Ω. Resistor cavities are filled with thermal compound. The black IC in the center of the image (Texas Instruments LM35) is the temperature sensor, which is attached to the aluminum body with thermal compound and epoxied in place. The dimensions of the heating element are 25.0 mm × 25.0 mm × 12.5 mm. 21

2.5 Repurposed ATX computer power supply. Molex connectors were stripped and equal voltage outputs were gathered across rails. Wires were fed into a breakout chassis and terminated at their respective colors. 22
2.6 Image of the final prototype heater, sensor, and PID control device. The Arduino microcontroller, which handles the temperature readings and PID controller, is seen on the right side of the image. The remaining electronics on the left handle the rest of the major tasks: switching the heater output, supplying a 5 V line for the thermometer, activating a power LED when the external power supply is on, and providing a reference voltage to set the range of the microcontroller's temperature measurements. 23
2.7 PID-controlled heating element temperature as a function of time. The temperature controller was set to a target temperature of 36 °C, with an ambient temperature of 17 °C. (**top**) After a relatively short temperature rise time of 18 s versus air circulation, the heating block temperature stabilizes at the target temperature by 40 s. (**bottom**) Oscillations about the target temperature under the desired limit of ±0.1 °C is achieved, with maximum excursions from the target rarely exceeding ±0.05 °C. 24

3.1 Simple measurement technique to extract particle sizes: Here, we measure across the interior of a crystal composed of 1.0 µm particles to obtain an average particle size. The red line spans 13 small particles and is 173.5 px long in the original image, resulting in an average particle diameter of 13.3 px. 30
3.2 Pair correlation function, $g(r)$, between first peak and first split of second peak. This measurement considers only the positions of small (1.0 µm) particles in an image of a mixed-phase system consisting of gaseous and crystalline regions of binary microparticles. Notice the first peak is centered around 13.3 px, which is consistent with the particle diameter measured directly in Figure 3.1. (**Inset**): Full $g(r)$, out to $r_{max} = 200$ px. 32
3.3 Crystal and amorphous islands with ψ_6 values overlaid on each small particle residing on the substrate. Red: $\psi_6 > 0.25$, Yellow: $\psi_6 > 0.5$, Green: $\psi_6 > 0.75$. 35
3.4 Crystal islands defined using depth-first search. Colors are assigned randomly to each cluster. Notice that the large particles consistently interfere with island edges, creating pockets and jagged edges. 37

3.5 Example of adding a particle to unique positions at the edges of a triangular lattice. Blue or black particles represent "test" particles added to the lattice. Black lines represent paths to a set of the particle's nearest neighbors, NN_1. A red line leads from NN_1 to their nearest neighbors, NN_2. Drawing the links to the nearest neighbor sets for each test particle begins to reveal a pattern: an acceptable edge particle participates in two closed traversal loops. Particles without a second traversal path (e.g., the dark particle) are excluded from edges, even though they may temporarily share the same lattice orientation. 39
3.6 Perimeter particles found via breadth-first search of particles with between 2 and 5 nearest neighbors. Compare to outermost particles in Figure 3.4. This method tends to include edge particles with low ψ_6 due to neighbors with a single bond to the crystal and tends to eliminate issues with single particle bridges between crystal islands. 40

4.1 Images of monodisperse (**A**) and bidisperse (**B**) samples of crystallizing polystyrene microparticles 20 hours after nucleation. Particles on the second layer appear white, while particles in the bottom layer appear dark. Scale bar is 10 µm. 44
4.2 Measurement of the counts of particles in various states in the sample (Left axis, black). The number of particles in the bottom (N_1) layers are indicated by the squares. The number of particle in the top (N_2) layers are indicated by the diamonds. The number of unblocked perimeter particles (N_{1P}) are indicated by the closed circles. The number of gaseous particles promoted off of the sample floor (N_{2G} are indicated by the stars. Measurement of the growth rate of the top layer as a function of time is indicated by the open circles (Right axis, red). A fit using the simple model described in Eq. 4.1 is overlaid as a sold red line. 47

4.3 Probability distributions characterizing the separation distance between N_{2G} particles and the nearest large particle in experiments and simulations during the onset of bilayer growth acceleration. (**A**): Probability of finding a promoted particle a normalized distance r/r_s from a large as measured in the experiment. (**B**): Results of Monte Carlo simulations that randomly place particles into N_{2G} based on various rules: Particles are promoted randomly, avoiding promotion from crystalline regions (red), or promoted at the edge of a randomly selected large particle and allowed to diffuse unhindered for 30 seconds (purple). Once promoted at a large particle, a random bond breaking time, t_b, is assigned, sampled from an exponential distribution with a mean of 30 seconds (green). In this case, promoted particles diffuse unhindered for $1/f - t_b$, the remaining time between frame captures. Error bars for the simulations are the width of the bin outlines. (**C**): Cumulative distribution functions for simulations and experiment. 51

4.4 Visual evidence of solute-facilitated promotion. (A) Contrasting images of monodisperse and bidisperse crystal edges and grain boundary, capturing the disordered nature of the boundary in bidisperse samples. Red circles mark large particles. (B) Four representative images of the promotion of small particles at the crystal boundary in the presence of a large particle. Green arrows highlight particles undergoing a promotion event. (C) Time-series highlighting the promotion and subsequent diffusion of a corner particle in the presence of large particles. The blue arrows mark the location of the same particle through the first two frames, while the dashed line in the third frame denotes the displacement of the same particle. 52

4.5 Time-lapse images of the crystallizing mixtures of binary, attractive colloidal hard spheres. Dark particles reside on the glass sample chamber. White particles are in focus, about 1 m above the black particles. At 0 minutes, we see a 2D gas of sedimented particles. At 400 minutes, the nucleation and growth of the monolayer crystals of small particles has completed, with the larger particles displaced to the periphery of the islands. In addition, we observe the nucleation and growth of a second crystal layer as indicated by the white particles. The top layers continue to grow through 800 minutes, while the exposed monolayer regions shrink. The large particles have formed monolayers of their own species at the crystal edges. The final panel shows the final configuration of the system after 1200 minutes. We see that all islands throughout the sample chamber consist of two full layers. Finally, we find that even the largest monolayer island in the field of view (dashed box) evaporates by the end of the experiment. Scale bar is 10 µm. Best viewed digitally. 56
4.6 Example frame of data: frame 201. **Red**: Small particles on substrate. **Blue**: Large particles. **Green**: Gaseous promoted small particles. **Yellow**: Small particles on top of a monolayer. **Magenta**: Small particles in a second-layer crystal. 58
4.7 Illustration of a distance transform of **L**. Each pixel is given a value equal to the distance to the nearest large particle. Crystalline areas (large, dark purple regions) are overlaid with a distance value of -1. Axes are in units of pixels, which has been supersampled by a factor of ten from the original image. Separation distance increases as the image transitions from purple to blue to yellow. 60
4.8 Result of simulating random placement of **G** and measuring the minimum distance to the nearest large particle across 10 minutes in time, repeated 10^5 times for each frame. **Inset**: Cumulative distribution function. 61
4.9 Result of directly measuring the probability to find a particle at a given separation from the nearest large particle by assuming a multinomial distribution with probability weights given by the normalized counts of pixels at each distance from Figure 4.7, taken across ten minutes of time. **Inset**: Cumulative distribution function. Notice the CDF of the measurement (red circles) and the simulation (black points) line up nearly exactly. 62

4.10 Example of simulation results for a single frame (210) assuming that particles must begin their diffusion at the edge of a crystal. Note that the diffusion constant in this run is extremely small, equating to a diffusion length of 6 px between frames. Thus, promoted particles are highly localized at crystal boundaries. The experimentally observed strong peak (20% at contact between large and small particles) cannot be reproduced with this promotion rule. 64

5.1 Melting time for particles in square versus triangular lattices. The number of particles in the triangular lattice is plotted with thin vertical lines, while the number of particles in a square lattice is plotted with squares. The plot illustrates that it takes about 3 to 4 times longer to melt particles in a square lattice than it does for triangular lattices. 69
5.2 Nearest neighbor count for particles on the edge of a facet of hexagonal symmetry. Each particle has three nearest neighbors contributed from the underlying crystal layer, while corner particles have three neighbors in-plane and edge particles have four. Thus, corner particles have six nearest neighbors, and edge particles have seven. 70
5.3 Nearest neighbor count for particles on the edge of a facet of square symmetry. Each particle has four nearest neighbors contributed from the underlying crystal layer, while corner particles have two neighbors in-plane and edge particles have three. Thus, corner particles have six nearest neighbors, and edge particles have seven, just like in the hexagonal lattice. 71
5.4 Example of removing a particle from the edge of a triangular lattice. Depending on the stacking orientation, removing a particle requires breaking either five or six bonds, as denoted by the number inside the particle being removed. Moving an edge particle always breaks four bonds in-plane (teal) and either one or two bonds with the substrate (purple). 72
5.5 Example of removing a particle from the edge of a square lattice. Moving an edge particle always breaks three bonds in-plane (teal) and either two bonds with the substrate (purple). 73
5.6 Post-processed image showing the diffusion paths of nine surface adadtoms on a triangular lattice after five minutes. The 10th particle on the far bottom-right, diffuses out of the frame and is not tracked. The paths illustrate that it is very rare for a particle to diffuse out of its trough and thus over an underlying particle to a new interstitial site. Particles are 1 μm in diameter. 74

5.7 Observational evidence of preference for corner melting. Image from the early stages of an experiment on melting a 52-particle hexagonally-symmetric crystal facet composed of 1.0 μm particles. 75
5.8 Number of bonds broken via moving corner particles. Moving a corner particle on either lattices requires breaking only four bonds. Furthermore, removing either a corner or edge particle can create up to two new corner particles, denoted by an "X". Particles whose bonds are broken in-plane with the removed particle are colored teal, while substrate particles that lose bonds are colored purple. 76
5.9 Image of patterned glass substrate after being cleaned and reused multiple times. Patterned circles are 1 μm in diameter. A clear amorphous blob of stuck material can be seen inhibiting access to patterned regions of the sample, effectively rendering our device useless. This is particularly bad, because the glass substrates were developed for the express purpose of being reusable for many experiments. 79
5.10 TOP: Optical transmission micrograph of arrays of 1.0 μm holes in PMMA on a glass substrate. Each square is 100 μm x 100 μm. In the top row, holes are arranged in a triangular lattice. In the bottom row, holes are arranged in a square lattice. Dosage is set to 100 $\mu C/cm^2$ at the top row of the image and decreases by $\mu C/cm^2$ for each subsequent row. Notice that the pattern appears patchy at lower exposures and is destroyed at higher exposures. BOTTOM: Close-up of the central patterns from above. 80
5.11 Reflected light micrograph of high beam current region of patterned substrate. Much of the feature layer has been destroyed. Colors arise from the change in PMMA thickness. Tree-like branching is similar in appearance to Lichtenberg figures, characteristic of damage due to electrical discharge. Small, colored circles roughly in the image center are 1.0 μm in diameter. 81
5.12 Successful results of new cleanroom process. LEFT: SEM image of triangular and square lattices made from altered E-Beam lithography recipe that adds a conducting layer onto the PMMA layer. RIGHT,TOP: Optical image of square lattice. RIGHT,BOTTOM: Optical image of triangular lattice. LEFT,BOTTOM: Dosage sweep over the same parameters used in Figure 5.10. Notice the absence of arcing damage in the patterned regions. 83

CHAPTER 1

INTRODUCTION

Throughout this dissertation, colloids are assumed to be roughly micron-sized solid particles in a fluid solvent. These particles are small enough to behave thermally, but large and slow enough to be imaged with optical microscopes. This makes colloidal systems quite attractive for researching atomic or nanoscale processes that may be too fast to view otherwise. Furthermore, the size, shape, interaction potential, and concentration of particles can be controlled quite precisely. These advantages in imaging and tunability are the core ideas behind viewing colloids as "model atoms."

Even the simplest of colloidal systems, the hard-sphere system, has interesting phase behavior of its own. Hard spheres are assumed to be non-interacting unless they come into contact, where they experience an infinitely strong repulsive potential, preventing them from interpenetrating. These systems can crystallize despite the lack of any attractive or long-range repulsive interaction simply due to volume fraction alone[62, 53].

It is important to remember that colloids are not atoms. This simplest colloidal suspension, hard-sphere particles, has no atomic counterpart. The fact that colloidal system are not completely analogous to atomic systems must be kept in mind when discussing the suitability for using a colloidal system to model a process. Attractive interactions, if they are present, usually extend only to nearest-neighbors in a lattice. The bond angles are restricted to the 60° of a hexagonally close-packed system, although recent research has produced other interesting arrangements[68]. The strength of the interaction is usually on the order of k_BT, or 1/40 eV, whereas binding energies in atomic crystals are on the

order of 1 eV. Trying to use colloids to model the specific material properties of a given atomic or nanoscale system is likely to be an unrealistic undertaking. While being a viable option for modeling some atomic and nanoscale processes with careful planning, the real power of colloidal systems is that they allow us to watch the evolution of a statistical mechanical system with high spatial and temporal resolution, giving us a window into fundamental statistical physics problems.

In the experiments described in this dissertation, we observe crystallization and melting at much lower volume fractions than those required to crystallize hard spheres. To enable crystallization at such volume fractions, an interaction between particles must be present. We induce an attractive interaction between colloidal particles by the introduction of a secondary species of particles. This interaction is called the depletion interaction.

1.1 Depletion Interaction

Colloids in a suspension with a second, smaller particle species experience a fleeting net attractive interaction when the larger particles are close enough that the smaller particles cannot fit between them. This is called the depletion interaction, as described in [4]. A schematic of the interaction is depicted in Figure 1.1.

The strength of this interaction depends on the concentration of depletant particles, as well as the sizes of both the colloids and the depletant spheres,

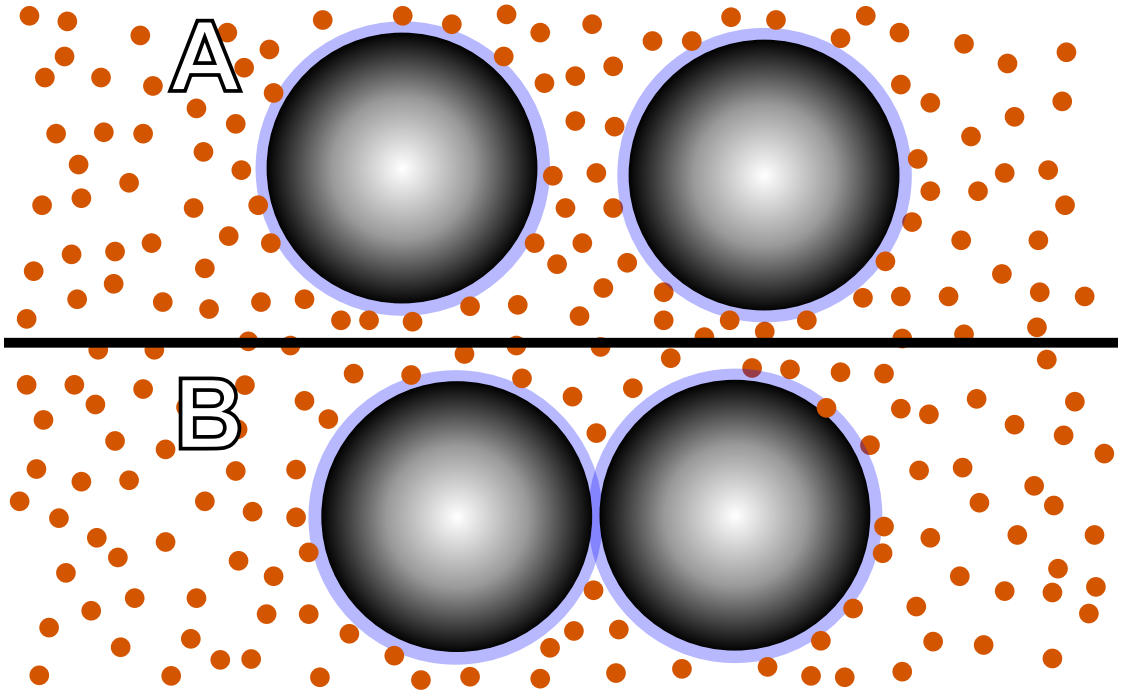

Figure 1.1: Schematic of the depletion interaction. Black particles represent large colloidal particles that are imaged during our experiments, approximately 1.0 µm in diameter. Red "depletant" particles are much smaller, about 30 nm in diameter. The smallest possible separation between the colloids and depletant is represented by the blue halo around the colloidal particles. This is called the depletion zone. (**A**): When colloidal particles are separated by distances larger than the diameter of a depletant particle, the depletion zones do not overlap, and the particles do not interact. (**B**): If the colloidal particles happen to be close enough that their depletion zones overlap, the particles feel a net pressure pinning them together, introducing a small attraction between colloids.

such that

$$U(h) = \begin{cases} -PV(h) & 0 \le h \le \sigma \\ 0 & h > \sigma, \end{cases}$$

where $P = nk_BT$, n is the bulk concentration of the depletant spheres, and $V(h)$ is the overlap volume of two spheres with edge-to-edge separation h. Notice $P = nk_BT$ is commonly known as the ideal gas pressure, meaning that this interaction is modeled as the pressure of an ideal gas of depletant particles colliding with the surfaces of the colloidal microspheres. The overlap volume between two spheres of equal size is equal to

$$V(h) = \frac{\pi}{6}(\sigma - h)^2(3R + \sigma + h/2),$$

where R is the radius of the colloidal particle, and σ is the diameter of a depletant particle.

In Chapter 4, we introduce a depletion interaction between two spheres of unlike sizes. The overlap volume, $V(h)$, can no longer be assumed to be the overlap volume between two equally-sized spheres. $V(h)$ can be found through the use of a more general equation describing the intersection between two spheres:

$$V(R, r, d) = \frac{\pi}{12d}(R + r - d)^2(d^2 + 2dr - 3r^2 + 2dR + 6rR - 3R^2),$$

where R and r are the radii of the large and small colloidal spheres[50, 14], *including* the additional depletion radius (i.e., $R \to R + \sigma/2$, $r \to r + \sigma/2$). d is the center-to-center separation distance between the two colloidal spheres such that $d = R + r + h$, with $0 \le h \le \sigma$, as before.

1.2 Notes to the Reader

The purpose of this thesis is twofold. First and foremost, it provides a full description of two of the major projects on colloidal crystallization that I have worked on while in the Cohen lab. But, perhaps equally importantly, it serves as a manual for reproducing experiments on two-dimensional colloidal crystals using a depletant to introduce attractive interactions. To this end, I have created Chapter 2 and Chapter 3 as an expanded introduction, outlining the domain knowledge and caveats for simple but critical tasks, such as steps needed to create samples that won't "die" after a short time on the microscope, how to better control the microscope's environment, how to determine the concentrations of surfactant to use in experiments, and how to reproduce key measurements in a set of featured particles. I further describe improvements to many of these techniques, which ultimately enabled me to perform and complete the experiment described in Chapter 4.

Although these seem like standard lab procedures to have on file, many of these topics and techniques were passed on to me through hands-on experience, with no documented procedures to follow, at a time when these techniques were commonly used by multiple lab members. In environments like this, without somebody purposefully sitting down to document "common knowledge," techniques and their subtleties often fall through the cracks as personnel come and go. Upon being asked for the first time to construct a colloid sample chamber for 2D experiments in 2009, I had no idea what I was doing. There were no details to follow, so John Savage (our postdoc) followed me into the wet chemistry room and began the process of teaching me everything he knew about these systems. After he left, I became the last person to be working on these systems.

When I graduate, many techniques specific to these 2D crystallization experiments will leave with me, especially those that I have altered or improved. This thesis serves as a short reference guide to those who may arrive after I leave, who may have the intent of carrying on similar experiments, and for Itai to have a document that can be given to such a student.

CHAPTER 2

INSTRUMENTATION

In the broadest possible sense, there are four material requirements to conduct the experiments on systems of microparticles outlined in this thesis. In no particular order, these are:

- Sample Containment
- Solvent
- Microparticles
- Microscope

While each experiment has some variation on one or more of these items, the general idea remains the same: Suspend particles in a solvent, inject the mixture into a containment cell, and image the sample on an optical microscope. The simplest possible system – a glass chamber with glass microparticles suspended in water – is enough to demonstrate Brownian motion[10], a subject on which a few obscure authors such as Einstein and Smoluchowski wrote over 100 years ago[20, 64].

2.1 Sample Containment

It is often the simplest parts of an experiment that are overlooked and cause the biggest headaches. The experiments in this thesis require chemically cleaned glass. In addition to this, they require that any sample exposure to epoxy, used

to seal the chamber after injection of microparticles, is minimized. Failing to adhere to these two principles will result in expedited failure of the sample.

2.1.1 Basic Cleaning

Glass slides and coverslips must be chemically cleaned immediately prior to sample construction to remove any dirt and contaminants that might be residing on the glass surface. It is rare to observe dirt in a sample if a reasonable amount of care went into preparing the sample, and it is easy to detect issues with dirt once the sample is mounted on the microscope. Surface contaminants, such as coatings or oils are much more insidious and have to be carefully avoided. If present, microparticles tend to irreversibly stick to the substrate. Poorly cleaned glass can make this problem difficult to detect, leading to situations where data acquisition may have started before stuck particles are noticed.

Clean glass[1] should be hydrophilic, yet one will inevitably notice that even new glass slides and coverslips taken directly from the manufacturer's packaging is hydrophobic. Thus, even "brand new" glass needs to be cleaned thoroughly. Furthermore, properly cleaning the glass surface but leaving it exposed to air for long periods of time will regenerate the problem.

We have utilized a number of different glass cleaning chemicals and procedures over the past ten years, all of which worked sufficiently well. The method reported here is the one that I introduced to the lab in 2010, as well as the one I used during my externship in Professor Tony Dinsmore's lab at the University of Massachusetts at Amherst. It is effective at limiting the number of stuck

[1]Clean glass will be slightly negatively charged when immersed in water, a fact that affects the choice of microparticles for sample preparation.

particles on the sample surface (less than one per field of view) and is very cost-effective. To clean glass slides and coverslips,

1. Rinse with acetone
2. Lightly scrub with a cleanroom swab
3. Rinse with methanol
4. Rinse with ultra-pure (18.2 MΩ cm) H_2O
5. Dry with N_2 or filtered compressed air
6. Place in base wash for 30 minutes
7. Using tweezers, remove from base wash, rinse with H_2O. Avoid contacting the glass with your gloves.
8. Dry
9. Place glass on a clean workspace.

Base wash is created by mixing 10 g NaOH : 40 mL H_2O. Remember that this reaction will generate a lot of heat and involves the use of a strong base. You must use proper personal safety equipment, a fume hood, containers rated to hold strong bases, and secondary containment for all containers holding the base wash solution for any length of time. Label all labware that contains this solution, including any temporary bottles or glassware. My extended reign as the lab's chemical safety advisor gives me the authority to issue this warning: There are many chemicals in the lab that could harm you in various ways, but this is likely the one that will. It will always be present in the fume hood while you are running experiments, and you will regularly be transferring glassware into and out of it.

2.1.2 Constructing Basic Sample Chambers

Simple nonreusable sample containment cells are created using a glass slide, 25 mm wide, three #1.5 coverslips, two of which are 25 x 25 mm and one is 22 x 22 mm. The two larger coverslips are placed on the glass slide up to 20 mm apart, forming a gap. A small amount of UV-curable adhesive (Norland) is placed along the edge of the air-coverslip-slide interfaces exterior to the gap. Capillary action wicks the adhesive into the coverslip-slide interface, eventually wetting the entire face of the coverslip. The freshly attached slide and coverslips are placed in a UV curing oven for one minute, cured, and removed. The 22 mm coverslip is laid on top of the gap formed by the two larger coverslips and glued in a similar manner. The end result should be a covered gap about 0.17 mm deep, open on two sides. I use a more viscous UV adhesive to partially seal the sides of both openings. The higher viscosity is chosen to limit the amount of adhesive wicked into the sample chamber, allowing me to form a small fill-port in both open ends. This is then cured in the UV oven and is ready for the sample to be injected.

After the sample is injected into the chamber, the open portions of the chamber are sealed with a quick-curing two-part epoxy (Devcon). Some amount of the epoxy will leak into the sample, causing particles to aggregate together and/or stick to the glass in the affected areas. Because this will always happen, there are a few additional steps that we take to limit the ingress of epoxy into the microparticle solution. The fill-ports formed from UV adhesive minimize the contact area of the microparticle solution and the epoxy, impeding leakage into the sample. Leakage is further decreased when the epoxy is mixed thor-

oughly, using the proper ratio of resin to crosslinker[2]. Furthermore, waiting to apply the epoxy until it forms a tacky, moldable semisolid will also help to keep any stray epoxy components from leeching into the cell.

If the UV glue is sloppily applied, and the epoxy is poorly mixed and applied while still liquid, the sample may only be useful for a few hours before the effects of the epoxy can be seen near the center of the sample. Careful preparation of the sample chamber will allow it to last for well over a week, enabling experiments to proceed for much longer time scales.

2.2 Solvent and Microparticles

The solvent and microparticles are lumped together in a single section because the choice of one often dictates required properties of the other. For example, to be able to image deep into a sample with a confocal microscope, particles need to be index matched with their solvent. Charge-stabilized particles may be so repulsive of one-another that additional ions may need to be introduced into the solvent to screen these repulsions and allow the particle to crystallize. The solvent itself may also introduce an attractive interaction, such as through the addition of depletant particles that occupy the otherwise free volume in the sample cell.

The goal of this section is to briefly describe the experimental systems that make up the bulk of the experiments I have run in the Cohen lab. I will also identify a couple of known issues with our system and suggest ways to avoid the problems that held up experiments.

[2]Double-barrel epoxy packages do not dispense as evenly as one might expect.

2.2.1 Microparticles

The microparticles used in the vast majority of the 2D crystallization and melting experiments does not really matter, so long as they are negatively charged in water. I primarily used silica particles, or polystyrene particles with negatively charged functional groups on their surface, such as sulfate or carboxyl. The use of clean and untreated glass as a containment cell is one of the reasons behind the selection of negatively-charged particles, as clean glass is slightly negatively charged in water[27]. Positively charged particles, like amidine-functionalized latex, will crash into the glass and stick irreversibly. Finally, some stock particle solutions will have various chemicals added during or after particle synthesis. If this is the case, particles must be washed thoroughly before use.

Particle sizes were always between 1.0 and 2.0 μm in diameter. Because of the much larger density of silica than polystyrene, silica particles were no larger than 1.5 μm, as I did not density match the 2D experiments because they depend on the particles sedimenting to the surface. Samples using polystyrene particles were sedimented on the microscope stage for a few hours before experiments were started.

Stock particle solutions are purchased or mixed to be 8% solids by volume in water and refrigerated after mixed.

2.2.2 Solvent

The solvent used in all experiments consists primarily of ultrapure H_2O, with a resistivity of 18.2 MΩ cm from a Millipore filter.

Attractive interactions between particles were provided using a depletant, covered in Section 1.1 of this dissertation. We commonly use two chemicals as depletants: sodium dodecyl sulfate (SDS) and hexaethylene glycol monododecyl ether ($C_{12}E_6$). Both of these chemicals are surfactants, with SDS being anionic and $C_{12}E_6$ being nonionic. The concentrations used for either surfactant is chosen to be higher than the critical micelle concentration, but low enough that the surfactant is still in the micellar phase. For phase diagrams of these surfactants, refer to Figure 2.1 for SDS and Figure 2.2 for $C_{12}E_6$. See [30, 37, 34, 12] for additional information for both surfactants. It is these micelles that provide the depletion interaction between the microparticles. Staying within the micellar phase of the surfactants is key: too little surfactant and you will no longer have a depletion interaction, and too much surfactant will aggregate the particles. At even higher concentrations you leave the spherical micelle phase altogether and the surfactant begins to transition into oblong micelles, hexagonal ordering, and crystalline sheets.

Samples using SDS or $C_{12}E_6$ differ in terms of additional charge screening requirements and in terms of the ability to tune the attractive interactions via changing micelle sizes with temperature. The following sections give a brief outline of the sample parameters for the "average" experiment.

SDS Samples

The size of SDS micelles can be controlled by about a factor of two, from 12 nm to 5 nm in diameter as the sample temperature moves from 10 °C to 40 °C[30], with the largest changes in size happening earlier in the temperature range. Near room temperature and above, between 20 °C and 40 °C, the size of the micelle

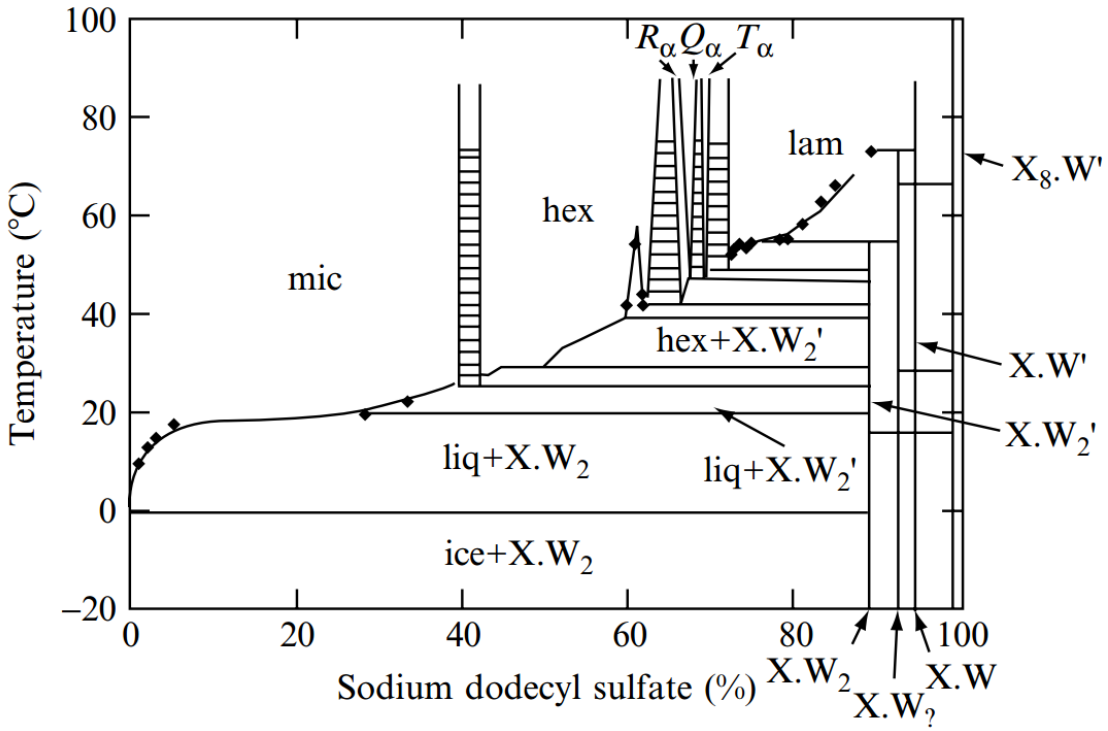

Figure 2.1: Phase diagram for SDS-Water mixtures at a given temperature. In these experiments it is important to remain in the micellar phase, which occupies the upper-left region of this plot. Reprinted from [30].

shrinks only a small amount, from about 7 nm to 5 nm.

Because the size of the SDS micelles do not change strongly with temperature in the temperature range of our experiments, we treat SDS samples as samples with a fixed interaction strength and control its strength by controlling the concentration of SDS during sample preparation, usually between 24 and 32 mM.

Samples mixed with SDS have not needed additional charge screening through the addition of salt (NaCl), likely because of the ionic bond between the sulfate group and sodium atom. To create a sample of SDS-depleted mi-

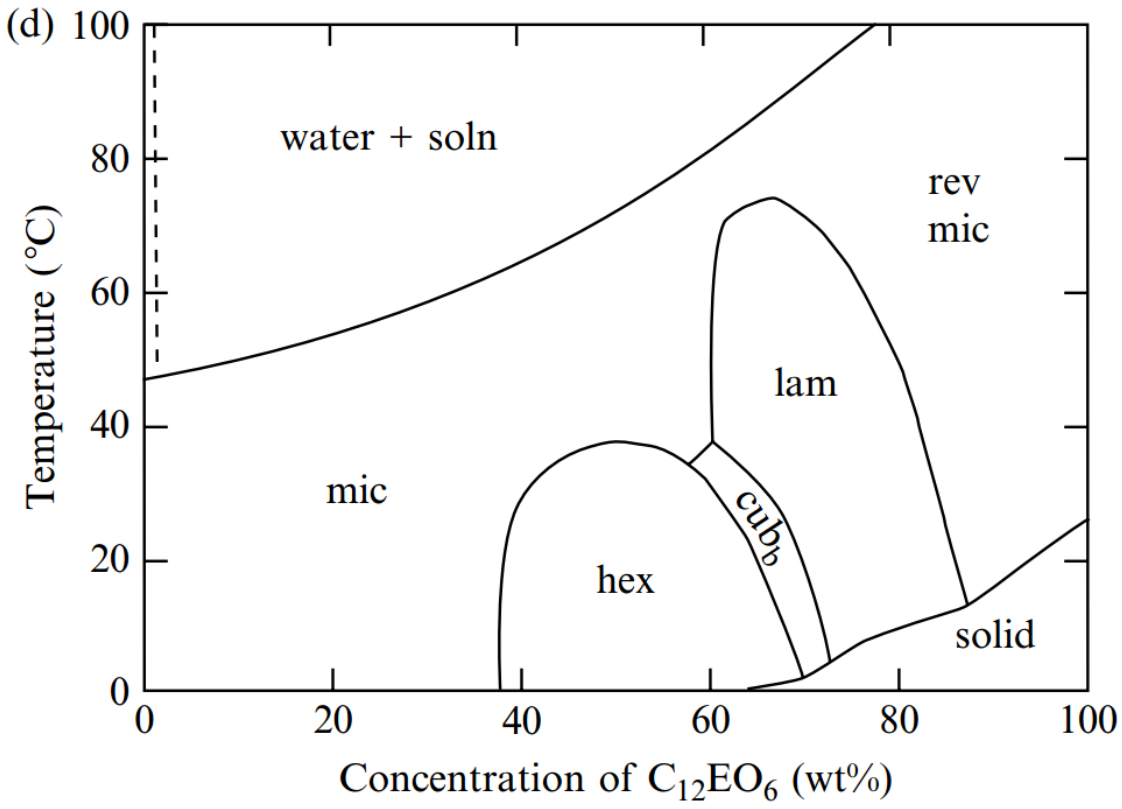

Figure 2.2: Phase diagram for $C_{12}E_6$-Water mixtures at a given temperature. Remaining in the micellar phase with this surfactant requires keeping the temperature below 45 °C at the modest 2.0 wt% used in our experiments. Reprinted from [30].

croparticles, one only needs to add particles to the SDS and H_2O solution.

$C_{12}E_6$ Samples

$C_{12}E_6$ samples afford the ability to significantly change their micelle size and concentration with temperature. At 20 °C, $C_{12}E_6$ micelles are roughly 6 nm in diameter and grow to 40 nm by 40 °C[30] at a concentration of 1.8% by weight. The micelle concentration also increases with temperature, as the solubility of the surfactant in water goes down as temperature goes up. This dual increase

in size and number is what makes $C_{12}E_6$ an attractive option for controlling the interaction potential between colloidal microparticles on-the-fly during active experiments.

Salt must be added to screen the charge on microparticles. Samples are initially mixed from a stock solution of 2 mM NaCl in ultrapure water, giving a Debye screening length of approximately 6 nm. $C_{12}E_6$ is added at a concentration of 2.0 wt%, but the concentration used can vary depending on the observed strength in the experiment. The surfactant is liquid in its pure form and gels immediately upon touching the water. The sample is gently agitated, avoiding the formation of bubbles, until the surfactant has dissolved.

2.3 Issues with $C_{12}E_6$

$C_{12}E_6$ is sensitive to UV and to oxygen. Repeated exposure of the stock to air, or accidentally leaving it out on the counter top (or worse, near the UV oven used to cure sample chambers) can cause degradation of the surfactant. Initially, this is difficult to detect, as the high temperature tunability of the micelle size can mask any underlying issue. Issues begin to manifest themselves as the requirement that your sample temperature be constantly run at unusually elevated temperatures for a given concentration of $C_{12}E_6$. Repeated exposure can be minimized by splitting the stock solution of $C_{12}E_6$ into many smaller vials.

Eventually, as the surfactant stock ages further, particles will appear to stick together, or stick together during sedimentation as if there is a strong attractive interaction. Particles and clusters will randomly stick to the surface of the sample chamber. Being extraordinarily careful with your glass cleaning procedure,

or adjusting the additional salt added to the sample to change the charge screening length will prove fruitless[3]. Once this begins to happen, it is time to throw away the surfactant stock and obtain more.

Unfortunately, the source of the chemical matters. All of the surfactant that we have purchased that works as expected was supplied by Nippon Chemical. Samples purchased from Sigma Aldrich behaved exactly as the expired surfactant samples had, leading us to conclude that the manufacturing process for the chemical could be flawed. This was further evidenced by the packaging of the vials: Nippon Chemical's vials arrived in opaque, sealed glass vials that must be broken open under inert gas, while Sigma Aldrich's vials were transparent with a syringe top.

The major warning here is that finding a reliable vendor for this chemical is an important step. Nippon Chemical offered to synthesize another 10 g of $C_{12}E_6$ for our lab, at a cost of over $5,000. There have since been other vendors offering the chemical (such as Anatrace) in the same packaging as that found at Nippon Chemical. If you must source new chemicals, I would try Anatrace first. However, it is likely a good idea to move away from $C_{12}E_6$ altogether. I recommend looking into finding a depletant that consists of small colloidal particles (tens of nanometers in diameter) that are able to swell in size upon exposure to light or a change in temperature.

[3]John Savage and I initially thought that the ultrapure water filter was to blame for some of the odd behavior we saw in the samples.

2.4 The Microscope

Unless otherwise noted, data was collected on a Zeiss 5 Live inverted confocal microscope used in bright-field mode. The objectives used were Zeiss Plan-Apochromat, 1.4 NA, oil-immersion lenses with either 100x or 63x magnification depending on the requirements of the experiment. Images were captured using a Zeiss AxioCam MRm, producing 12-bit grayscale images at 1388 x 1040 resolution and a maximum frame rate of 48 frames per second, connected via FireWire[4]

A keen reader may realize that the size of a single image is slightly above 17 Mb. The maximum bandwidth of the camera at full-resolution and 48Hz is 830 Mbps, over twice the max bandwidth of the connection interface! To compensate, max-resolution images can only be captured at 14 fps (242 Mbps). Although this was stated in the Zeiss marketing material for the camera, it was *not* made immediately obvious in the data acquisition software. This caused many analysis headaches. Even with this reduced frame rate, the camera was capable of generating approximately 110 GB of data per hour, limiting our ability to quickly image the full sample for days at a time. Thus, short-term experiments on particle diffusion were run at the maximum frame rate, while multi-day experiments were run at one frame per minute.

2.4.1 Standard Thermal Control

Due to the size dependence of $C_{12}E_6$ micelles on temperature and the uncontrolled nature of the shared lab space within which the microscope was located,

[4]Old FireWire – IEEE 1394a – with a bandwidth of 400 mbps

the microscope *stage* was thermally isolated from its surrounding environment. An integrated product line for environmental control of the Zeiss microscopes and stages was used for the majority of experiments. This package consists of an air heater, objective heater, control station, and incubation chamber. These tools supposedly allow control of the sample and environment temperature to within ±0.1 °C. In practice, however, the delayed response of the air heater causes relatively large temperature oscillations of ±0.7 °C across a period of about five minutes when running the heater about 15 °C above ambient temperature.

In addition to the air controller being insufficient for controlling the ambient temperature of the microscope environment to with our desired tolerance of ±0.1 °C, the temperature oscillations themselves caused imaging issues. The sample would cycle in and out of focus as the air heater cycled around the temperature set point, requiring constant manual intervention to keep the sample in focus for more than a few minutes[5]. For this reason, only short experiments that require fast data acquisition are run with on this setup. For longer experiments, I designed a more stable temperature control scheme.

2.4.2 Improved Thermal Control

Improving the ability to control the temperature of the system required two main components: better thermal isolation of the entire microscope, and better control of the sample's local environment. Improved isolation of the microscope itself was required mainly because of the unreliable state of the room's air conditioning system, causing major issues with the sample's focus. A large change

[5]There exists a lab legend of two post-docs and a graduate student that took shifts to monitor data acquisition on this setup over the course of a week.

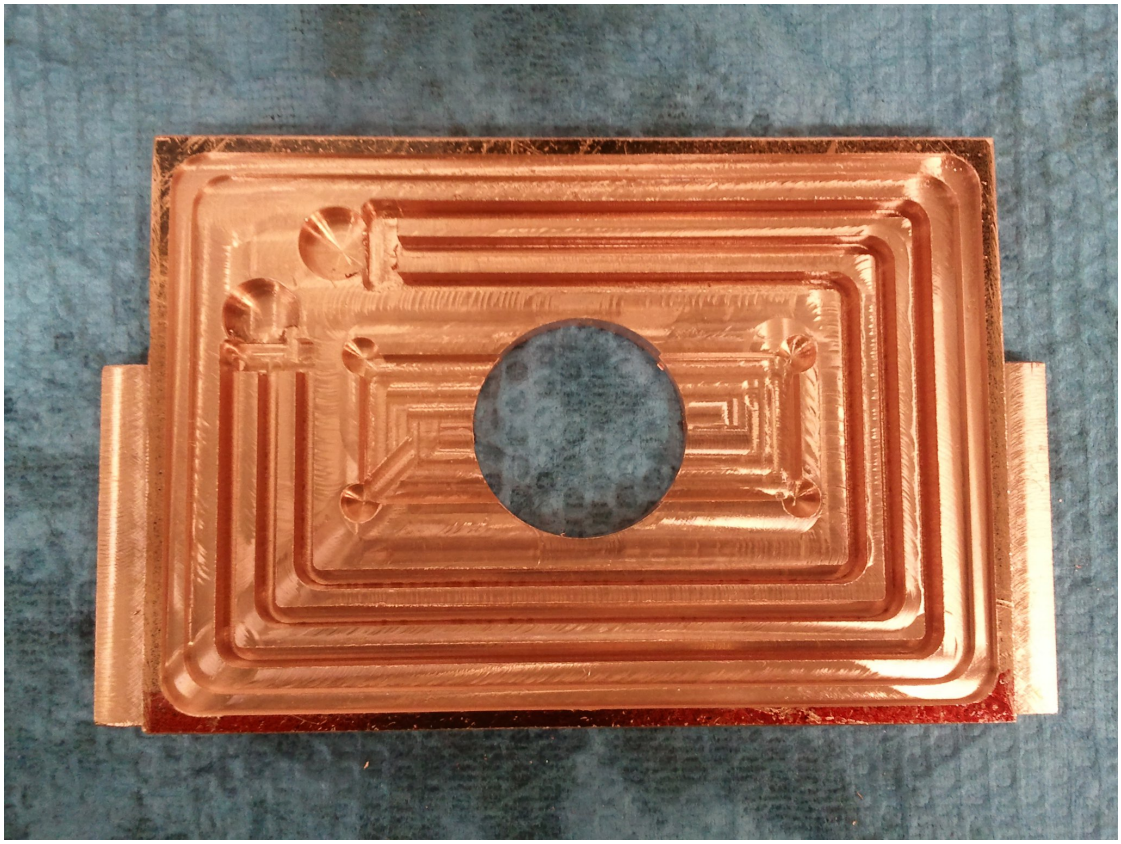

Figure 2.3: Custom copper water block used for precise control of the air and surface temperature surrounding a sample. Glass slides are mounted horizontally across the center hole, allowing the objective lens to come in contact with the sample from underneath and transmitted light to enter from the top. Water is pumped in and out through the holes in the top-left of the block, traveling along three trenches running along the outer portion of the block. The block is sealed from above with a plastic cover (not pictured).

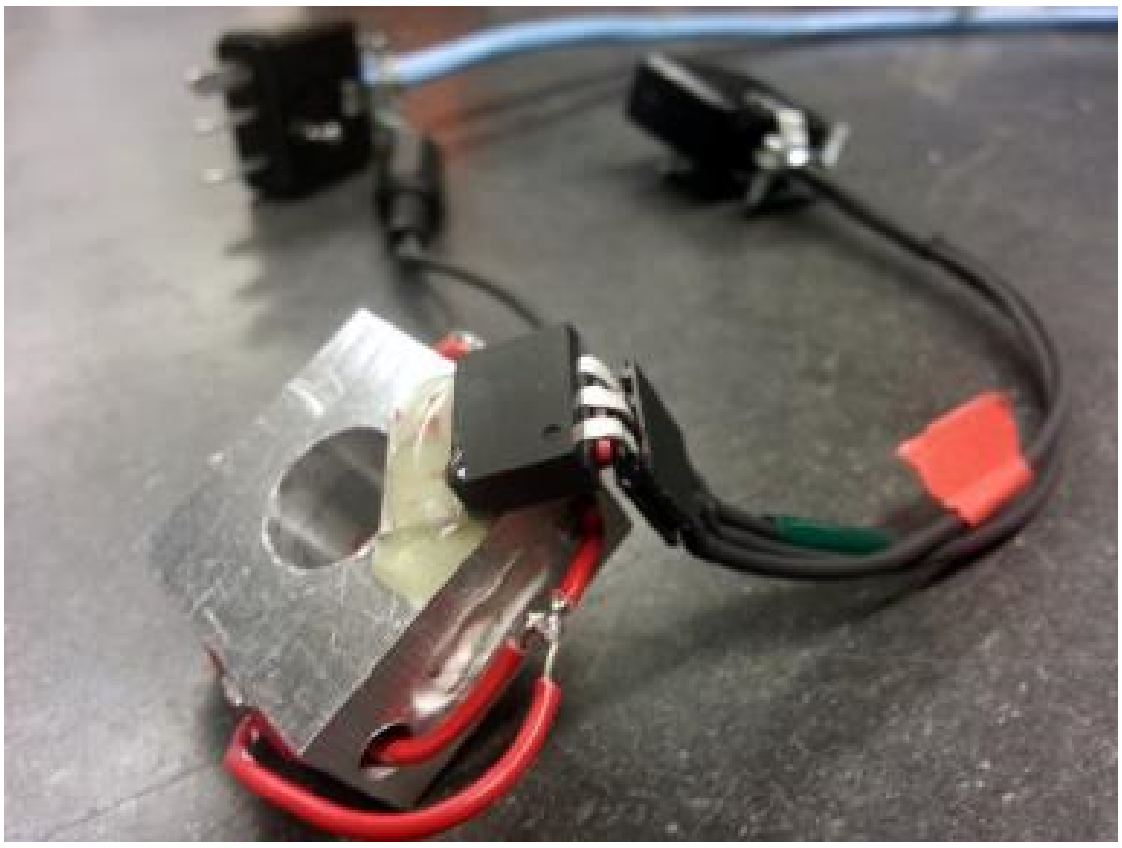

Figure 2.4: Custom aluminum resistive heating block used for directly controlling sample temperature from above. The through-hole allows all light from the condenser to reach the sample. Red wires lead to four buried resistors, equal in resistance with a total device resistance of 40 Ω. Resistor cavities are filled with thermal compound. The black IC in the center of the image (Texas Instruments LM35) is the temperature sensor, which is attached to the aluminum body with thermal compound and epoxied in place. The dimensions of the heating element are 25.0 mm × 25.0 mm × 12.5 mm.

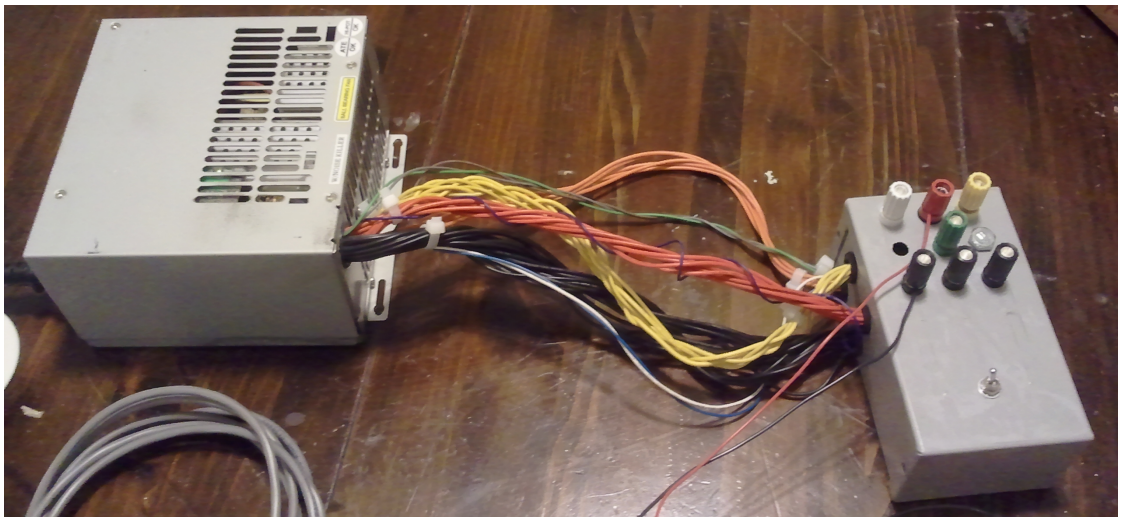

Figure 2.5: Repurposed ATX computer power supply. Molex connectors were stripped and equal voltage outputs were gathered across rails. Wires were fed into a breakout chassis and terminated at their respective colors.

(approximately 3 °C) in the room temperature usually meant that the sample would drift out of focus permanently.

To isolate the microscope, a containment box was constructed from 5 cm thick extruded polystyrene (Owens Corning). The microscope was fully enclosed on all sides, including the bottom. A variable-sized port was created in the top panel to allow heat from the microscope light source to vent. Three holes were cut into the base of the box: one for wiring and two for water hoses.

For better control of the microscope stage temperature, the Zeiss air circulator was shelved. In its place we used a water-regulated copper stage which we designed and machined in the CCMR and UMass Amherst Physics Department machine shops, displayed in Figure 2.3. The stage was was then attached to a water circulator capable of controlling its water temperature to within ±0.1 °C via the ability to both heat and cool its reservoir.

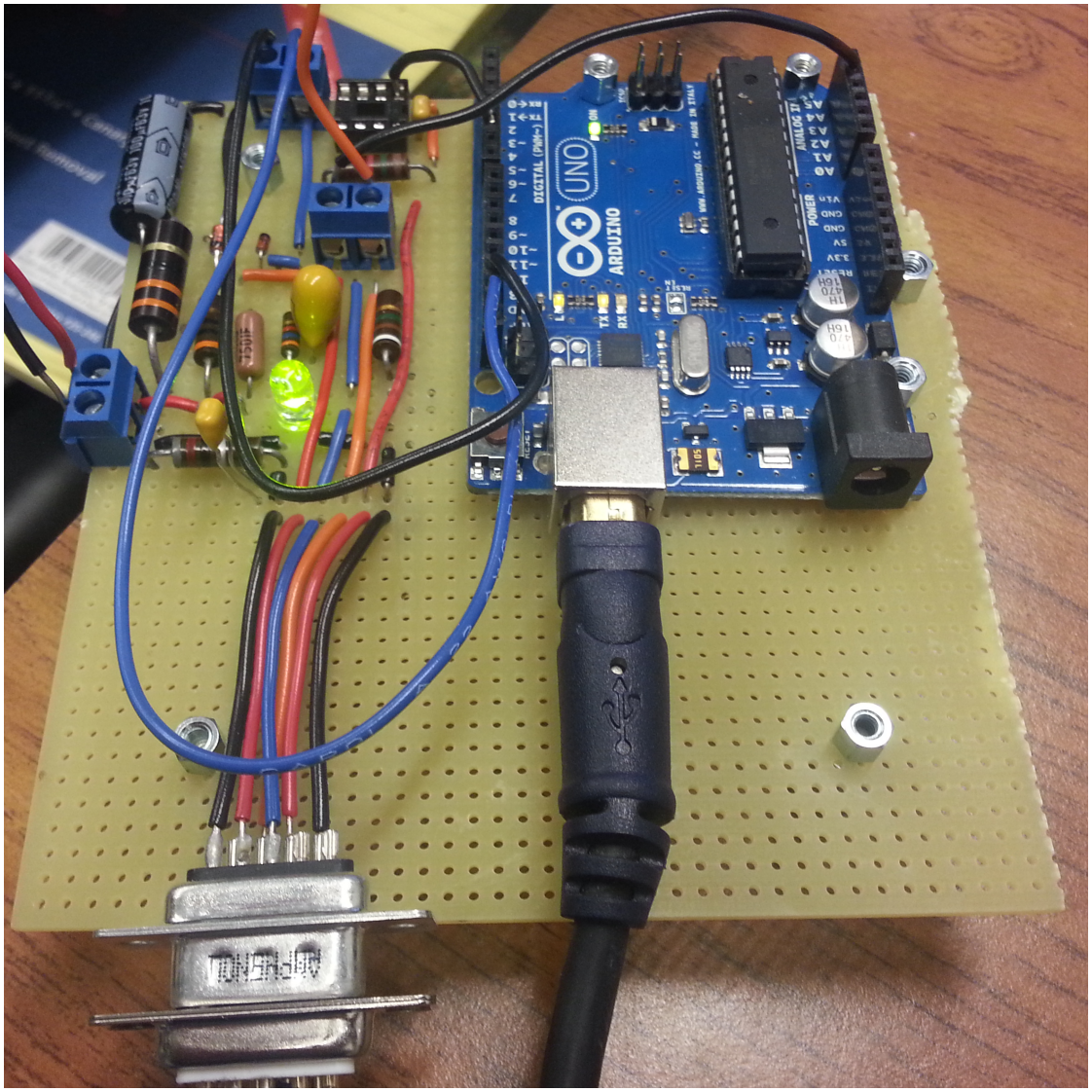

Figure 2.6: Image of the final prototype heater, sensor, and PID control device. The Arduino microcontroller, which handles the temperature readings and PID controller, is seen on the right side of the image. The remaining electronics on the left handle the rest of the major tasks: switching the heater output, supplying a 5 V line for the thermometer, activating a power LED when the external power supply is on, and providing a reference voltage to set the range of the microcontroller's temperature measurements.

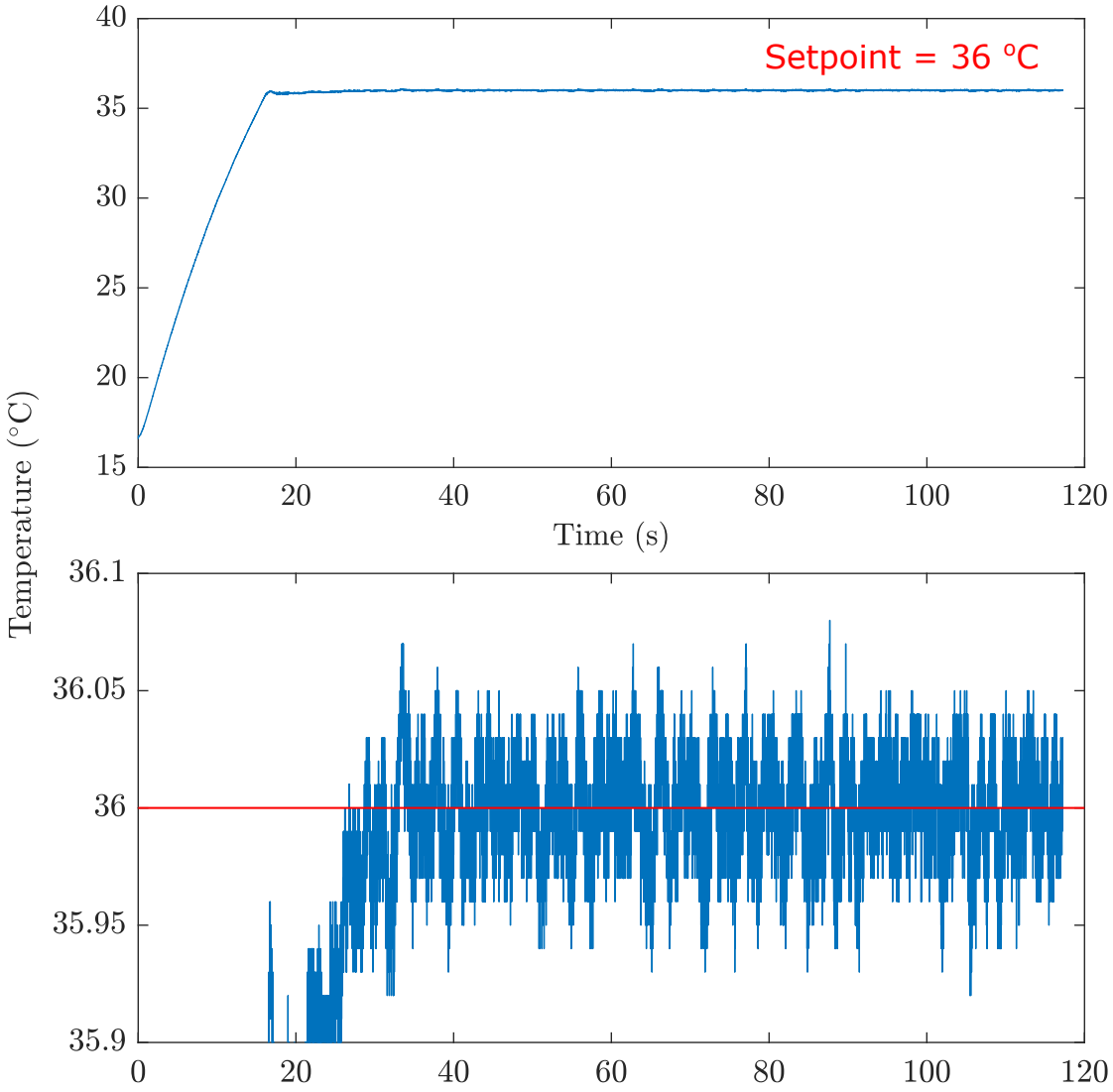

Figure 2.7: PID-controlled heating element temperature as a function of time. The temperature controller was set to a target temperature of 36 °C, with an ambient temperature of 17 °C. (**top**) After a relatively short temperature rise time of 18 s versus air circulation, the heating block temperature stabilizes at the target temperature by 40 s. (**bottom**) Oscillations about the target temperature under the desired limit of ±0.1 °C is achieved, with maximum excursions from the target rarely exceeding ±0.05 °C.

For local control of the sample temperature, the Zeiss objective heater from Section 2.4.1 is again utilized. However, the sample is also heated from above using a custom-built PID-controlled resistive heating element machined from aluminum, shown in Figure 2.4. The heating element is affixed to the sample with thermal paste (Arctic Silver) and spot-epoxied at its edges. The temperature of the heating element is regulated by a PID controller implemented on an Arduino microcontroller using modified open-source code[6]. Because the microcontroller cannot supply enough power to the heating element, a repurposed ATX power supply (see Figure 2.5) is connected to the heating element through a power MOSFET. The PID controller triggers the switching of this transistor to achieve temperature regulation of the heater. An image of the final device is shown in Figure 2.6.

Temperature data is reported via serial connection by the microcontroller, which can be accessed directly with various standard binaries (powershell, hyperterminal, cu) or in Matlab through its serial port functions. The temperature setpoint can be changed on-the-fly through the serial connection to the microcontroller. We have developed a short program in Matlab that live-plots the temperature received from the device, the temperature setpoint, and the values of the PID parameters, which is useful for setting up the device. Ultimately, the device reduces the temperature oscillations in the environment around the sample by an order of magnitude (Figure 2.7), allowing for better control of the attractive interaction commonly employed in our samples while simultaneously eliminating the focal "breathing" effects seen when heating the entire microscope via the standard air incubation units.

[6]During the creation of the temperature controller, the Arduino did not have a PID library. Now it does, which was a missed opportunity.

This improved temperature control scheme not only allows week-long experiments to be performed more reliably and with less manual labor, but it is also very inexpensive. The material costs of the major components – the Arduino, the polystyrene panels, and the copper block – total less than $100.

CHAPTER 3

DATA ANALYSIS

3.1 Introduction

Let us imagine that after careful sample preparation following Chapter 2, a starry-eyed graduate student loads her sample onto the microscope stage, aligns the optics and fiddles with the camera electronics. The graduate student sees a uniform dark gray background with thousands of white, Gaussian-like blobs[1], capped off at their centers by bright maxima, all diffusing around in the camera output. The graduate student has achieved perfection. However, this is not necessarily the state that we can find many experiments to be run in. Not all experiments use spherical particles or are able to image relatively deep into the sample without considerable issues with particle scattering.

The main issue with these non-ideal images formed with non-ideal particles is that feature extraction algorithms commonly found in microscopy have not changed appreciably [8]. Many well-accepted software packages in the microscopy community are based on variations on a similar heuristic: identify bright blobs in an image and fit a gaussian to it [2, 3, 9, 16, 28, 23, 42, 43, 51, 49, 56, 63]. Individual packages differ in their intended specialization, whether it be speed, hardware, fit techniques, convolution kernels, or even just being made available in a different language. These packages are excellent at the task they set out to do: identify the centers of particles as precisely as they can. Again, not all experimental data fits the paradigm of a collection of Gaussian-

[1] A blob is a technical term for a contiguous region of an image that represents something of interest. In the context of this thesis, blobs are regions of an image representing a particle.

like blobs. The experiment detailed in Chapter 4 is an example of one of these exceptions. Systems where particles are specifically designed to be dimpled, mushroom capped, buckled, or otherwise deformed compared to ideal spherical particles[32, 55] pose significant challenges for featuring routines.

There are two major parts to data extraction in this system: featuring and analysis. Featuring is essentially the process of finding and classifying particles from video data. Analysis involves applying numerical methods to get insight into the behavior of the system. The boundary between these two parts can be blurry. Analysis may generate additional classifications for particles, which may be advantageous to store with feature data. To make the discussion clear, I will discuss analysis methods *assuming that we have a featured data set*, as the analysis of the data is what is crucial for understanding the physics of these systems.

There is a large body of work that has been done in this laboratory by Brian Leahy, Lena Bartell, and myself, all in different systems but toward the same goal: automating accurate feature detection in messy settings. For the scope of this thesis, I restrict myself to the dataset of manually featured ground-truth particle center and size data, which represents approximately 1700 hours of my working time as a graduate student. This number should highlight the importance of developing proper automation routines for these tasks. Automation of feature detection in these messy systems would enable rapid analysis of much larger sets of data, or data from multiple sets of experiments. Combined with more precise measurements though better featuring algorithms, this is a clear pathway for improving experimental accuracy and throughput, further advancing the ability of optical microscopy to probe new physics.

3.2 Analysis

Let's assume that we have a featured set of particles, extracted from an experiment on binary microparticles. The feature set consists of a list of (x,y) float pairs, indicating the particle centers on a pixel grid (your image), and a size for each particle. The fact that the particles are "binary" means that the individual species have a polydispersity of less than 4%, so we classify their size as a binary: particles can either be large or small. We also have information on a particle's "layer height", which is also binary: either they reside on the glass substrate, or they do not. Finally, lets assume that we have this data for all time.

3.2.1 Particle Sizes

We have a good general idea of the sizes of particles in the system due to the fact that our binary particle species have low polydispersity, and we know the microscope optics, and we know the properties of the camera recording the data. However, it is important to measure the sizes of the particles in the system, since much of the analysis will depend on various length cutoffs based on particle sizes and the assumption that a particle's nearest neighbors are in contact.

Obviously, directly measuring a particle's size from an image is an option. Unfortunately, because the edges of small, optically imaged microparticles are inherently blurry, it is not often the greatest of ideas to visually measure the size of a single particle, especially when your particle blobs are not well-formed. In our samples, we have crystals of large and small particles. We can use these structures to our advantage to measure distances: measuring across the interiors

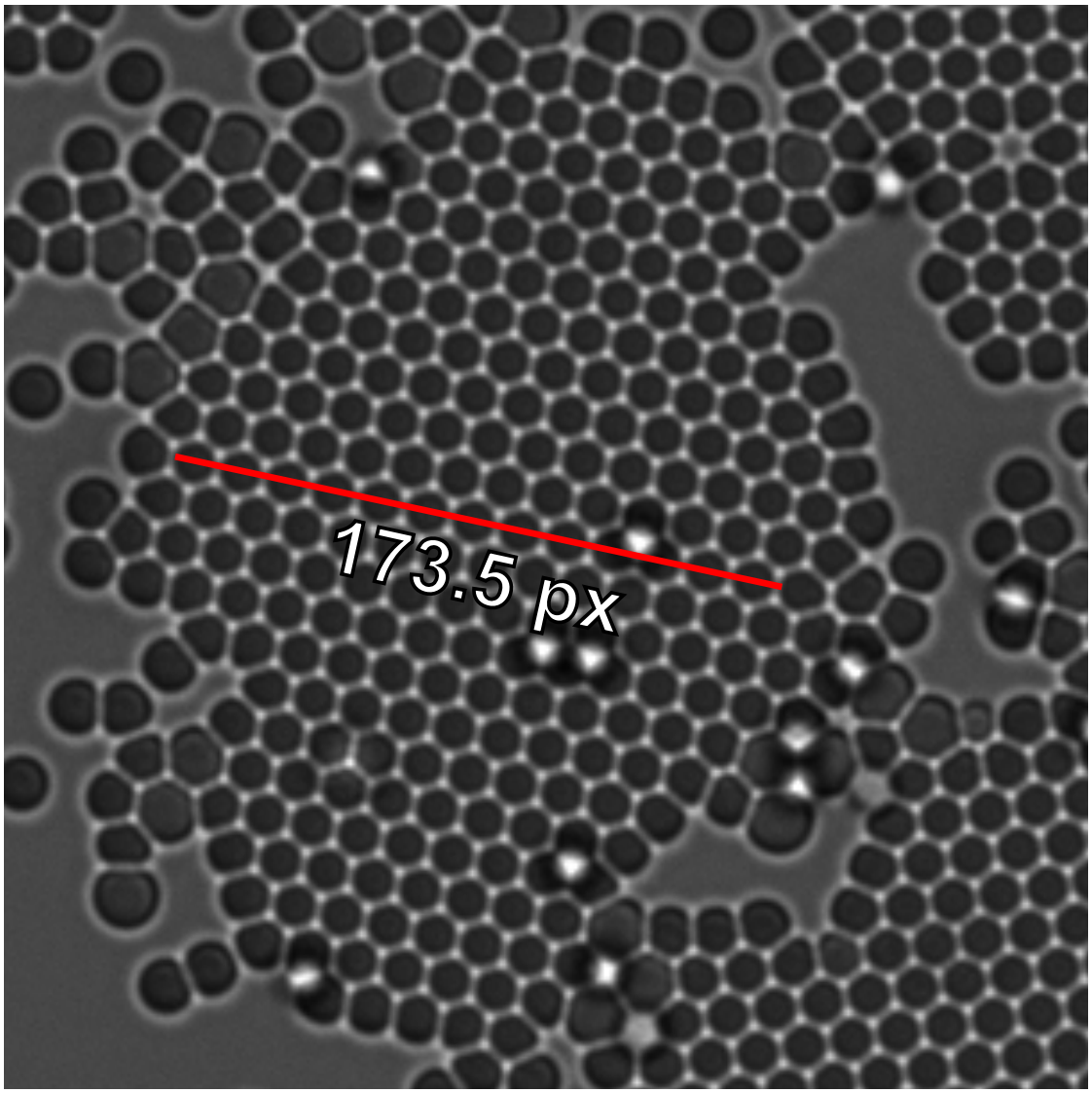

Figure 3.1: Simple measurement technique to extract particle sizes: Here, we measure across the interior of a crystal composed of 1.0 µm particles to obtain an average particle size. The red line spans 13 small particles and is 173.5 px long in the original image, resulting in an average particle diameter of 13.3 px.

of crystals ensures that there are multiple particles to average across, each as close to its neighbor as it can be. This technique is presented in Figure 3.1, resulting in an average particle diameter of approximately 13.3 px.

Measuring and averaging across crystalline particles is a "quick and dirty" way to get a particle length measurement. A more rigorous way to measure the particle size is to compute the conditional probability of finding a particle a distance r away from another particle by measuring the 2D pair correlation function,

$$g(r) = \frac{1}{2\pi r N c_0} \sum_{i}^{N} \sum_{i \neq j}^{N} \delta(r - |\mathbf{r_i} - \mathbf{r_j}|)., \tag{3.1}$$

where $\mathbf{r_i}$ is the location of particle i, $\mathbf{r_j}$ is the location of particle j, N is the total number of particles, and c_0 is the area fraction of the particles. The first peak of this function represents the first relatively common distance to find neighbors of a particle. In the case of our data where many particles are crystalline and they are assumed to be interacting only while visibly in contact, the location of the first peak corresponds to the average particle size.

We have developed Matlab code that computes $g(r)$ very rapidly compared to some notable widely-distributed versions of code for microscopic particle analysis[31]. Surprisingly, it is not too difficult to find examples of code that mishandles computing $g(r)$ at a particle located too near a boundary. There is excellent information available at [15] on this topic, so I surmise that the field's slow move away from IDL may have left some important pieces of this code-base by the wayside. In our code, we handle the boundaries by only sampling particle pairs with an origin inside an inner image area defined by a maximum radial distance cutoff, ensuring that the measurement is free of edge effects at distances smaller than the cutoff. This is ensured at the expense of measuring $g(r)$ at distances greater than the cutoff, however, increasing this cutoff decreases the total number of particles available to count. The result of measuring $g(r)$ and finding the first peak location is presented in Figure 3.2. Notice that this method also yields an average small particle diameter of 13.3 px.

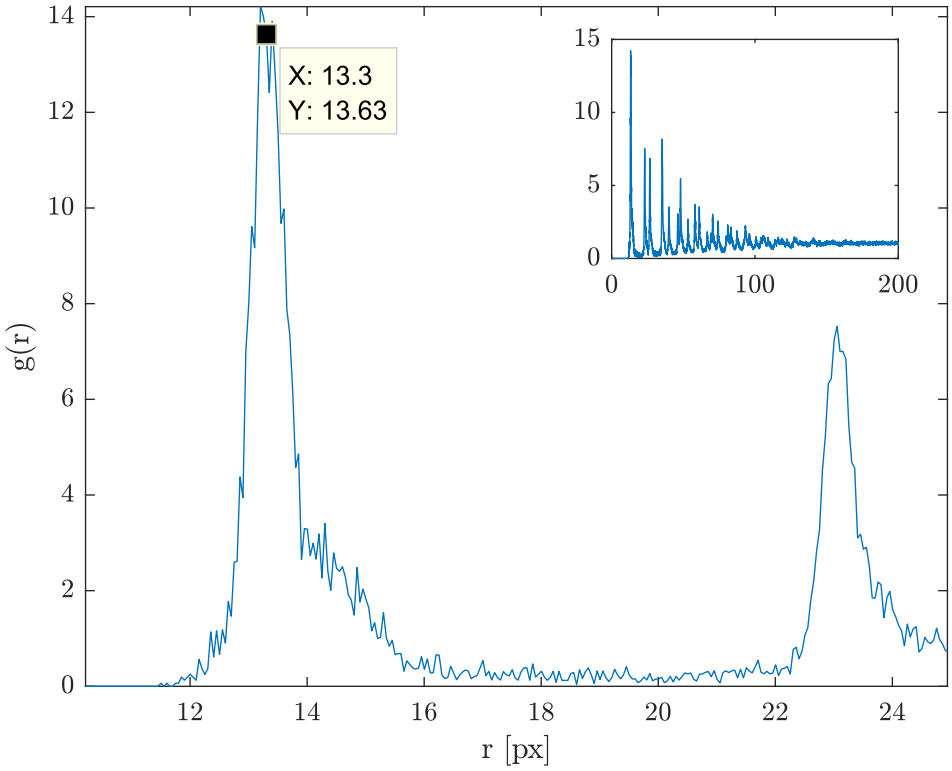

Figure 3.2: Pair correlation function, $g(r)$, between first peak and first split of second peak. This measurement considers only the positions of small (1.0 µm) particles in an image of a mixed-phase system consisting of gaseous and crystalline regions of binary microparticles. Notice the first peak is centered around 13.3 px, which is consistent with the particle diameter measured directly in Figure 3.1. (**Inset**): Full $g(r)$, out to $r_{max} = 200$ px.

For reference, this code computes $g(r)$ in a 1388 x 1040 image with approximately 6000 particles and 4000 radial steps in about 0.4 seconds. Previously mentioned code does this same job, without handling boundary effects, in 800 seconds. The final result: a more accurate routine that runs three orders of magnitude faster. The code was compared on a 8 (16 logical) core AMD Ryzen CPU running at 4.0 GHz with an Nvidia GeForce 1070 GTX GPU. This code has been contributed for use in a number of colloidal microscopy projects in the Cohen

lab since 2011.

See Appendix A.1 for sample Matlab code and more information.

3.2.2 Bond Orientation Order Parameter ψ_6

The particle size estimate obtained from $g(r)$ is essential for determining the nearest neighbors of each particle, which in turn is critical for measuring the local orientational order, edge membership, and cluster membership of particles. The local six-fold bond orientational order parameter ψ_6 is given by

$$\psi_6(k) = |\frac{1}{Z_k} \sum_{j \in \mathrm{NN}} \exp(6i\theta_{jk})|$$

for each particle k, where Z_k is the particle's nearest neighbor (NN) count and θ_{jk} is the angle formed between the particle, its j^{th} bonded neighbor, and an arbitrary reference axis[36, 47, 65]. Values of ψ_6 range between zero and one. Particles in a fluid have ψ_6 values near zero, while those in a perfect triangular lattice have a value of one. Figure 3.3 illustrates the utility of this measurement for determining which particles are members of a crystal, and which ones are not. To do this, we need to identify each particle's nearest neighbors and their associated angles.

To obtain each particle's set of nearest neighbors, we first compute the distance matrices Δx and Δy containing the separation between all particle pairs (i, j) in a single layer in the x and y dimensions,

$$\begin{aligned} \Delta x_{ij} &= \hat{\mathbf{x}} \cdot \left(\mathbf{r}_i - \mathbf{r}_j \right) \\ \Delta y_{ij} &= \hat{\mathbf{y}} \cdot \left(\mathbf{r}_i - \mathbf{r}_j \right), \end{aligned}$$

Using these matrices, we compute D, the distance between all particles, where

$$D_{ij} = (\Delta x_{ij}^2 + \Delta y_{ij}^2)^{1/2}$$

To identify the nearest neighbors for each particle, we define a connectivity matrix, C, such that

$$C_{ij} = \begin{cases} 1 & 0 < D_{ij} \leq d \\ 0 & \text{otherwise,} \end{cases}$$

where d is the average particle diameter as determined in Section 3.2.1. The condition that $0 < D_{ij} \leq d$ does not allow for particles to identify themselves as a connection. Because this matrix is inherently symmetric, summing over either dimension will produce a vector with elements equal to each particle's nearest neighbor count:

$$Z_i = \sum_j C_{ij}$$

Finally, we must compute the angle between each pair of particles and a reference axis, which is chosen to be $\hat{\mathbf{x}}$. This can be done using the x and y separation matrices:

$$\theta_{ij} = \arctan\left(\frac{\Delta y_{ij}}{\Delta x_{ij}}\right)$$

With all of these elements computed, we have all of the components required to compute ψ_6 for each particle in the system by referring to C and collecting the angles for each neighbor. All of this can be done rather quickly with vectorized code that also takes advantage of GPU resources in Matlab, which I have contributed to the various Cohen group members for use in colloidal microscopy projects. See Appendix A.2 for the code. For a quick observation and discussion on the speedup of the entire chain of computations for ψ_6, which relies on brute-force computation of interparticle distances, see Appendix A.3.

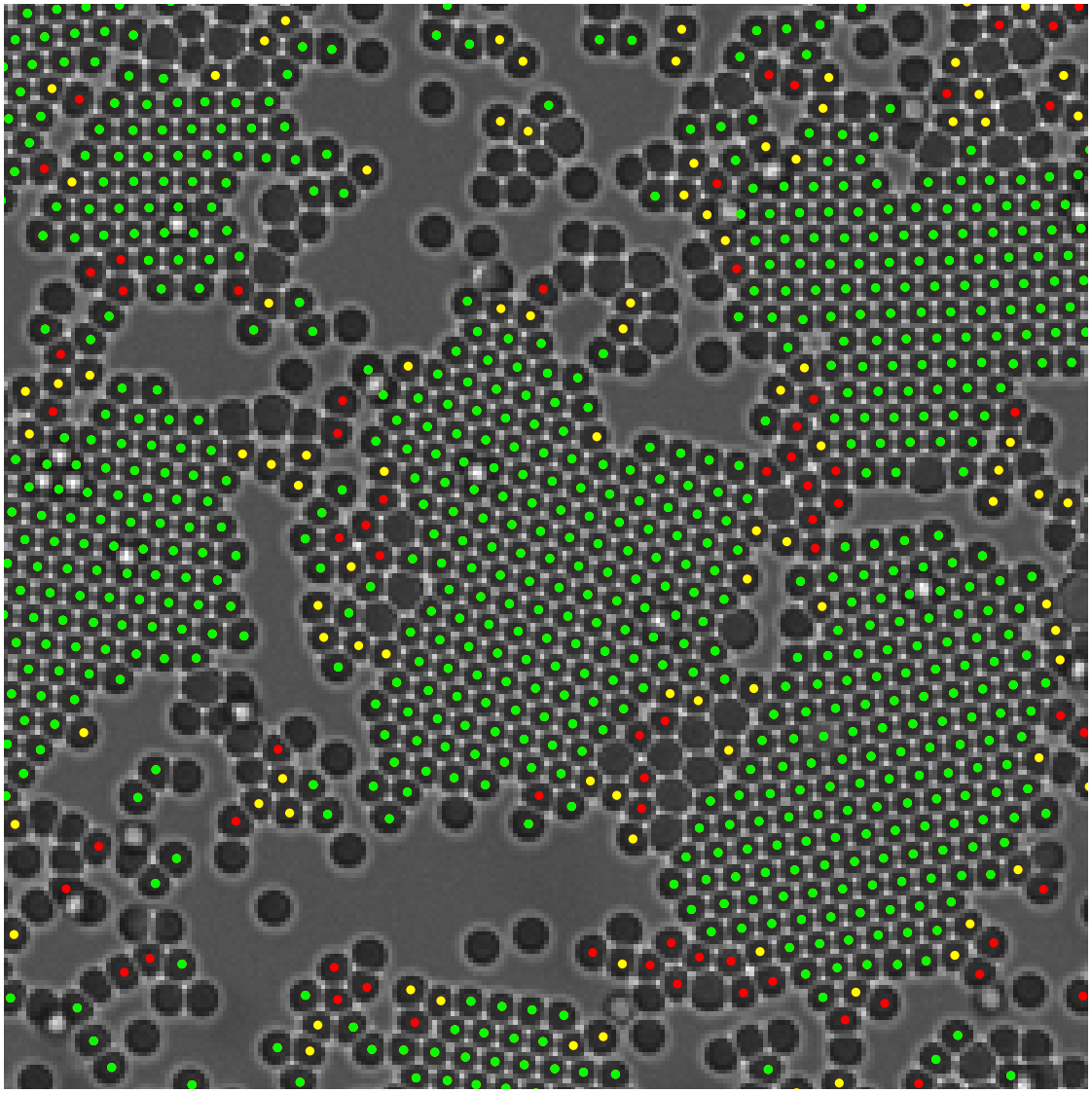

Figure 3.3: Crystal and amorphous islands with ψ_6 values overlaid on each small particle residing on the substrate. Red: $\psi_6 > 0.25$, Yellow: $\psi_6 > 0.5$, Green: $\psi_6 > 0.75$.

3.2.3 Perimeter Particles

One of the quantities of interest in the crystallization dynamics of bidisperse spheres is the number of perimeter particles, since the perimeter of islands of small particles is the only place the large particles can interact with crystallized particles. Furthermore, large particles were usually found to be attached directly to the perimeter of crystals composed of small particles. We employ two ways of automating the classification of edge particles, one involving the clustering of particles into individual crystals via graph traversal, and another we developed that restricts the computation to a particle's neighbors and the neighbor's neighbors.

Crystal Membership

Using depth-first search, we traverse the matrix C to assign each particle to a crystal. We place constraints on the connectivity matrix such that only values of ψ_6 above 0.75 will be considered, and we assume that all small particles with six neighbors are crystalline.

The connectivity matrix represents a set of more than one tree. To traverse the multiple trees in an image, we track the number of times the traversal algorithm was run. Every connected particle in a given run is assigned this number, effectively assigning each particle a cluster number. Further analysis on individual clusters to extract the boundary is straightforward: for each cluster, any particle with less than six nearest neighbors must be a particle located on the perimeter. While this method is fairly effective at determining cluster boundaries, it does not capture the compactness expected in a crystal boundary: par-

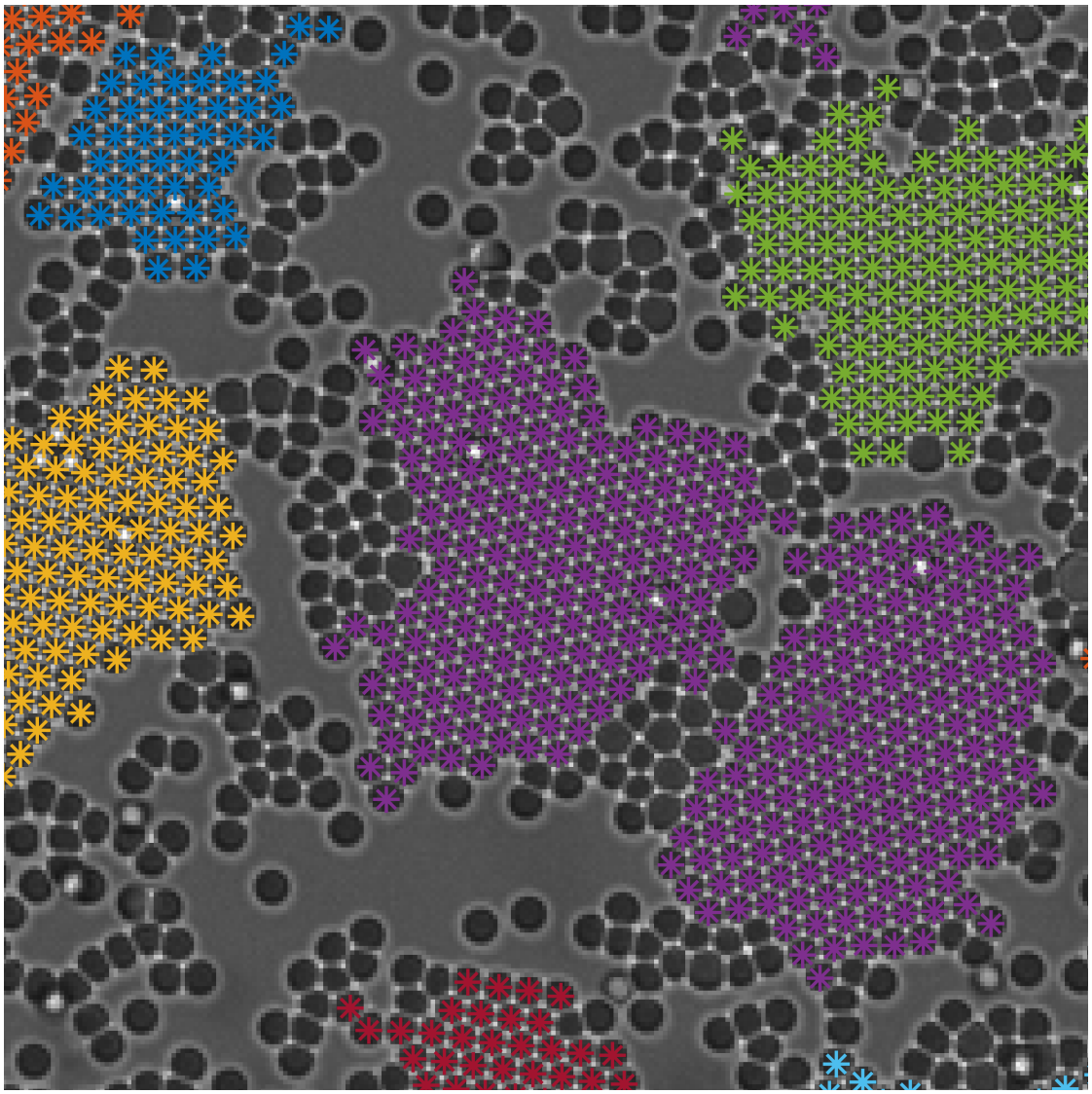

Figure 3.4: Crystal islands defined using depth-first search. Colors are assigned randomly to each cluster. Notice that the large particles consistently interfere with island edges, creating pockets and jagged edges.

ticle offshoots from the crystal that happen to have a high ψ_6 value as seen in singly-connected components in Figure 3.4 are inevitably counted as boundary particles. Arguably, these particles should not be considered part of a crystal, as they skirt the idea behind the rule that ψ_6 requires two nearest neighbors. A particle forming a bond with a second, disjoint neighbor that happens to have the correct bond angle is not equivalent to a compact three-particle island.

Localized perimeter membership

To handle issues like these, we have developed another way to classify crystal perimeter particles. For general crystal islands – those that are not simply one layer thick, as sometimes found with ψ_6 – it is advantageous to consider a particle's nearest neighbors as well as the neighbors of those neighbors to determine its classification. Particles with six nearest neighbors are assumed to be part of a crystal interior, but particles at the crystal boundary can have between two and five neighbors. Considering that any non-crystalline cluster of particles might have up to five neighbors, the boundary can be much more difficult to classify.

Looking at the connectivity of the nearest neighbors of a particle gives information on whether or not the particle in question is only singly-bound to a crystal, and whether the neighbors themselves are part of a crystal. For the usual case in our experiments, crystals with no vacancies near an edge, the general idea is that a suspected edge particle must have at least two neighbors. These neighbors must be neighbors of each other and a mutual neighbors of a fourth particle. These constraints are depicted in Figure 3.5.

We implement these rules by selecting a random particle with $2 \leq NN \leq 5$

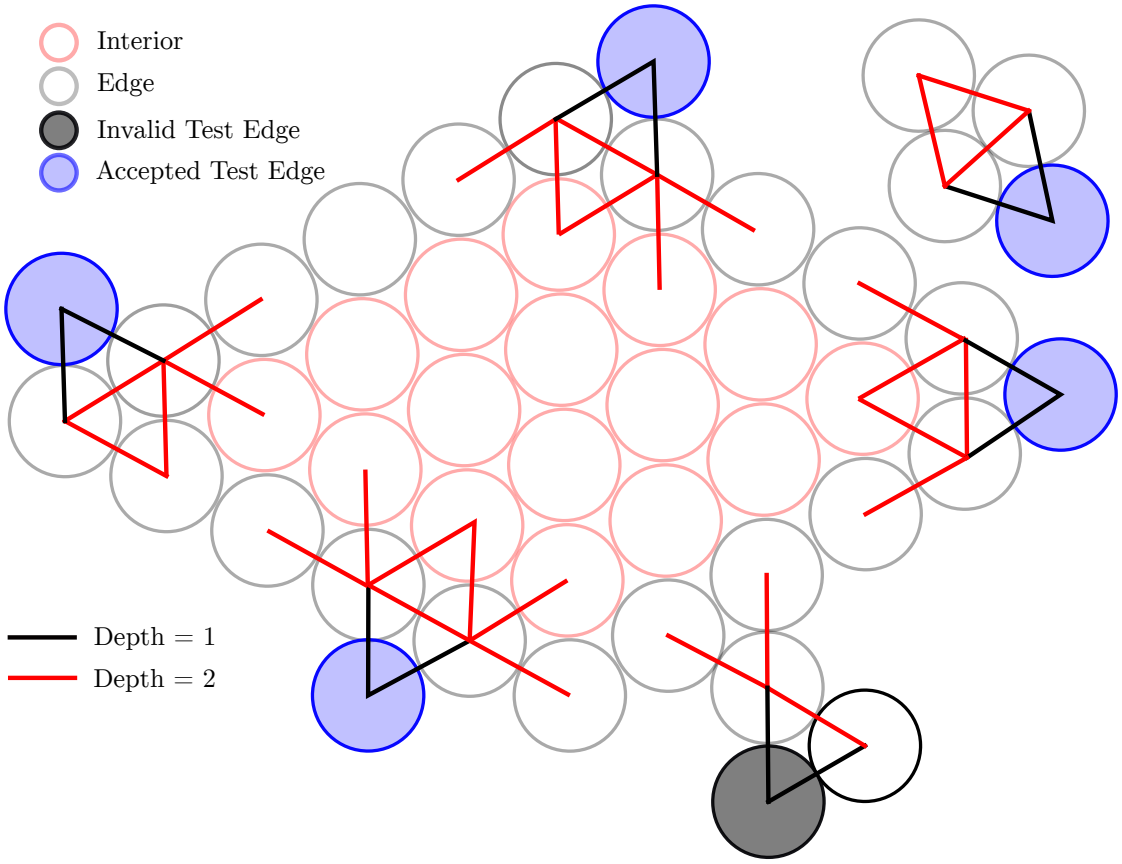

Figure 3.5: Example of adding a particle to unique positions at the edges of a triangular lattice. Blue or black particles represent "test" particles added to the lattice. Black lines represent paths to a set of the particle's nearest neighbors, NN_1. A red line leads from NN_1 to their nearest neighbors, NN_2. Drawing the links to the nearest neighbor sets for each test particle begins to reveal a pattern: an acceptable edge particle participates in two closed traversal loops. Particles without a second traversal path (e.g., the dark particle) are excluded from edges, even though they may temporarily share the same lattice orientation.

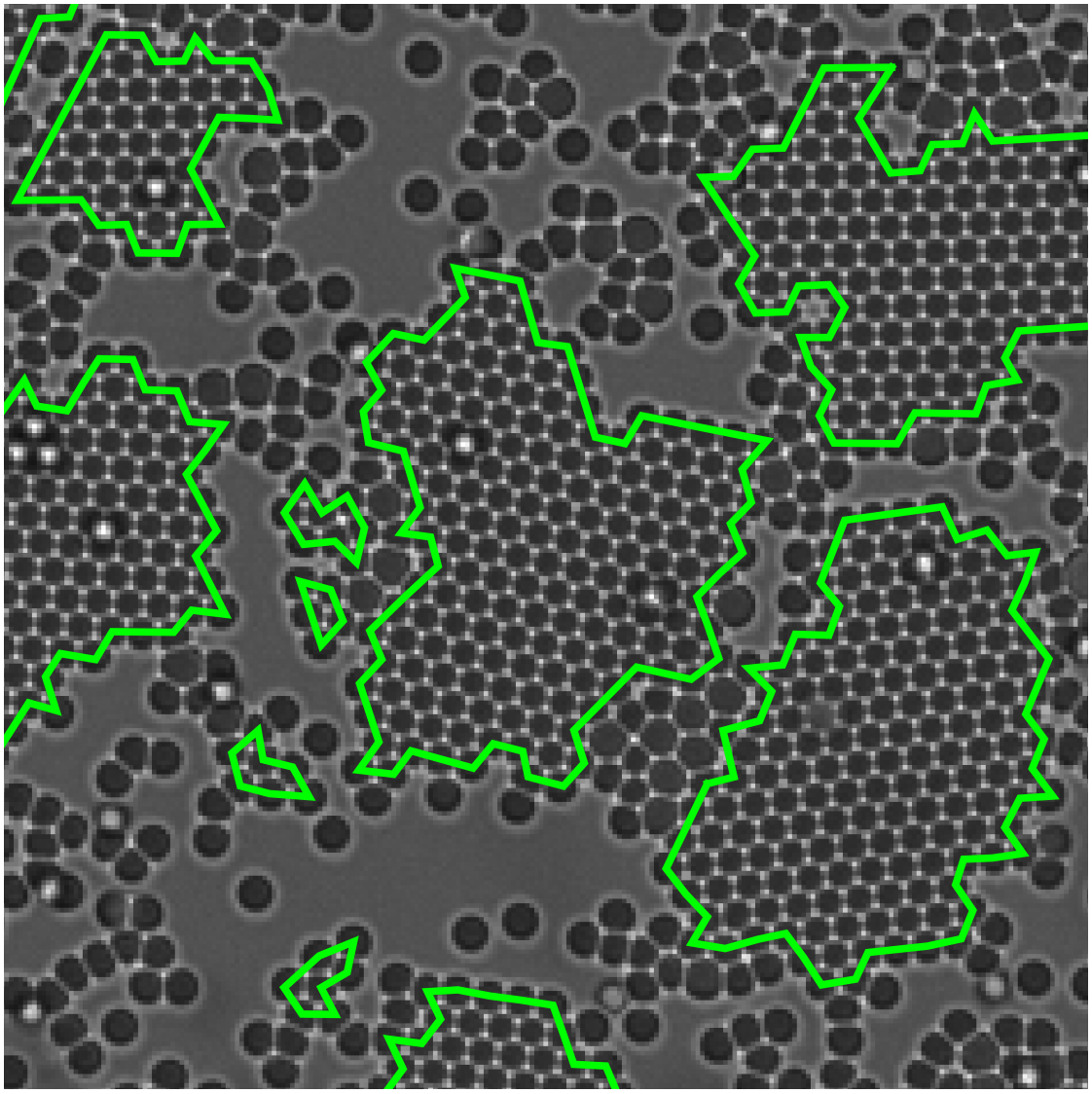

Figure 3.6: Perimeter particles found via breadth-first search of particles with between 2 and 5 nearest neighbors. Compare to outermost particles in Figure 3.4. This method tends to include edge particles with low ψ_6 due to neighbors with a single bond to the crystal and tends to eliminate issues with single particle bridges between crystal islands.

and use C_{ij} to inspect the set of nearest neighbors of the first particle as well as the particles bonded to the neighbors. Neighbors with less than six bonds can be marked as potential boundary particles, revisited later, and the process repeated until no unclassified particles remain. This is essentially a breadth-first search over the C_{ij}, terminating after the second layer has been traversed. We often use this method to compliment the crystal clustering method of Section 3.2.3. Figure 3.6 shows the final results.

CHAPTER 4

CATALYSIS OF SINGLE-TO-DOUBLE LAYERED CRYSTAL GROWTH IN BIDISPERSE COLLOIDAL SUSPENSIONS

This chapter contains a draft of the titular paper, submitted for publication in *Physical Review Letters* in October 2017.

4.1 Abstract

We report experiments on depletion driven crystal growth of colloidal suspensions at a surface where the addition of a secondary species of larger particles alters the crystal growth process from formation of single layer crystals to two layer crystals. We record the nucleation and growth of these bilayer crystals over time. Remarkably, we find that the monolayer regions of these crystals melt while the top layer growth accelerates. The simultaneous melting of the bottom layer and growth of the top layer continued until all crystals composed of small particles had two full layers. We describe a simple growth model that captures the behavior of the second-layer growth and put forward a mechanism by which the large particles may act as a catalyst in the growth of the second layer.

4.2 Introduction

Crystallization of atoms, nanoparticles, and microparticles is ubiquitous in nature. Recent experiments across multiple research disciplines have shown

that the process of crystallization does not always follow classical nucleation and growth scenarios. Crystallization of certain materials may be prefaced by the formation of structured precrystalline states or punctuated by intermediate metastable or kinetically-determined states that substantially affect crystal growth [18, 33]. To accurately predict crystallization rates in these systems [5, 21], such alternative pathways for material crystallization may need to be taken into account. The manner in which these intermediary states depend on solution chemistry, interparticle potential, polydispersity, and kinetics remains poorly understood.

The growing body of evidence for alternative crystallization pathways has largely come from advances in numerical and physical techniques that have enabled researchers to examine crystallization in nanoscale and atomic systems with single-particle resolution. Pioneering experimental and computational studies have shown that crystal growth is altered by phenomena such as nucleation of metastable phases [25, 11, 69, 7, 45], oriented attachment of crystallites [6, 35], and assistance from amorphous phase precursors [71, 46, 35, 52, 59, 38, 57, 44]. Such non-classical nucleation or growth behavior has been identified in protein crystal nucleation [67], calcite growth [71, 52, 35], tissue mineralization [46], CdSe quantum dot growth [69], iron oxide growth [6, 7], and colloidal microparticle crystallization [59]. The appearance of these phenomena across different systems in different disciplines is exciting because it implies that there may be underlying universal mechanisms at play. Their understanding could dramatically enhance our ability to control and direct crystallization of materials for a broad class of applications, such as bone growth, protein crystallization, and synthesis of functional materials. As such, the fundamental physics behind crystal growth pathways has garnered intense interdisciplinary inter-

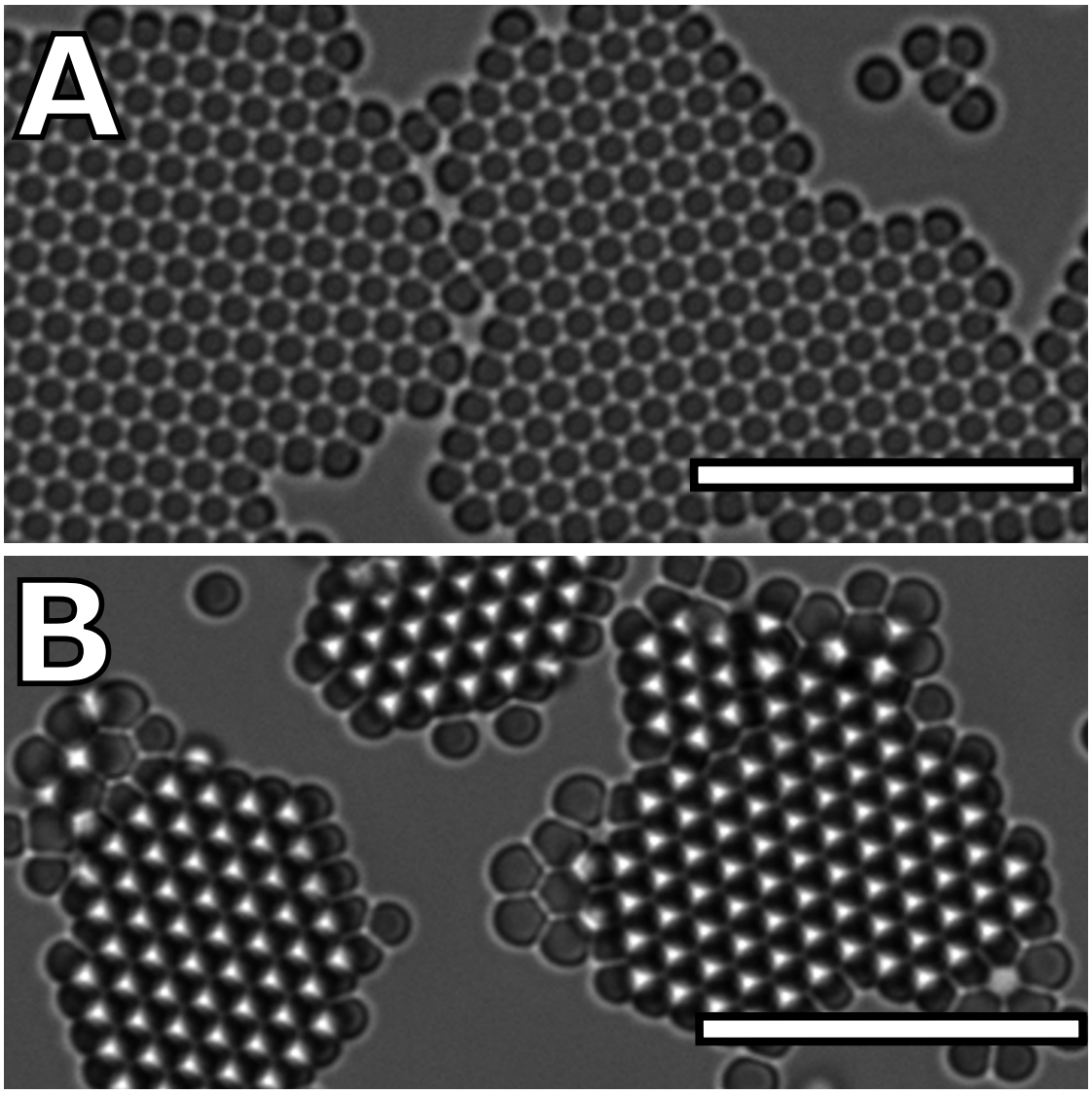

Figure 4.1: Images of monodisperse (**A**) and bidisperse (**B**) samples of crystallizing polystyrene microparticles 20 hours after nucleation. Particles on the second layer appear white, while particles in the bottom layer appear dark. Scale bar is 10 µm.

est [24, 66, 17, 70].

Probing such mechanisms in colloidal systems is particularly attractive because the particle shape, size, polydispersity, concentration and potential can be carefully controlled. Experiments on hard sphere colloids have provided

direct observations of various crystallization processes through their relatively slow single-particle dynamics, e.g., crystallization of particles under shear [1], entropically induced crystallization [53], defect propagation [61], and plastic response due to compression [41]. Beyond the hard-sphere model, studies that have included attractive interactions between microparticles advanced our ability to measure the universality of epitaxial growth rates [22], crystal nucleation and growth at low volume fraction [19], the effect of the substrate on crystal growth [60], and the formation of Wigner crystal analogues [29]. The systematic control afforded by colloidal systems enable a powerful approach for determining the fundamental drivers of crystal growth pathways [48, 24].

Here, we use a quasi-two dimensional (2D) colloidal model system to study crystal nucleation and growth at low volume fraction to determine how growth is altered by the presence of a secondary particle species. An attractive interaction between particles is provided via the depletion interaction [4] by introducing a nonionic surfactant that forms micelles whose size and concentration can be tuned with small changes in temperature as described in [58, 59]. This tuning allows control over the strength of the interparticle interaction. The system is imaged via bright-field microscopy throughout the crystallization process. Using only monodisperse particles, we observe typical nucleation, monolayer growth, and subsequent coarsening [19, 59]. Surprisingly, in the presence of a small concentration of larger particles, monolayer growth is reversed in favor of nucleation and growth of a secondary crystalline layer. Thus, we identify a new growth pathway that is catalyzed by the presence of the secondary particle species.

4.3 Experimental Methods

The solvent used in these experiments consisted of 2 mM NaCl in H_2O (Millipore). The nonionic surfactant hexaethylene glycol monododecyl ether ($C_{12}E_6$) was added at a concentration of 2.5 mM and was gently shaken until the surfactant was dissolved. Colloidal microspheres were introduced by adding an additional 2% of sample volume of polystyrene spheres suspended in water. Bidisperse samples were prepared using a mixture of polystyrene spheres with radii of r_l = 0.6 and r_s = 0.5 μm and less than 4% size polydispersity, mixed 1:10 by volume, both drawn from stock solutions of 8% solids by volume. Monodisperse samples used as a control were prepared using the 0.5 μm spheres.

Samples were pipetted into glass chambers that had been cleaned with a strong base and rinsed with methanol and DI water. The chambers were sealed and loaded onto an inverted optical microscope. Colloids were allowed to sediment for about twelve hours at 22 °C before undergoing a temperature ramp of +0.1 °C every 30 minutes until crystal nucleation was observed. Because of the temperature sensitivity of the depletant, the microscope was thermally isolated from its surroundings using a foam polystyrene box 5 cm in thickness. The target temperature of the sample was set using two PID controlled heating elements placed above and below the sample. Images of the sample were captured at 1 frame per minute for 78 hours.

Particle locations were extracted from the video data using custom software written in MATLAB based on previously developed particle tracking methods [16]. Significant effort went into implementing additional segmentation and featuring algorithms, as well as manual checks to account for optical ar-

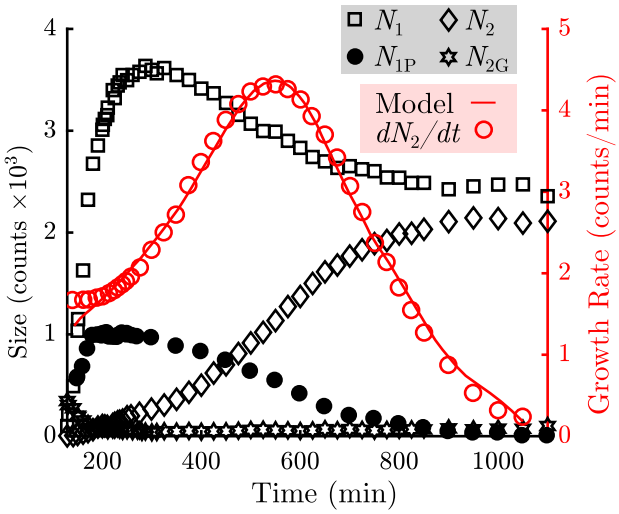

Figure 4.2: Measurement of the counts of particles in various states in the sample (Left axis, black). The number of particles in the bottom (N_1) layers are indicated by the squares. The number of particle in the top (N_2) layers are indicated by the diamonds. The number of unblocked perimeter particles (N_{1P}) are indicated by the closed circles. The number of gaseous particles promoted off of the sample floor (N_{2G} are indicated by the stars. Measurement of the growth rate of the top layer as a function of time is indicated by the open circles (Right axis, red). A fit using the simple model described in Eq. 4.1 is overlaid as a sold red line.

tifacts that arise from setting the focal plane at the second layer. Additional information on these changes can be found in Chapter 3.

4.4 Results

We observe that monodisperse solutions form single layer islands that display previously observed growth behaviors [19, 59]. Remarkably, bidisperse samples form crystals with two full layers of small particles in the same time frame. A characteristic image of the crystals formed at the end of the experiments on the monodisperse and bidisperse samples are shown in figures 4.1A and 4.1B,

respectively. Particles that reside on the glass substrate of the sample chamber appear as black circles, while particles at the height of the top layer appear white. To illustrate the evolution of the bilayer crystal morphology, we display a time lapse image of the bidisperse sample in the four panels that make up Fig. 4.1C. Within the first 400 minutes, the sample transitions from a quasi-2D gas composed of mixed large and small particles to a gas-crystal coexistence of small particles and a gas of large particles. The large particles are excluded from the solid phase of small particles and can be seen near the crystal edges. Rather than continuing to grow and coarsen, the crystal islands melt from their periphery while a second layer nucleates and grows on a subset of the islands. This simultaneous melting of the bottom layer and growth of the top layer continues until all crystal islands have either evaporated or have grown two full layers of small particles.

To quantify the growth behavior of the two crystalline layers, we measure the total number of particles in the top and bottom layers of the crystals and plot these in figure 4.2. A particle is considered part of a top or bottom crystal layer if it has at least two neighbors and a bond orientational order parameter ψ_6 value greater than 0.8, where ψ_6 is defined as $|1/N_j \sum_k \exp(6i\theta_{jk})|$, N_j is the particle's total number of nearest neighbors, and θ_{jk} is the angle between the particle and its k^{th} neighbor relative to a reference axis [36].

We observe that the number of particles incorporated into the bottom crystal layer, N_1 (black squares), rises rapidly during the first 200 minutes, during which nucleation and subsequent growth of monolayers occur. The number of particles in the bottom layer peaks at 300 minutes and then declines by roughly one-third at later times. Meanwhile the number of particles in the top crystal

layer, N_2 (black diamonds), increases monotonically. The growth rate of the top layer (red open circles) peaks at roughly 550 minutes and decays to zero when all top-layer positions are filled. In addition, we observe that particles are never promoted to the top layer from the interior of a monolayer island. We also see that once particles are incorporated into a top layer, they remain bound for the rest of the experiment.

Collectively, these observations indicate that to model the top layer growth, incorporation into the top layer crystal can be treated as a permanent adsorbing state. Thus, the top-layer growth rate should only depend on the number of elevated gas particles that can sediment onto a crystal surface, N_{2G}, and the number of particles at the periphery of the bottom layer that are not attached to stabilizing second layer neighbors, N_{1P}. The number of particles detected in these positions is plotted in figure 4.2. N_{1P} (solid black circles) follows a similar trend to N_1, while N_{2G} (black stars) contains about 300 particles at the onset of monolayer nucleation, quickly decreases by 200 minutes, and then increases to about 100 particles by the end of the experiment.

We fit the growth rate data for the top layer with a simple model of the form

$$\frac{dN_2}{dt} = k_1 N_{2G} + k_2 N_{1P} \frac{N_2}{N_1}, \tag{4.1}$$

where k_1 and k_2 are fit constants with $k_1 = 2 \times 10^{-2}$ min^{-1} and $k_1/k_2 = 3.1$. We plot this fit as a solid line in figure 4.2. We find that the first term primarily affects the initial and final growth rates. We also find that the fit is substantially improved by the factor N_2/N_1 in the second term. Once promoted to the top layer, the rate of capture into the crystal will depend on the fraction of sites on that layer adjacent to the growing crystal. N_2/N_1 represents a rough but useful approximate to this fraction. Finally, we hypothesize that the presence of the

large particles plays an important part of the mechanism for promoting particles to the second layer.

To further strengthen the link between the presence of the large particles and the promotion of particles into the second layer, we measure the lateral separation between particles in N_{2G} and their nearest large particle over 10 frames starting at 200 minutes (figure 4.3A). We find a highly structured distribution with a large peak around 1.5 particle radii, indicating that over a third of N_{2G} particles are close to, or in contact with a large particle. The remainder of the distribution appears significantly broader with a peak around 6 particle radii. We find that the overall distribution differs dramatically from a random promotion of small particles to N_{2G} from anywhere between the crystals (figure 4.3B, red). Furthermore, distributions generated by forcing particle promotion to only occur at large particle sites with subsequent diffusion (figure 4.3B, purple) are also unable to reproduce the measured data. A distribution similar to the one we observe in our experiments can, however, be generated in a simulation by promoting small particles at large particle locations, assigning each particle a random bond breaking time sampled from an exponential distribution with a mean time of 30 seconds, and allowing the particles to diffuse for the remainder of the time interval between successive frames (figure 4.3B, green). We do note that while this is a plausible mechanism, other mechanisms such as rapid promotion and demotion near large particles could also generate similar distributions. Regardless of their origin, however, the data clearly indicate that promotion occurs preferentially near large particles.

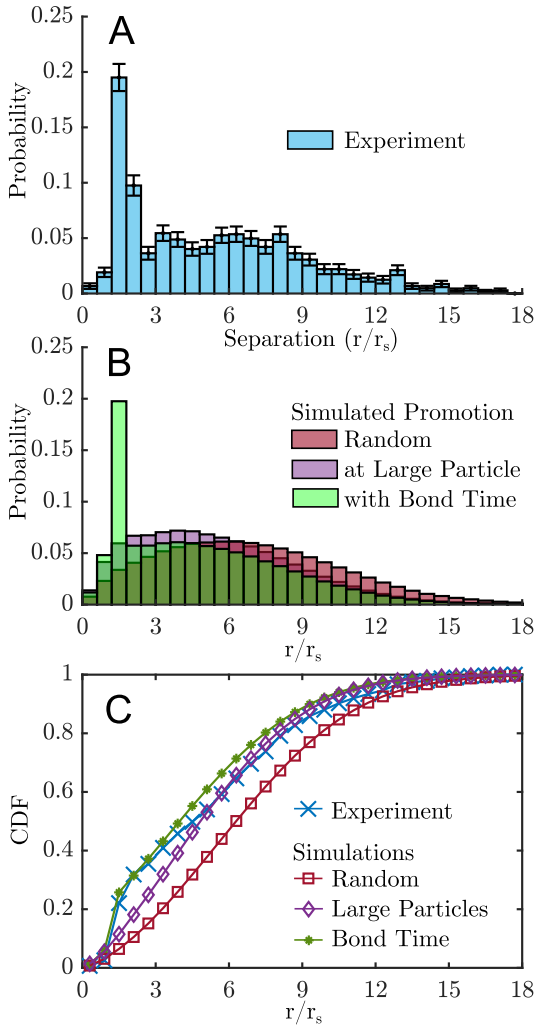

Figure 4.3: Probability distributions characterizing the separation distance between N_{2G} particles and the nearest large particle in experiments and simulations during the onset of bilayer growth acceleration. (**A**): Probability of finding a promoted particle a normalized distance r/r_s from a large as measured in the experiment. (**B**): Results of Monte Carlo simulations that randomly place particles into N_{2G} based on various rules: Particles are promoted randomly, avoiding promotion from crystalline regions (red), or promoted at the edge of a randomly selected large particle and allowed to diffuse unhindered for 30 seconds (purple). Once promoted at a large particle, a random bond breaking time, t_b, is assigned, sampled from an exponential distribution with a mean of 30 seconds (green). In this case, promoted particles diffuse unhindered for $1/f - t_b$, the remaining time between frame captures. Error bars for the simulations are the width of the bin outlines. (**C**): Cumulative distribution functions for simulations and experiment.

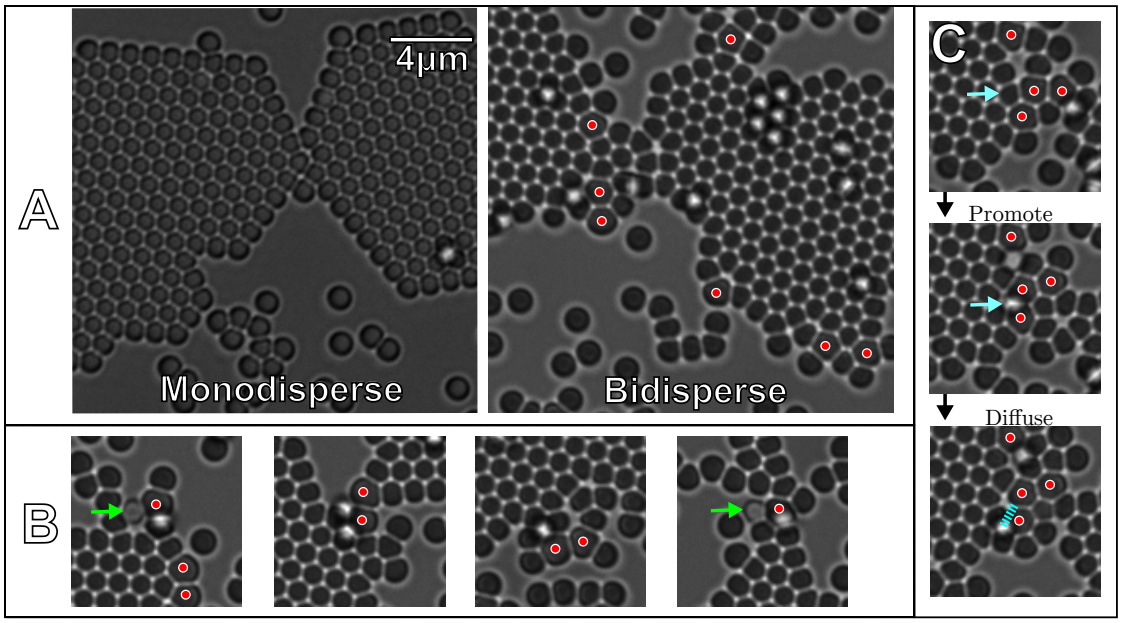

Figure 4.4: Visual evidence of solute-facilitated promotion. (A) Contrasting images of monodisperse and bidisperse crystal edges and grain boundary, capturing the disordered nature of the boundary in bidisperse samples. Red circles mark large particles. (B) Four representative images of the promotion of small particles at the crystal boundary in the presence of a large particle. Green arrows highlight particles undergoing a promotion event. (C) Time-series highlighting the promotion and subsequent diffusion of a corner particle in the presence of large particles. The blue arrows mark the location of the same particle through the first two frames, while the dashed line in the third frame denotes the displacement of the same particle.

4.5 Discussion

In this system, the lowest energy position that a particle can assume is inside the interior of a multilayer crystal. Thus, the energetically preferred structures are large, 3D, close-packed crystals. The fact that only the bidisperse sample exhibits multilayer growth indicates that the large particles are enabling an accelerated pathway to the promotion of small particles onto the crystal islands.

The puzzle that remains is to understand how this facilitation is accomplished. Here is what we know:

i. Bonds between unlike particles are approximately 10% stronger than those between two small particles, which can be calculated from the overlap volume between the depletion zones associated with particles in our experiment[39].

ii. The large particles are excluded from the monolayer crystals of small particles but remain attached to the edges of these domains. Given that there is a strong attraction between unlike species, this behaviour is what one would expect quite generically for a mixture in which the minor component is too large to be incorporated into the crystal with defects.

iii. Promotion of small particles to the second layer only occurs at the edges of the crystal islands.

iv. After promotion, the small particles exhibit a transient attachment to the large particles and so remain near the edges of the islands during this time. This is again expected due to the stronger attraction between large and small particles; on a monolayer crystal, interstitials formed with a large particle offer the deepest energy wells.

v. Once the crystal has nucleated a second layer, the promoted particles can be irreversibly captured by the growing crystal. This upper crystal layer grows, at the expense of the lower layer, until the top and bottom edges coincide. Further changes to the size of the bilayer crystals are extremely slow.

Based on these observations, we propose the following explanation of the solute-facilitated promotion of particles. The exclusion of the large particles

from crystals implies that their presence among the small particles disrupts the ordering of the latter. This being so, we can assume that some residual of that disruption remains for those small particles adjacent to the large ones around the edge of the island. In a rigorously 2D system, these interfacial small particles would have exhausted all means to further lower their free energy. In the real system, however, an option remains – interfacial particles can elevate themselves to the second layer, exchanging a strained interfacial environment for one on the upper layer, free from frustration. With this new flexibility, the promoted particles are able to take optimal advantage of the stronger attraction to a large particle and organise themselves with respect to the large particles so as to lower the free energy of the configuration. Once promoted, the presence of a surface particle atop this interface constrains any further local promotion until the particle eventually moves away, allowing the interface to participate in another promotion. Figure 4.4 highlights an observation of our hypothesized sequence of events and displays a number of instances of promoted particles remaining in association with a large particle before diffusion into the interior of the monolayer regions.

The failure of monodisperse systems to form bilayers would be explained, according to our model, by the highly-ordered character of the island edges in these systems, as demonstrated in figure 4.4A. Our model of promotion driven by interfacial frustration is quite general and suggests a number of interesting possibilities. If interfacial disruption is important, could defects in the substrates play a similar role to the large particles in facilitating promotion? Inverting the composition, so as to make the small particles the minority species, may have similar effects on the promotion of large particles. For example, after the second-layer growth decelerates, our system shows significant segregation

of large particles into their own structures, effectively leading to a local population inversion of particles. During this time, large particles can be observed undegoing promotion to the second layer in crystals of their own species, as evidenced by figure 4.1. Overall, our model suggests a new level of control over the self assembly of particles adsorbed on surfaces which we hope will inspire further research.

4.6 Appendix: Supplemental Information

A time lapse figure and a video of the frames between $200 \leq t \leq 800$ minutes were provided as supplemental information. The supplemental figure is reprinted below.

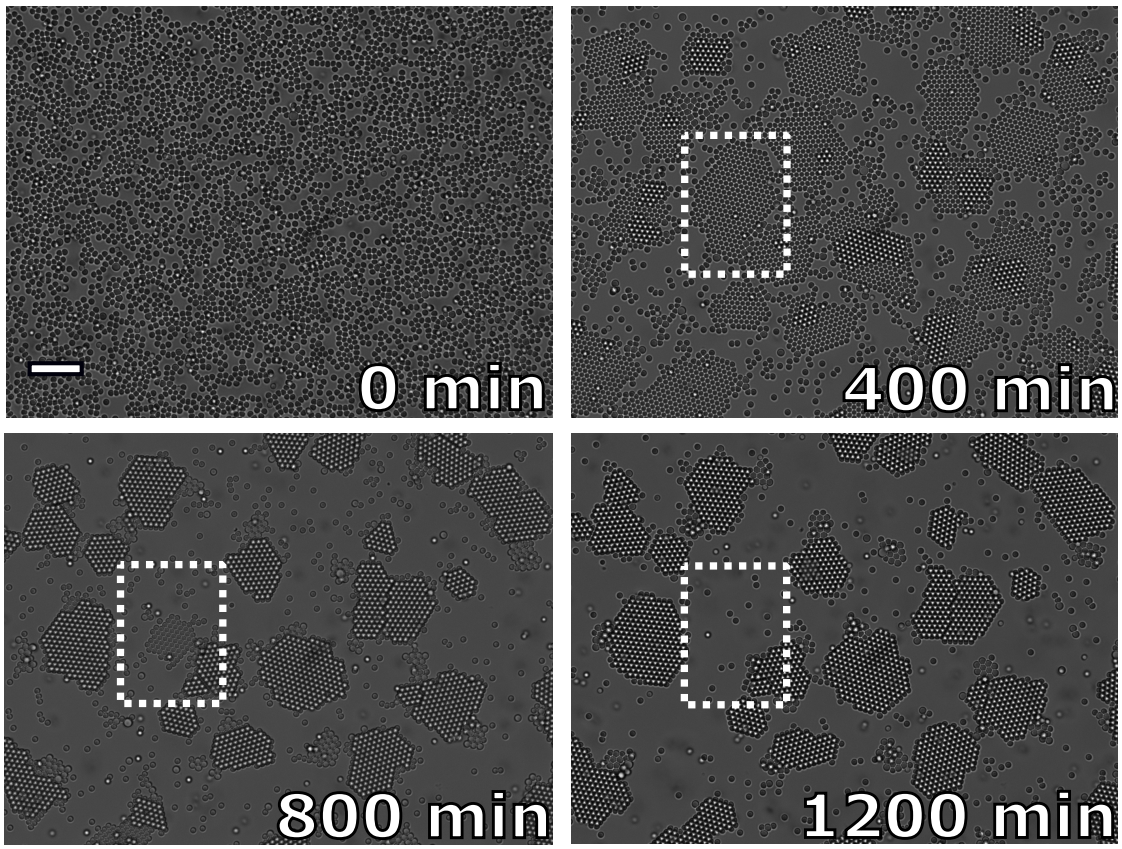

Figure 4.5: Time-lapse images of the crystallizing mixtures of binary, attractive colloidal hard spheres. Dark particles reside on the glass sample chamber. White particles are in focus, about 1 m above the black particles. At 0 minutes, we see a 2D gas of sedimented particles. At 400 minutes, the nucleation and growth of the monolayer crystals of small particles has completed, with the larger particles displaced to the periphery of the islands. In addition, we observe the nucleation and growth of a second crystal layer as indicated by the white particles. The top layers continue to grow through 800 minutes, while the exposed monolayer regions shrink. The large particles have formed monolayers of their own species at the crystal edges. The final panel shows the final configuration of the system after 1200 minutes. We see that all islands throughout the sample chamber consist of two full layers. Finally, we find that even the largest monolayer island in the field of view (dashed box) evaporates by the end of the experiment. Scale bar is 10 µm. Best viewed digitally.

4.7 Appendix: Simulating Particle Promotion

Although we measured a large peak in the measured distribution of distances between small, gaseous particles promoted off of the glass substrate and large particles, there was still an open question as to whether or not the distribution is significantly different from what one might measure randomly. If so, following the spirit of Eq. 4.1, could the distribution be explained or approximated by a simple governing rule for particle promotion? To answer these questions, we developed a brute-force Monte Carlo simulation to examine both of these questions. In the end, the simulations revealed a key insight that is a common thread in our 2D colloidal crystallization experiments[60, 22], including the experiment outlined in Chapter 5: bond breaking and diffusion must be considered together. If a particle breaks a bond but fails to diffuse away, the time spent bound is effectively increased.

4.7.1 Model

The simplest test case

The data from the experiment consists of sequential images separated 1 min in time. Images are 1388 x 1040 pixels in 12 bit grayscale. Each image has been featured and analyzed according to Chapter 3. An example frame with complete feature set is displayed in 4.6.

Let us define the set of promoted particles that add to the count of N_{2G} as **G**, and the set of all large particles as **L**. In the experiment, we measure the closest distance between each particle in **G** and all of the particles in **L**. We also

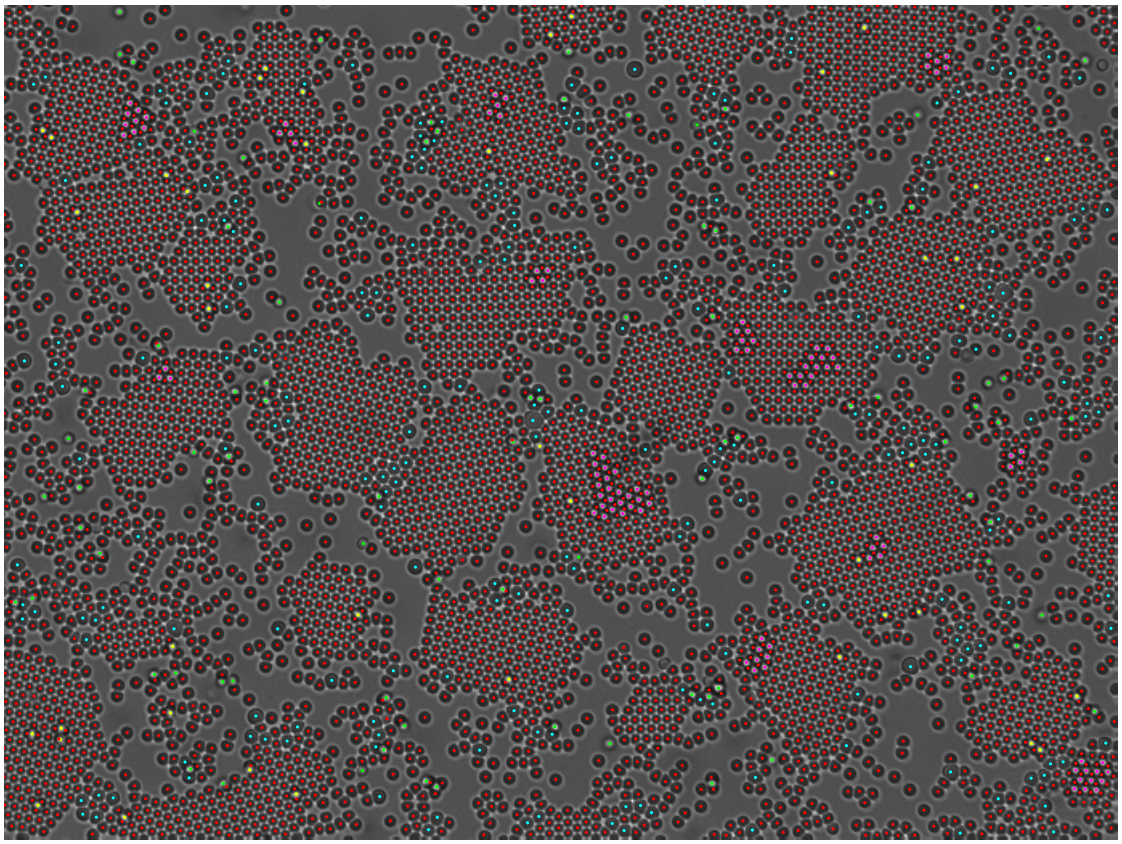

Figure 4.6: Example frame of data: frame 201. **Red**: Small particles on substrate. **Blue**: Large particles. **Green**: Gaseous promoted small particles. **Yellow**: Small particles on top of a monolayer. **Magenta**: Small particles in a second-layer crystal.

notice from observation that the number of particles that are promoted onto a crystal from inside a crystalline monolayer is negligible. Finally, we know the free diffusion coefficient for each particle, given by the Stokes-Einstein equation

$$D = \frac{k_B T}{6\pi\eta r}$$

where k_B is the Boltzmann constant, T is the sample temperature, η is the solvent viscosity, and r is the radius a particle. For this experiment, $D = 92.72\,\mathrm{px}^2/\mathrm{s}$ for a small particle. Since the frame rate of the experiment is 1 per minute, it is not possible to track each particle through time without being certain that particles

have not interchanged positions. Because of this, we look at each frame as an independent snapshot in time and measure the *distribution* of nearest distances between **G** and **L** particles.

The general idea of the simulation is to generate many new sets of **G** given the other data in a frame, allowing us to generate an 'expected' distribution of shortest distances between each **G** and **L**. To do this, we remove and regenerate **G** for each frame. In every simulation, particles cannot be promoted from within the boundaries of a crystal.

4.7.2 Random Promotion

The random promotion simulation is designed to test the hypothesis that what is seen is simply the result of promoted particles taking up random positions throughout the image – that nothing is happening.

In this simulation, |**G**| particles are generated and given random coordinates throughout the image. New particle positions are accepted if they do not coincide with the location of any other new particles or the location of a crystal island. The results of running this simulation are shown in figure 4.3.

4.7.3 Comparison to Multinomial Model

The random promotion simulations are easily checked by determining the probabilities of placing a particle a given distance away from any large particle directly from the measured data. If we assume that only one particle center can

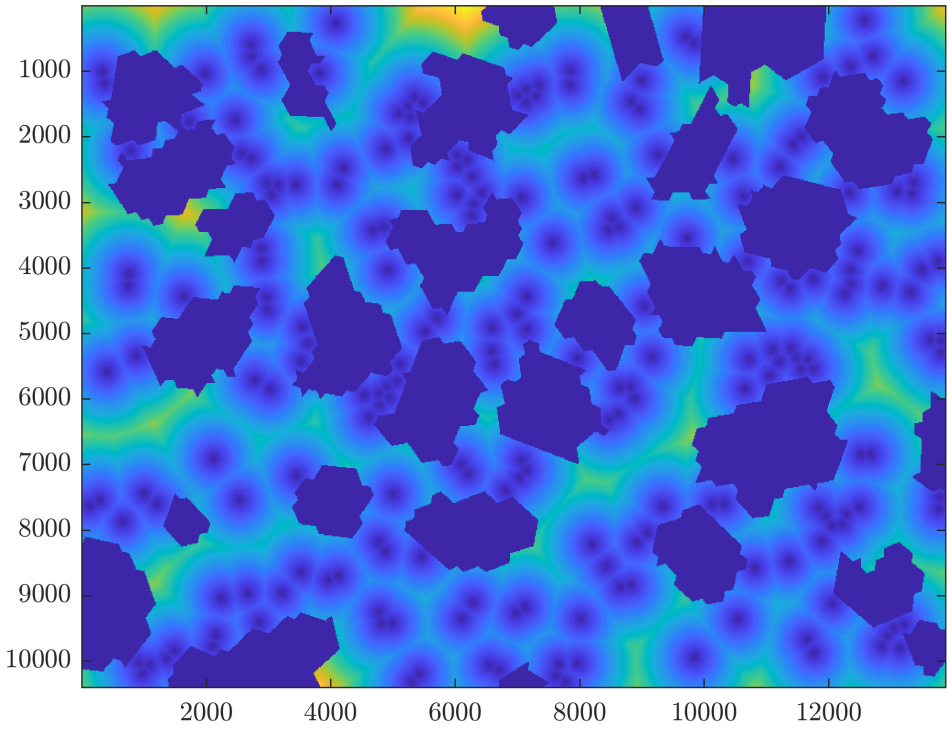

Figure 4.7: Illustration of a distance transform of **L**. Each pixel is given a value equal to the distance to the nearest large particle. Crystalline areas (large, dark purple regions) are overlaid with a distance value of -1. Axes are in units of pixels, which has been supersampled by a factor of ten from the original image. Separation distance increases as the image transitions from purple to blue to yellow.

be present in a pixel and that the locations of **L** are given for each frame, we can compute a binary image representing the locations of the centers of **L**. A distance transformation of this binary image is taken, which assigns the distance to the nearest member of **L** to each pixel. Finally, because crystalline regions are excluded from the simulation, they are overlaid on the distance transformation and given a value of -1. This results in an image similar to Figure 4.7.

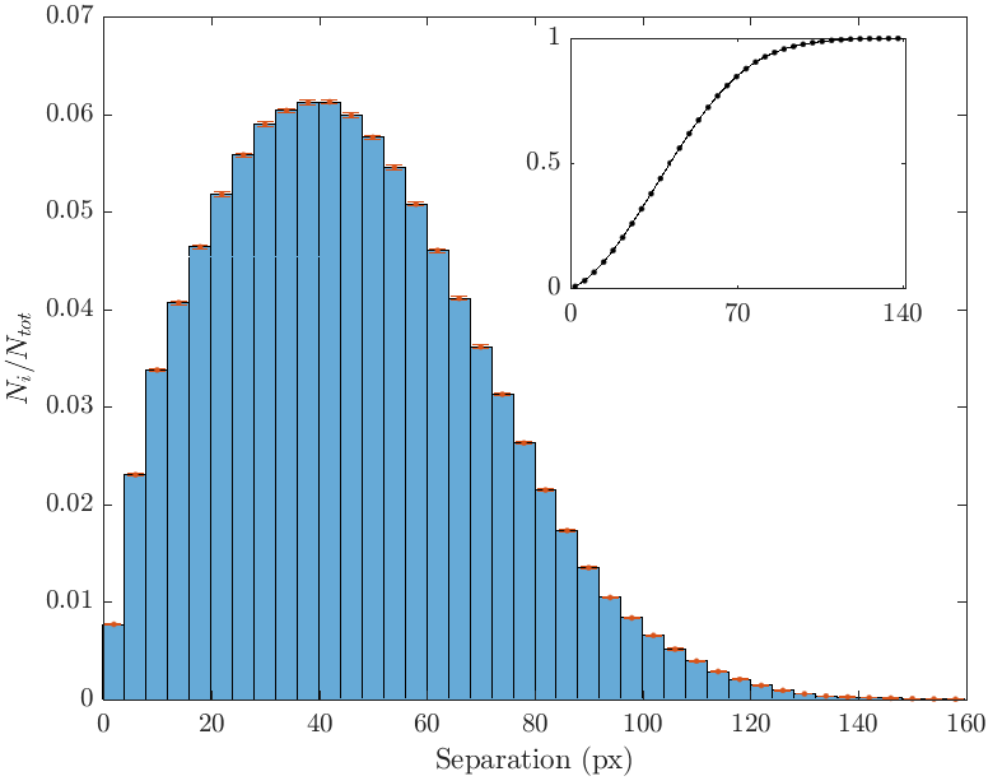

Figure 4.8: Result of simulating random placement of **G** and measuring the minimum distance to the nearest large particle across 10 minutes in time, repeated 10^5 times for each frame. **Inset**: Cumulative distribution function.

Counting the number of pixels at each distance for this image and normalizing by the number of non-negative pixels is results in the measurement of the individual event probabilities, p_k, of a multinomial distribution describing the random placement of a particle at a distance k away from any large particle. Or, in other words, the sum over each individual pixel distance is equivalent to counting the number of microstates in each macrostate that a particle could be placed into. The simulation of the random case should be equivalent to measuring the number of pixels belonging to each macrostate.

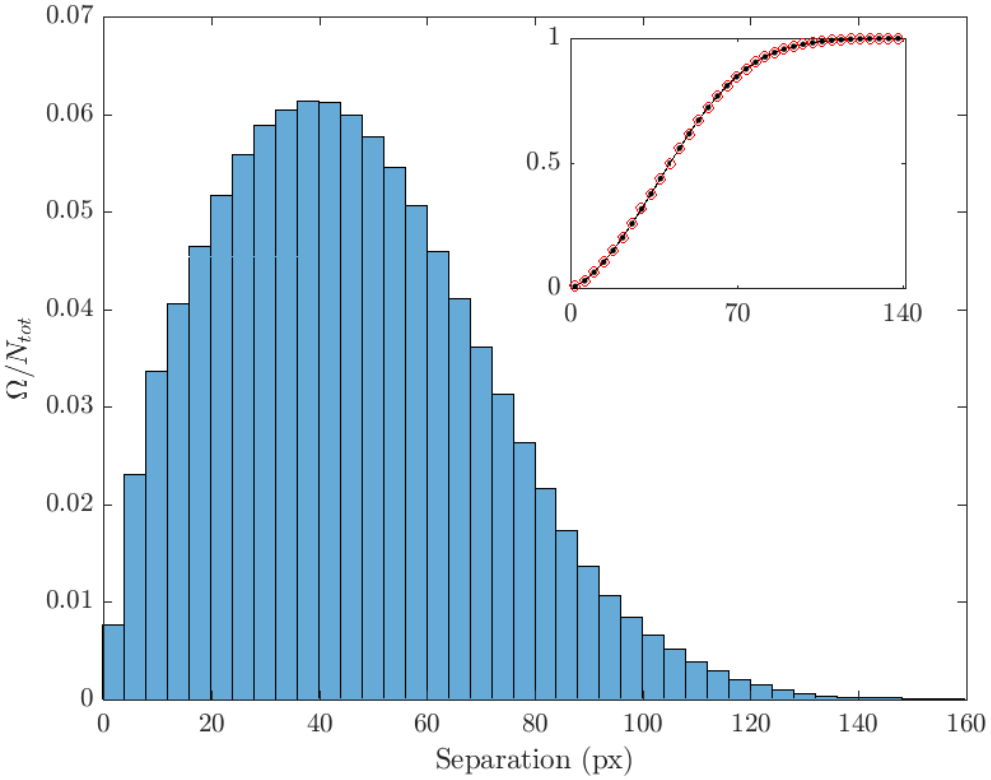

Figure 4.9: Result of directly measuring the probability to find a particle at a given separation from the nearest large particle by assuming a multinomial distribution with probability weights given by the normalized counts of pixels at each distance from Figure 4.7, taken across ten minutes of time. **Inset**: Cumulative distribution function. Notice the CDF of the measurement (red circles) and the simulation (black points) line up nearly exactly.

Figure 4.8 shows the result of the random simulation using 10^6 trials across ten frames. Figure 4.9 shows the result of the multinomial model. The results are compared in this figure via comparison of the CDF for each distribution, which line up nicely and pass the Kolmogorov-Smirnov test, indicating that these results likely share the same underlying probability distribution.

4.7.4 Promotion at Large Particles

Although an excellent test case, it is also notable that random placement of particles throughout the sample may not necessarily be a fair assumption. Particles are not promoted as frequently in the monodisperse case, where large particles are absent. To take maximal advantage of this observation, we create a simulation that assumes promotion can only occur at large particle locations. Once promotion occurs, the particles are free to diffuse unimpeded.

This simulation accomplishes this task through the following sequence of events: for every **G** to be placed, place one at the edge of a randomly selected particle. Then, sampling from the probability distribution

$$P(x|\sigma) = \frac{1}{\sqrt{2\pi\sigma^2}} \exp(-\Delta x^2/2\sigma^2),$$

where $\sigma^2/2 = Dt$, randomly select a set of two independent (x,y) values to acquire the new position of the particle after t seconds of unimpeded diffusion. To account for the effect of particle interactions leading to an effective lowering of the diffusion constant, we also swept over values of D. The result of the simulation using the experimental system's parameters is given in Figure 4.3.

It is worth noting that increasing D leads to a flattening of the probability distribution, approaching the result of the random case, while decreasing D sharpened the distribution. It is possible to recover a large peak at contact distance, such as the one measured from experiment, with small values of D, such as $D \leq 10px^2/s$ but the entire PDF decays to zero over a shorter range than measured experimentally. This makes sense, as extremely small D should lead to a single Gaussian-like distribution of distances at the contact length, as particles have no chance to diffuse away. The probability of finding these particles

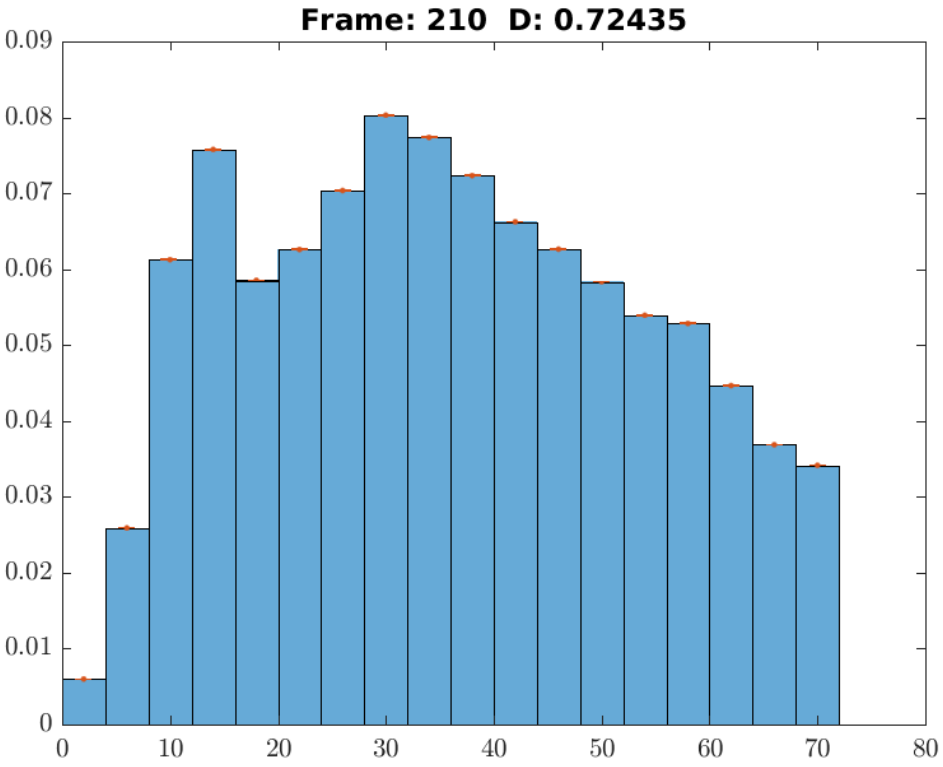

Figure 4.10: Example of simulation results for a single frame (210) assuming that particles must begin their diffusion at the edge of a crystal. Note that the diffusion constant in this run is extremely small, equating to a diffusion length of 6 px between frames. Thus, promoted particles are highly localized at crystal boundaries. The experimentally observed strong peak (20% at contact between large and small particles) cannot be reproduced with this promotion rule.

farther than the contact length necessarily goes to zero quite quickly in this case.

4.7.5 Promotion at Crystal Edges

We ran our simulations with a particle placement rule that only allowed placement of **G** near a crystal edge, with subsequent diffusion away from the edge.

This was done using the same probability distribution for free diffusion given in the previous section. Starting locations for promoted particles were selected by picking a random position along a random edge of a random crystal. The diffusion constant D was again varied to account for possible adjustments to the average value of D due to particle interactions. The results were not appreciably different from the case where particles were promoted at the locations of large particles. This is perhaps unsurprising in hindsight: large particles are found near crystal edges. Large diffusion constants allow the small particles to sufficiently randomize their positions such that the difference between starting near a large particle and starting near the edge of a crystal is essentially negligible.

For smaller diffusion constants, particles do not have much time to diffuse *toward* large particles. Looking at the distance transform in Figure 4.7, you can see that most crystal edges are within two diameters of a large particle – 30 pixels, and many areas have large particles directly attached to the edges. There should be elevated counts around roughly 30 pixels in this case. To illustrate this, I show the results of simulating this behavior for a single frame for $N = 10^5$ trials in 4.10.

4.7.6 Promotion with Bond-Breaking

The key to recovering both the strong peak at contact between large and small and the longer timescale decay seen in the experimental data is to account for the fact that particles will often fail to diffuse away from whatever they were bonded to. In other words, the particles we are interested in take a non-negligible amount of time to break bonds and to diffuse to their next location.

Furthermore, there are so few particles undergoing this process – approximately 100 in each frame – that a handful of deviations from "average behavior" can become a significant number of overlooked events in the sample.

We assign each particle in **G** a random bond-breaking time, t_b, sampled from an exponential distribution

$$p(t|\lambda) = \lambda \exp(-\lambda t),$$

with a mean of $\lambda^{-1} = 30\,\mathrm{s}$. Because we are simulating the diffusion of particles between snapshots in a video, we assume that the amount of time a particle can diffuse after successfully breaking its bonds is $t = 1/f - t_b$, the remaining time until the next video frame is captured. If t_b exceeds 60 s, the particle is promoted and remains stationary. If $t_b = 0$, the particle diffuses uninhibited for the full 60 s. This simulation is run with the constraint of only promoting near large particles as in Section 4.7.4.

It is important to note that t_b really represents a "time since last successful bond breaking." This model cannot capture the difference between a particle breaking its bonds at $t = 0$, reforming and breaking bonds with other particles until freely diffusing at $t = t_n$, versus a particle simply breaking its bonds and successfully diffusing away at $t > t_n$. In fact, this does not capture the difference between a particle being promoted at t_0, reforming a bond with the substrate, and a *new* particle taking its place by a successful promotion at $t > t_0$. In this sense, this is modeling the "average time left to diffuse" as a value drawn from a random process, where the details of what happened along the lifespan of a promoted particle are unimportant. These details are necessarily swept away: what we care about are the particles that are free to diffuse once the next frame

ready to be captured.

This model successfully captures the strong peak at contact between particles in **G** and **L**, and does decently well at capturing the behavior of the sample for longer separations when compared to the other models. The reason it captures the behavior near contact is because of the subset of **G** that has relatively large bond-breaking times, effectively keeping some promoted particles localized near large particles. Determining a more exact distribution to model bond breaking and subsequent diffusion will govern the behavior at longer separation distances more finely, but we believe that these simulations outline the key components to consider when looking to perform future studies of this system.

CHAPTER 5

MELTING ON SQUARE AND TRIANGULAR LATTICES

Before I joined the Cohen lab, an experiment measuring the melting dynamics of colloidal crystals with square and triangular lattice symmetry was performed. Analysis of this experiment eventually stalled. When I joined the lab, I initially worked on droplet breakup projects, but I found the colloidal crystallization experiments quite interesting. John Savage presented me with data from the stalled experiment, which became my first foray into colloids. This chapter briefly outlines the project, as well as my contribution to the theory and analysis. I presented my results at the 2011 Gordon Conference on Thin Films and Crystal Growth Mechanisms.

5.1 Experiment

Samples were prepared as outlined in Chapter 2.2, with $C_{12}E_6$ used as a depletant and 1.0 μm silica particles. The glass chamber floor was patterned with square and triangular lattice sites. Particles were sedimented overnight, with many taking residence inside the patterned lattice, effectively forming the outer layer of a bulk crystal. Holographic optical tweezers were used to fill the gaps in the patterned substrate and build a second crystal layer of 55 particles on top of the patterns.

While being trained as a new graduate student, I was given the data from this experiment, which showed a substantial difference in melting rates on different facets of a colloidal crystal (see Figure 5.1). The result was quite clear:

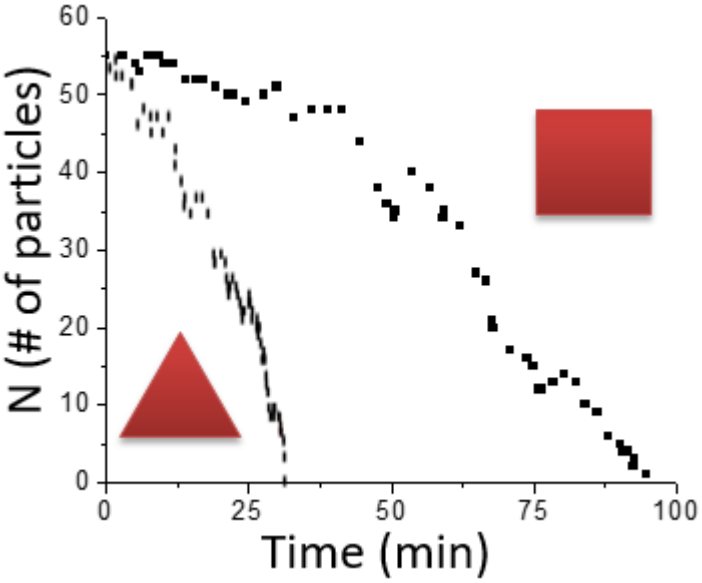

Figure 5.1: Melting time for particles in square versus triangular lattices. The number of particles in the triangular lattice is plotted with thin vertical lines, while the number of particles in a square lattice is plotted with squares. The plot illustrates that it takes about 3 to 4 times longer to melt particles in a square lattice than it does for triangular lattices.

square-symmetric crystal faces take about three times longer to melt than their triangular counterparts.

5.2 Theory

Perhaps the first direction to look for a solution to the question of why a certain crystal facet would melt faster than another would be to consider the energetics of the surfaces in question; the surfaces that provides more bonds should melt more slowly than the surfaces that provide less. As it turns out, the same physics behind dynamic Ehrlich-Schwoebel barriers in colloidal systems[22] likely governs the melting dynamics of colloidal crystal facets as well.

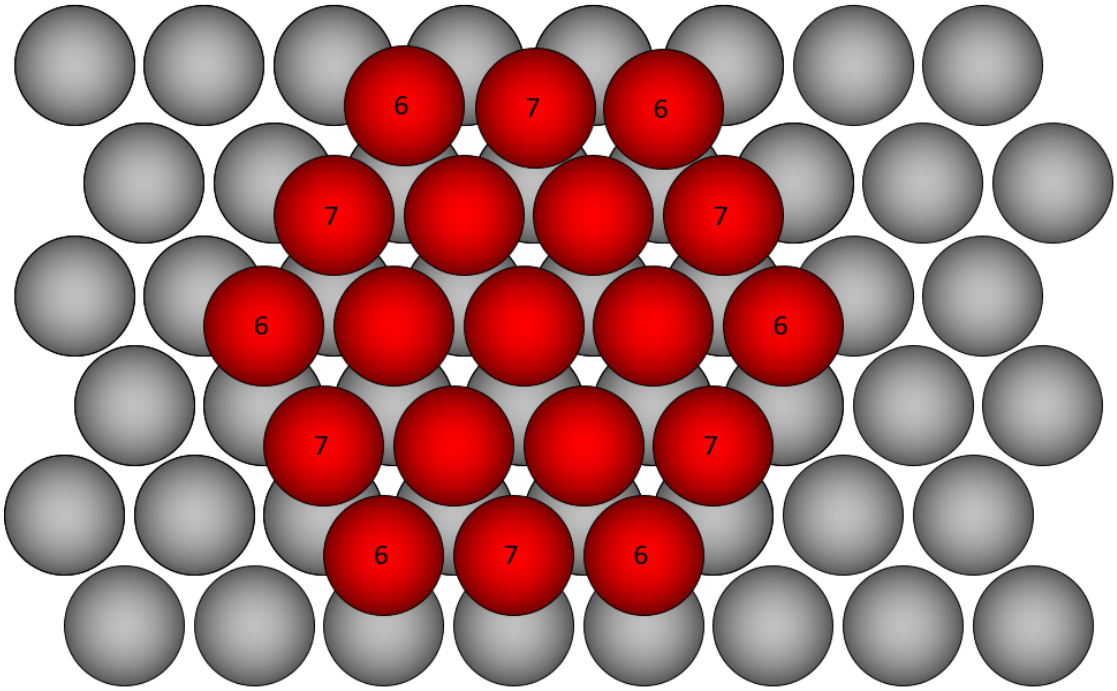

Figure 5.2: Nearest neighbor count for particles on the edge of a facet of hexagonal symmetry. Each particle has three nearest neighbors contributed from the underlying crystal layer, while corner particles have three neighbors in-plane and edge particles have four. Thus, corner particles have six nearest neighbors, and edge particles have seven.

5.2.1 Bond Energies for Interstitial Particles

Because the interaction length is at most 30 nm due to the size of the depletant, only the nearest neighbors of a particle may form bonds with it. Bonds between these particles depend only on the size of the particle and their separation. We assume that all particles in a lattice are of equal size and that they do not deviate from their equilibrium lattice position while at a lattice site. This allows us to equate the number of nearest neighbors to a particle with the number of bonds to that particle.

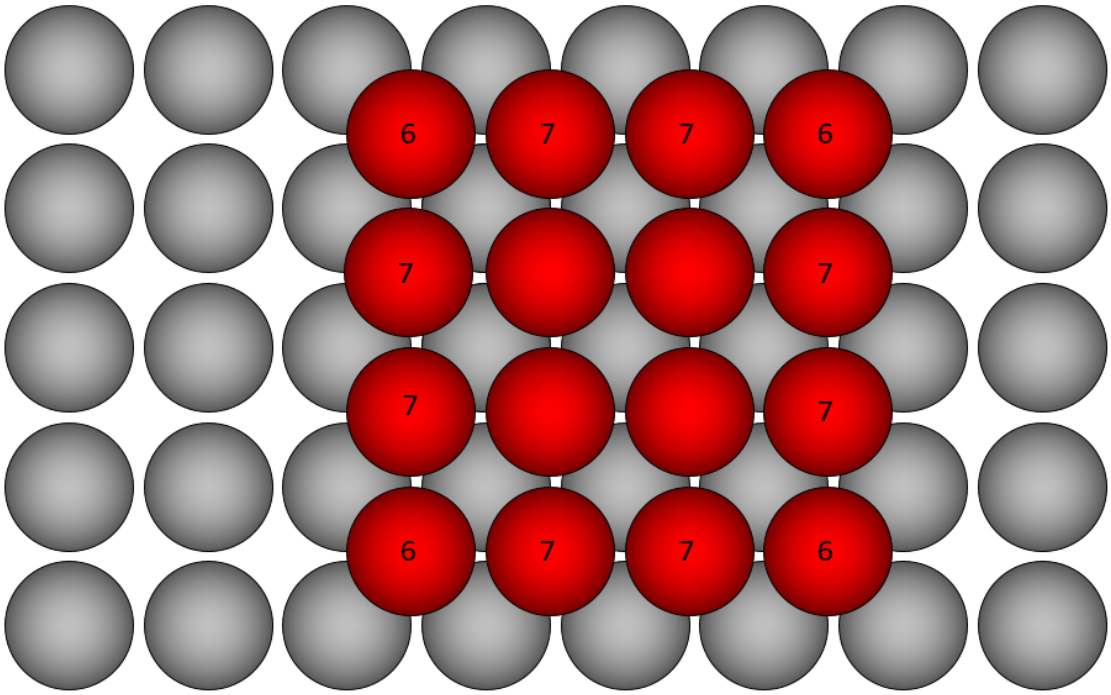

Figure 5.3: Nearest neighbor count for particles on the edge of a facet of square symmetry. Each particle has four nearest neighbors contributed from the underlying crystal layer, while corner particles have two neighbors in-plane and edge particles have three. Thus, corner particles have six nearest neighbors, and edge particles have seven, just like in the hexagonal lattice.

Let us first consider a colloidal adatom that is part of the edge of an exterior hexagonally-symmetric layer of an infinite bulk crystal. For a perfectly formed layer, there are six corner sites possessing six nearest neighbors. Edge particles other than these corner sites all possess seven nearest neighbors. This is illustrated in Figure 5.2.

On a surface with square symmetry, the same end result is true: 6 bonds at corner sites, 7 bonds at edge sites. However, the contribution of the substrate and in-plane neighbors changes. There are always four nearest neighbors in the substrate layer, which in turn reduces the possible number of in-plane neighbors

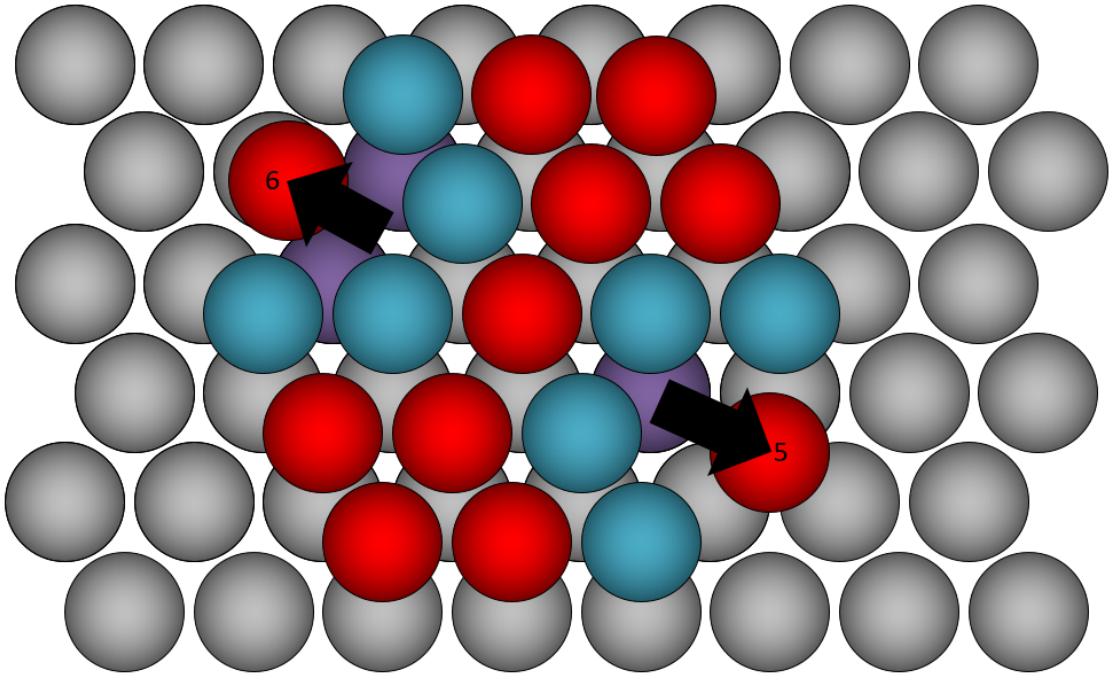

Figure 5.4: Example of removing a particle from the edge of a triangular lattice. Depending on the stacking orientation, removing a particle requires breaking either five or six bonds, as denoted by the number inside the particle being removed. Moving an edge particle always breaks four bonds in-plane (teal) and either one or two bonds with the substrate (purple).

to two for corners and three for edges. This is illustrated in Figure 5.3.

The prevailing idea at the time was that, barring corner particles, removing a particle from the edge of a square lattice required breaking five bonds, while doing the same on a triangular lattice required breaking at *at least* five bonds, depending on the stacking orientation of the second layer on top of the first layer. Examples of the triangular and square lattice bond-breaking scenarios are shown in Figures 5.4 and 5.5, respectively. Ultimately, because the triangular lattice has a higher bond density, we would expect that the triangular lattice would take more time to melt.

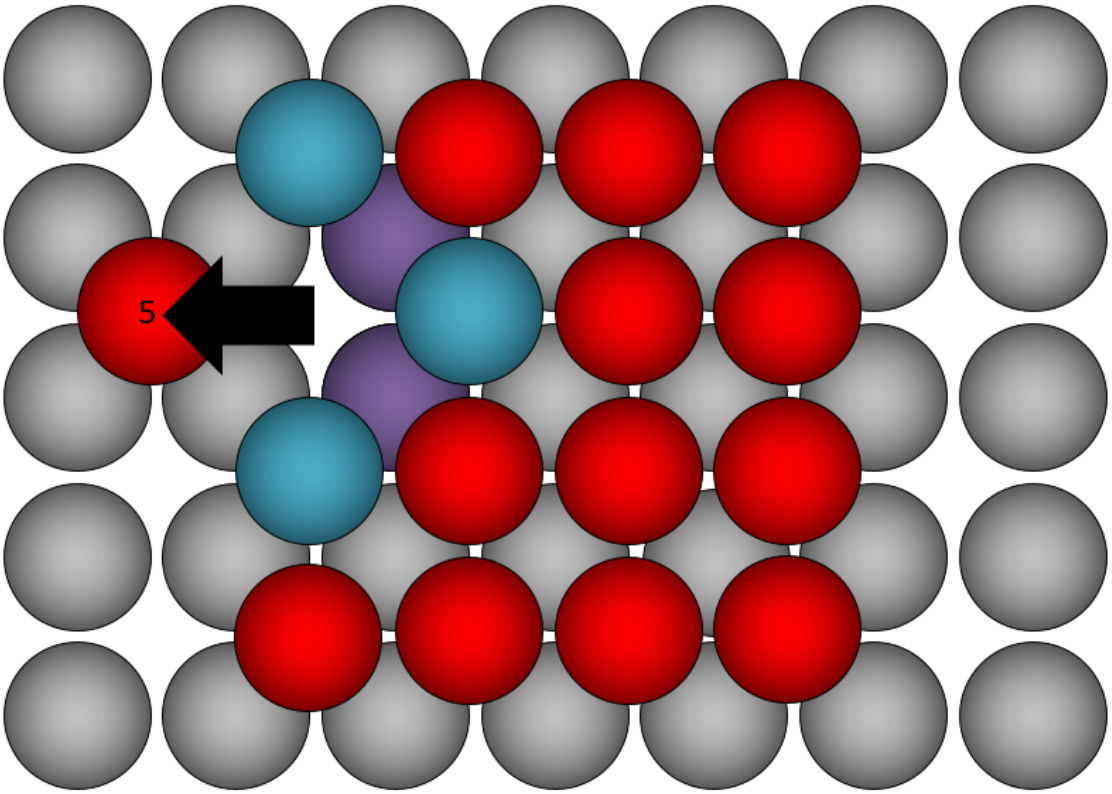

Figure 5.5: Example of removing a particle from the edge of a square lattice. Moving an edge particle always breaks three bonds in-plane (teal) and either two bonds with the substrate (purple).

The issue with the prevailing idea is that it ignores the preference for melting to occur at corners due to the lower local bond density. Furthermore, it ignores that the removal of an edge particle creates two corner particles, compounding the issue of ignoring corner particles. Finally, the observable dynamics of the system are ignored: particles almost never diffuse over the top of an underlying particle, as shown in Figure 5.6. This means that the melting pathway on a triangular lattice that involves breaking six bonds is not only more difficult to do energetically, it's also unlikely to occur because of dynamics.

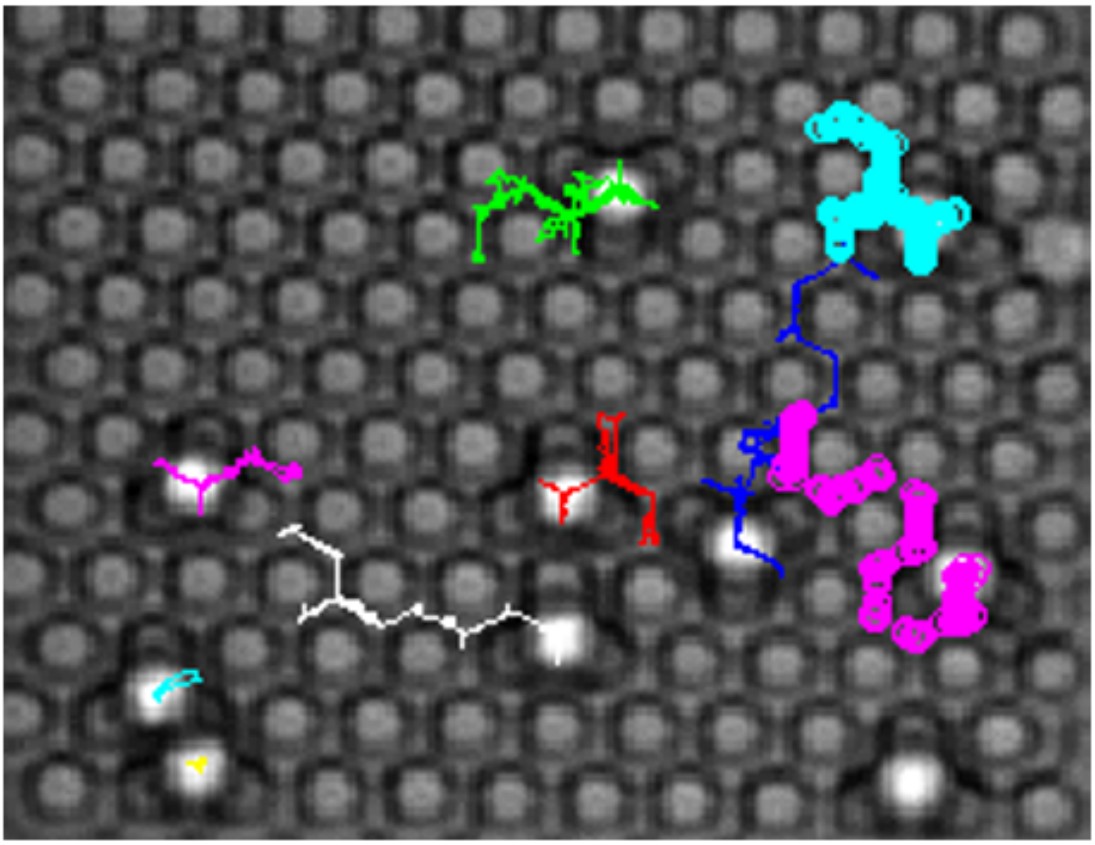

Figure 5.6: Post-processed image showing the diffusion paths of nine surface adadtoms on a triangular lattice after five minutes. The 10th particle on the far bottom-right, diffuses out of the frame and is not tracked. The paths illustrate that it is very rare for a particle to diffuse out of its trough and thus over an underlying particle to a new interstitial site. Particles are 1 μm in diameter.

5.2.2 Diffusion Path on Different Lattices

The idea that, given a massive lattice, melting from an edge dominates over corner melting because of the sheer number of edge particles vs corner particles is misleading. If the rate of melting from a corner was slow, it could *only* be due to the number of corner particles available to melt, as they are always more loosely bound than their edge counterparts. Removing the initial corner parti-

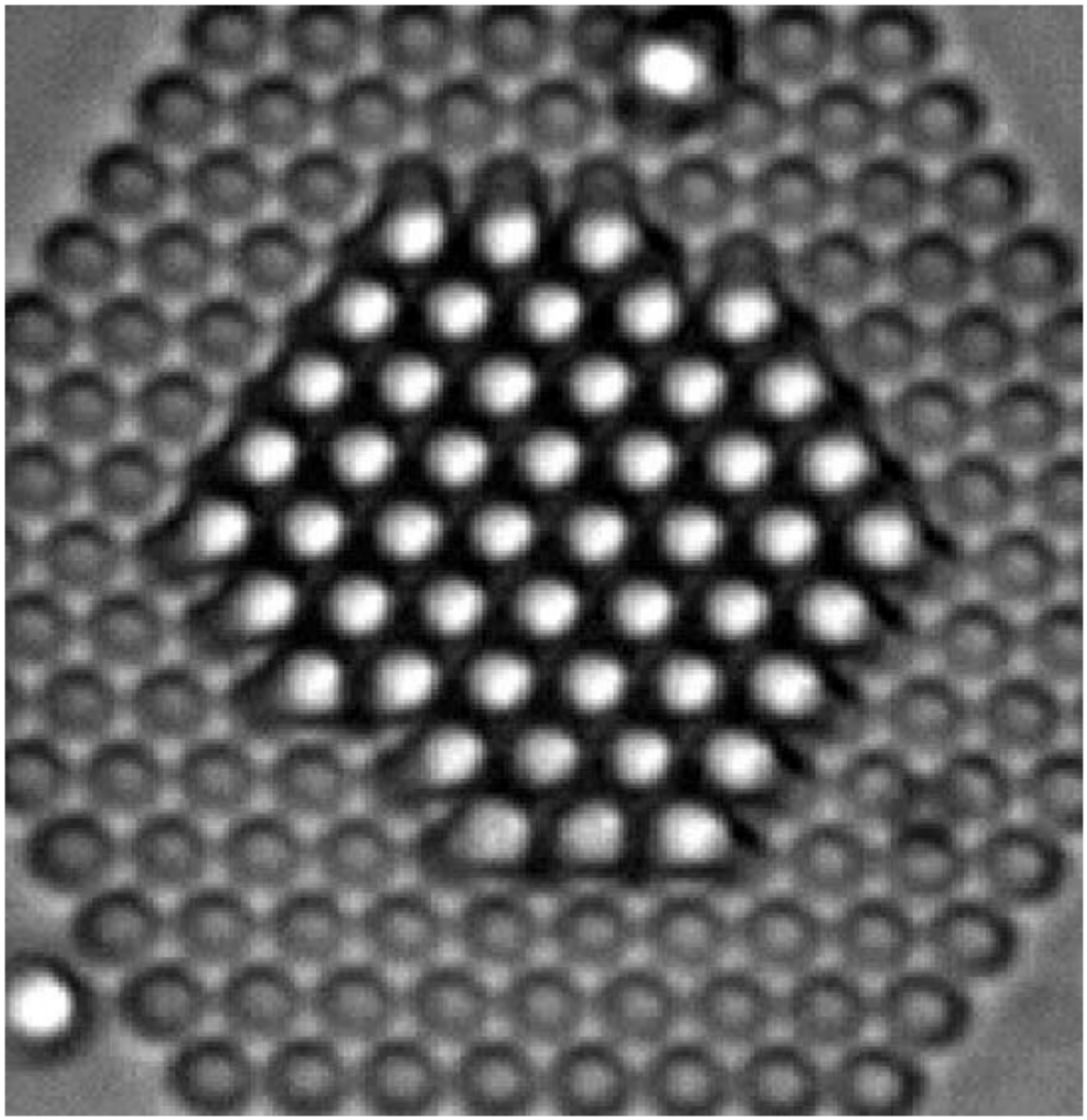

Figure 5.7: Observational evidence of preference for corner melting. Image from the early stages of an experiment on melting a 52-particle hexagonally-symmetric crystal facet composed of 1.0 μm particles.

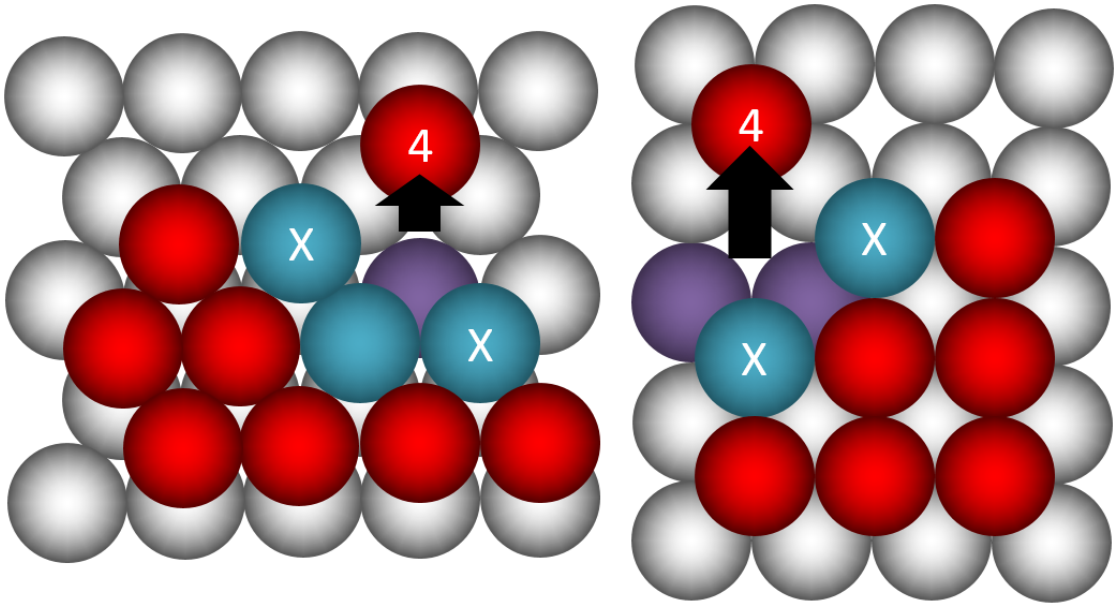

Figure 5.8: Number of bonds broken via moving corner particles. Moving a corner particle on either lattices requires breaking only four bonds. Furthermore, removing either a corner or edge particle can create up to two new corner particles, denoted by an "X". Particles whose bonds are broken in-plane with the removed particle are colored teal, while substrate particles that lose bonds are colored purple.

cles doubles the number of corner sites. Removing an edge particle increases the number of corners by two. Eventually, the effect of melting from a corner must dominate.

In addition to this quick argument, consider the actual data collection from a hexagonal crystal of 52 particles, as in Figure 5.7. There are 18 edge particles and 6 corner particles in the full lattice: 1/3 of the outer particles are corners[1]. This is far from the limit where the number of corners is far greater than the number of edge particles.

[1]You may want to consider that all corner particles are technically edge particles, which means that 6 of 24 (25%) of edge particles are corners. The point still holds: the crystals in our experiments do not contain orders of magnitude more edge particles than corner particles.

With the previous arguments being so, I make the assumption that melting occurs primarily from the corners of a crystal for each lattice and look at the difference in the number of bonds broken when moving a corner particle on both lattices. As it turns out, it is the same for each lattice – four – as shown in Figure 5.8.

Using a simple Arrhenius equation to model bond breaking on a lattice, we can write the frequency of successful bond breaking as

$$f = f_0 \exp\left(\frac{-E}{k_B T}\right), \tag{5.1}$$

where f_0 is the attempt frequency, E is the activation energy required for a particle to break its bonds, k_B is the Boltzmann constant, and T is temperature. Inverting the equation gives us the average residence time of a particle, given by

$$\bar{t} = t_0 \exp\left(\frac{E}{k_B T}\right), \tag{5.2}$$

where $t_0 = f_0^{-1}$. Assuming that the attempt frequency is equivalent in both systems, each corner particle needs to break four bonds to hop to the next lattice site, and the energetics alone would dictate that the average residence time for a particle at the corners of these lattices should be equal.

Because microparticles diffuse much more slowly than atoms or small nanoparticles, it is not enough to consider only the bond breaking energies when describing an adatom hopping around a lattice, a fact made clear by the laboratory's work on dynamic Ehrlich-Swoebel barriers[22]. The time it takes for a particle to successfully diffuse to another interstitial site must also be explicitly taken into account when describing the hopping rate of colloidal particles.

To do this we can focus on the attempt frequency, separating out a factor that depends on the path length a particle must successfully diffuse without returning to its origin and reforming the previous bonds. This describes a "first passage" process, where we are interested in the average amount of time it takes to diffuse from one lattice site to another. Given a diffusion constant of D, the average time to diffuse a length L is given by $L^2/2D$[54]. We reformulate the inverted Arrhenius equation as such:

$$\bar{t} = C\frac{L^2}{2D}\exp\left(\frac{E}{k_B T}\right), \tag{5.3}$$

where the path length dependence is factored out of t_0 such that $t_0 = CL^2/2D$. The prefactor, C, is still unknown, but again assumed to be equal for both systems. To make a comparison on each lattice, I take a ratio of the average residence time of a corner particle on a square lattice and the average time on a triangular lattice:

$$\frac{\bar{t_\square}}{\bar{t_\triangle}} = \frac{L_\square^2}{L_\triangle^2}\exp\left(\frac{E_\square - E_\triangle}{k_B T}\right). \tag{5.4}$$

Noting that the activation energies $E_\square$ and $E_\triangle$ are equivalent, this reduces to

$$\frac{\bar{t_\square}}{\bar{t_\triangle}} = \frac{L_\square^2}{L_\triangle^2} \approx 3.2, \tag{5.5}$$

which is consistent with the melting time difference seen in Figure 5.1.

5.3 Patterned Substrates

5.3.1 Background

While a graduate student in the Cohen lab, my CNF mentor Professor Sharon Gerbode developed a method for patterning an inverse lattice layer into

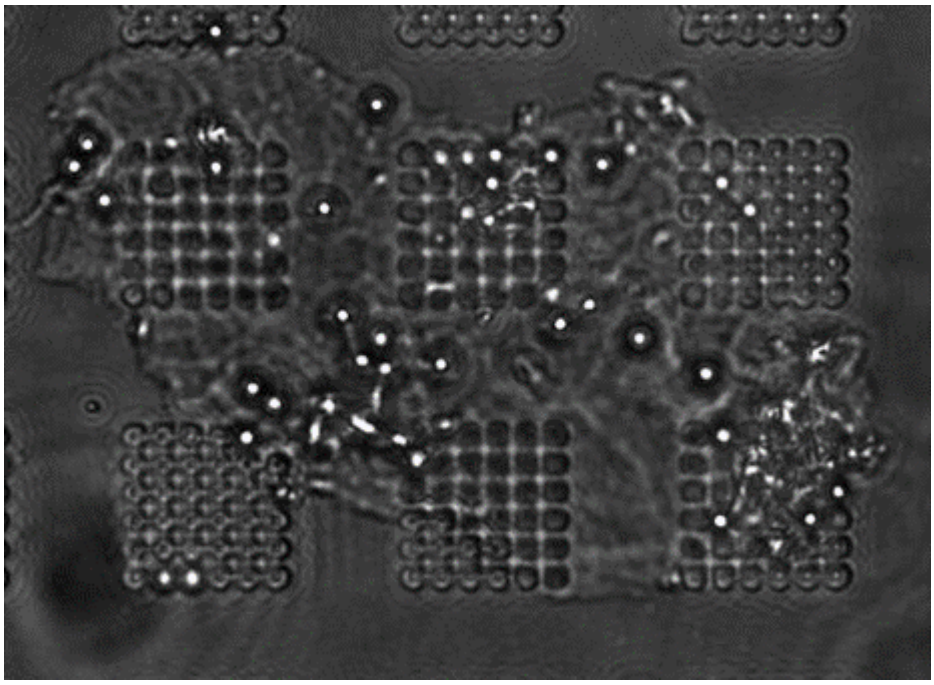

Figure 5.9: Image of patterned glass substrate after being cleaned and reused multiple times. Patterned circles are 1 μm in diameter. A clear amorphous blob of stuck material can be seen inhibiting access to patterned regions of the sample, effectively rendering our device useless. This is particularly bad, because the glass substrates were developed for the express purpose of being reusable for many experiments.

poly[methyl methacrylate] (PMMA) or glass substrates[26] using electron beam lithography. This granted us the choice of square or hexagonal lattice symmetry as well as the ability to artificially introduce strain by varying the lattice constant. After Sharon's graduation, the VB6 Electron Beam Lithography tool was retired from CNF, with a JEOL 6300 taking its place.

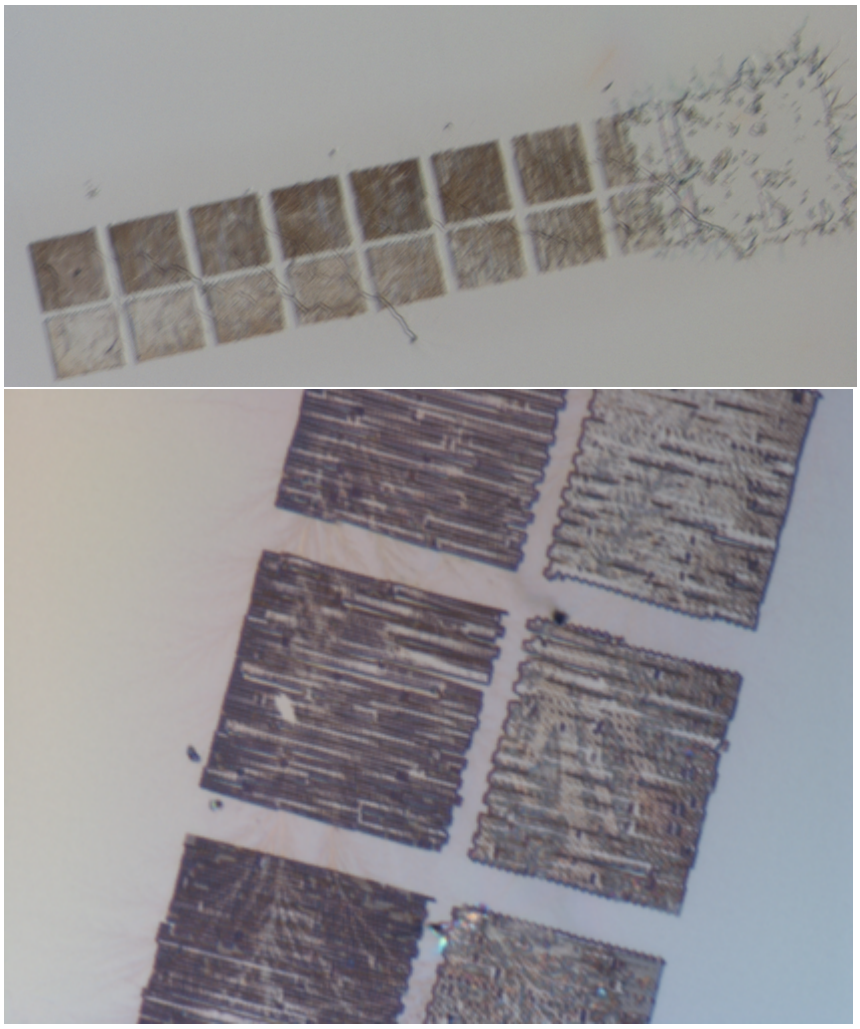

Figure 5.10: TOP: Optical transmission micrograph of arrays of 1.0 μm holes in PMMA on a glass substrate. Each square is 100 μm x 100 μm. In the top row, holes are arranged in a triangular lattice. In the bottom row, holes are arranged in a square lattice. Dosage is set to 100 $\mu C/cm^2$ at the top row of the image and decreases by $\mu C/cm^2$ for each subsequent row. Notice that the pattern appears patchy at lower exposures and is destroyed at higher exposures. BOTTOM: Close-up of the central patterns from above.

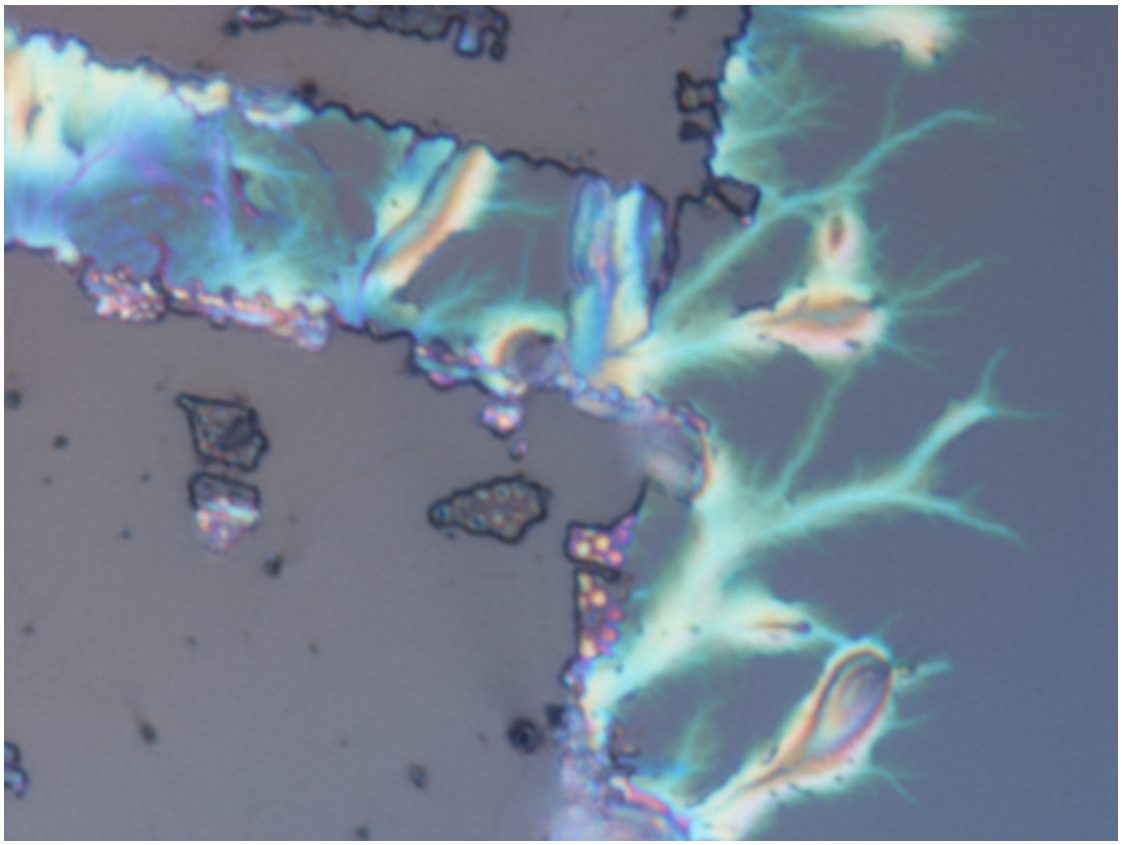

Figure 5.11: Reflected light micrograph of high beam current region of patterned substrate. Much of the feature layer has been destroyed. Colors arise from the change in PMMA thickness. Tree-like branching is similar in appearance to Lichtenberg figures, characteristic of damage due to electrical discharge. Small, colored circles roughly in the image center are 1.0 μm in diameter.

5.3.2 Problems with Previous Process on New E-Beam

After a few repeated uses, I found that our patterned glass substrates were not as reusable as we expected. Clumps of dissolved materials became trapped in the sample chamber, blocking important regions, as shown in Figure 5.9. Creating new substrates was not an easy task, however, since the electron beam lithography tool used to make the previous patterns was no longer available.

Having been trained in the nanofabrication facility, I generated new CAD patterns and machine instructions compatible with the JEOL 6300 and attempted to fabricate a substrate following the previous laboratory recipe, which failed. Figure 5.10 displays an optical image of results of a dosage test-run for the JEOL 6300. Beam current is set to 10 nA. Each pair of squares (columns) has equal dosage. At the left of the image, the dosage is 100 $\mu C/cm^2$, increasing 100% for each successive pair, up to 1000 $\mu C/cm^2$. Although the maximum dosage is equal to the dosage delivered by the VB6, extensive sample damage is observed. Reflected light microscopy reveals colorful patterns at the edges of the most damaged regions of the sample, extending into the other patterned surfaces nearby. The patterns observed are similar to Lichtenberg figures[40], which are characteristic of electrical discharge through an insulating material. To rectify this, I added additional sample processing steps to ensure that the PMMA-layered glass substrates would not be blown apart due to accumulation of charge from the E-Beam.

5.3.3 Modifications to Fabrication Process

After spin-coating PMMA to the desired thickness on a glass coverslip, I evaporate a layer of Al roughly 20 nm thick on top of the sample using the CHA Evaporator. This provides a conducting layer, which is then grounded with sample clips inside the E-Beam before patterning. The sample is exposed with the same parameters, and then washed in a strong base to remove the aluminum layer. The PMMA film is developed as usual. The results of the modified process are shown in Figure 5.12.

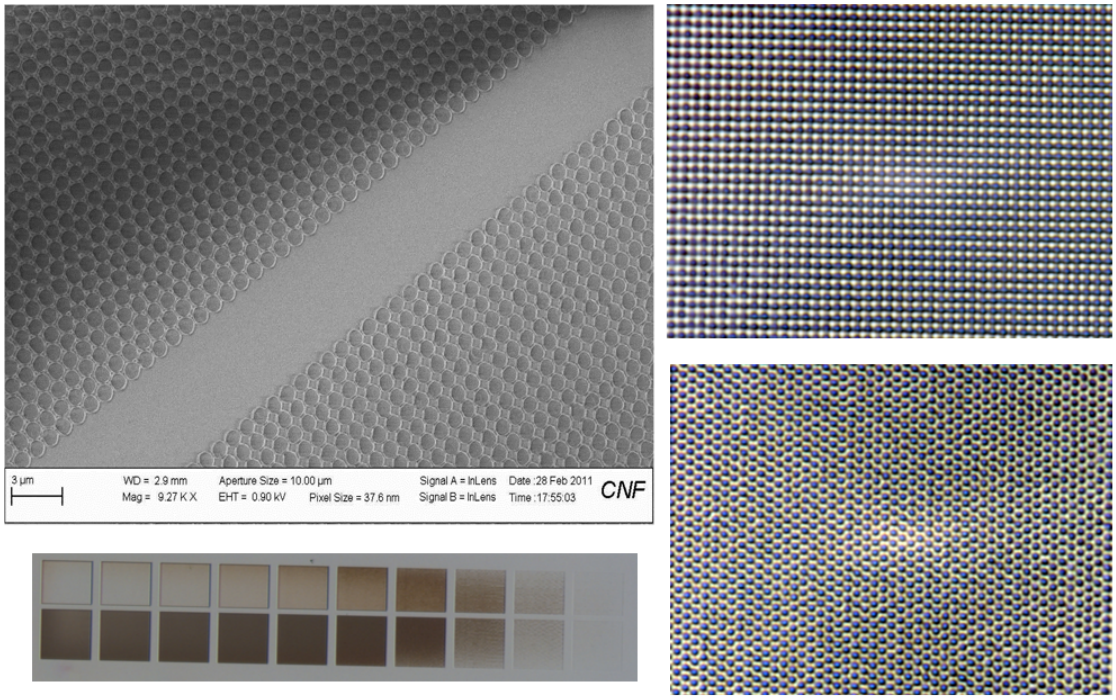

Figure 5.12: Successful results of new cleanroom process. LEFT: SEM image of triangular and square lattices made from altered E-Beam lithography recipe that adds a conducting layer onto the PMMA layer. RIGHT,TOP: Optical image of square lattice. RIGHT,BOTTOM: Optical image of triangular lattice. LEFT,BOTTOM: Dosage sweep over the same parameters used in Figure 5.10. Notice the absence of arcing damage in the patterned regions.

5.4 Conclusion

The melting rate of different facets of a colloidal crystal, where bonds extend only as far as a particle's nearest neighbors, and bond strengths are comparable to k_BT, is likely governed by the average time it takes a detaching particle to diffuse to a new lattice site so long as the weakest bound particles in both crystals have equal bond energies.

An excellent next direction for this project would be to use the theoretical

arguments provided in Section 5.2 and modified lithography recipe in Section 5.3.3 to predict the effect of moderate strain on the melting rates of crystals. Furthermore, the ratio of melting times expressed in Equation 5.5 only considers the initial movement of a particle from a corner site. The melting time of the entire face would also depend on the configuration of particles near the edges of the crystal. Particles that have not yet diffused away from adjacent interstitials would effectively act to cage particles attempting to leave the crystal. Simulations on the melting of an entire face of these colloidal crystals would allow us to explore the variance in melting behavior due to these secondary effects. Overall, this work holds the promise of opening up techniques for controlling the self-assembly of colloidal crystals via controlling a particle's available diffusive path lengths (for example, through local strain of the lattice).

CHAPTER 6

CONCLUSION

"Colloids as a model system" is a phrase not all that uncommonly used to describe the ability of microparticle suspensions and sediments to be used as an analog for atomic or nanoscale systems. In the preceding chapters, I have described two experiments that have interesting results because of the relatively long diffusion times that are inherently present in systems of colloidal microparticles. In Chapter 4, I described an experiment that identifies size-mismatching paired with unequal interaction strengths between particle sizes as a potential route to catalysis of multilayer crystal growth in colloidal systems with weak, short-ranged interactions. Chapter 5 documents an experiment that has yet to be published that finds counter-intuitive results for the rate of melting of crystals with different crystal face symmetries, whereby the more dense triangle-symmetric arrangement of particles melts significantly faster than those with square symmetry. Although it certainly would be interesting to measure these effects in smaller-scale counterparts, a direct connection between the dynamics of the disparately-sized systems would be icing on the cake, so to speak. The fact that these results are interesting or counter-intuitive means that there is plenty of fundamental physics to be explored in these systems.

The melting rate of different crystal faces should be dependent on the chemical potential of the system. Can we run another round of experiments where we control the chemical potential of the system and record melting and freezing rates of these square and triangular lattices? How does this change the result we found previously? Could we run these experiments on strained substrates with the intent of facilitating melting from a particular edge of the crystal?

We have a highly temperature-sensitive interaction that essentially leaves the energy of the thermal bath constant but increases the strength of the attraction between particles as temperature increases. Can we use this to our advantage and run experiments on the annealing of colloidal crystals? How does this change the growth or melting rates on patterned substrates, or the quality of crystals? Can this method be used to grow multilayer crystals without the presence of a large number of sedimenting particles, or as we recently found, without the presence of larger particles?

In bidisperse samples of crystallizing microparticles, frustrated clusters of mixed large and small particles persist for hundreds of minutes. In the absence of large particles, these amorphous clusters do not exist for long periods of time unless the attractive interaction between particles is so large that particles begin to aggregate. At this point, they are arrested and no longer fluid. Can we measure the free energy of these amorphous fluid clusters over time? How, exactly, does the presence of large particles help to promote particles into the gas from the sample substrate and from crystal edges? Could we use total internal reflection microscopy to investigate the substrate detachment rate of particles in the presence and absence of large particles? Is the amorphous cluster near a crystal edge a requirement for particle promotion, or is the presence of a large particle enough?

The answer to all of these questions is currently ”we don’t know.” However, with the changes made to the experimental system, techniques, featuring improvements, and insights gained from simulation, these questions are well within reach of the next round of experiments. I am excited to see the directions that this system is taken in the future.

APPENDIX A

APPENDIX: CODE SNIPPETS

A.1 Fast Pair Correlation Function, g(r)

As discussed in Section 3.2, here is a short Matlab function that quickly measures the relative conditional probability of finding a particle at distance r, conditional on a particle existing at the chosen reference location. The probability is relative to that of an ideal gas, making this a computation of $g(r)$, the pair correlation function.

This code computes $g(r)$ accurately inside the boundaries of `rMax`. That being said, if `rMax` is made to be very large, such as half of the sample size, very few particles will be able to serve as origins for the $g(r)$ calculation, which ruins the statistics. A good rule of thumb is to make `rMax` slightly larger as the distance you are interested in, which will maximize the number of particles that can serve as an origin for the calculation.

```
function gOfR = makePairCorrelation(xy,rMax,dr,sampleArea)
% Generate the pair correlation function g(r) for XY data
%
% INPUTS:
% xy:   N-by-2 matrix of [x,y] positions
% rMax: Max distance from reference particle to consider.  Also sets
%       the size of the inner box such that
%           innerBoxX = [0+rMax,boxXMax-rMax]
%           innerBoxY = [0+rMax,boxYMax-rMax]
%
% dr: distance step size
% sampleArea: (optional) Alter the sample space.  By default,
```

```
13 %             this is set to be bound by [0,0] and [max(x), max(y)].
14 %             Using the image size is a good idea.
15 %
16 % Distances are measured in pixels.
17
18 if nargin < 4,
19     sampleArea(2) = max(xy(:,1));
20     sampleArea(1) = max(xy(:,2));
21 end
22
23 boxXMax = sampleArea(2);
24 boxYMax = sampleArea(1);
25 tic;
26
27 % Mark the particles inside the inner box.
28 % Reference particles may only be chosen from here.
29 innerX = ((xy(:,1)>=rMax) & (xy(:,1) <= (boxXMax-rMax)));
30 innerY = ((xy(:,2)>=rMax) & (xy(:,2) <= (boxYMax-rMax)));
31 innerXY = innerX & innerY;
32
33 nRef = sum(innerXY);
34 binRanges = 0:dr:rMax;
35 binRangesSq = binRanges.^2;
36
37 dSqMat = math.distanceMatrix(xy(:,1),xy(:,2),false).^2;
38 dSqMat(dSqMat==0)=Inf;  % fix the diagonal
39 dSqReference = dSqMat(innerXY,:);
40
41 % Use only the inner particles as origins
42 % Count up the particles in each distance range.
43 binResults = histcounts(sqrt(dSqReference(:)),binRanges);
44 density = size(xy,1)/boxXMax/boxYMax;
```

```
45 area = pi*diff(binRangesSq);
46 gOfR = binResults./(nRef*area*density);
47 toc;
48
49 end
```

A.2 Fast Orientational Order Parameter, ψ_6

See Section 3.2.2 for a complete discussion of the code. Note that this function requires the input of a connectivity matrix `connMat` and a matrix of angles `angleMat`. Code for these are also reproduced in the code Appendix.

```
function [ p6 ] = psi6( connMat, angleMat )
%PSI6 Compute the value of Psi6 for each particle
% Given a connectivity matrix and angle matrix, compute Psi6 for each
% particle.  Note that a particle with less than two neighbors is
% defined to have a psi6 value of 0.

angles = angleMat;
angles(~connMat) = 0;
angles(connMat) = exp(6i*angles(connMat));

numNN = sum(connMat);
p6  = abs(sum(angles)./numNN)';
p6(numNN < 2) = 0;

end
```

A.3 Distance Matrix

Computing a matrix of distances between particles,

$$D = |(\mathbf{r}_1 - \mathbf{r}_2)|,$$

starts to take a decent chunk of time in experiments that involve many thousands of particles. In the case where we have approximately 5000 particles in two dimensions, poorly vectorized code takes about 1.5 seconds to run. Vectorized code runs in about 1.1 seconds. Offloading the computation onto the GPU results in a run time of about 0.4 seconds[1].

While the absolute difference in run times is small for this single function, it is used at least twice per frame in video analysis, one time for each layer. Videos consist of on the order of 10^3 frames. Simulations must call the distance functions multiple times for iterations on generated particle positions. The 375% speed-up on a computation that takes $O(1\text{ s})$ saves quite a bit of time.

```
1  function [ dMat , angles ] = distanceMatrix(x,y,b_angle)
2  %DISTANCEMATRIX Compute distance and angles between all x,y points.
3  %  This function assumes that x and y are vectors of x and y values
4  %  only.  However, if x and y are matrices of XY values (two-column),
5  %  this function  will pass the inputs on to math.asymDistanceMatrix.
6
7  if nargin < 3, b_angle=false; end
8
9  nParticles = length(x);
10
11 if (size(x,2) == 2 && size(y,2)==2)
12     [dMat,angles] = math.asymDistanceMatrix(x,y,b_angle);
```

[1]Measured on an AMD Ryzen 7 8-core (16 logical) CPU @ 4.0 GHz with a GeForce 1070 GPU

```
13      return;
14  end
15
16  % generate X and Y value grid
17  xmat = repmat(gpuArray(x),[1 nParticles]);
18  ymat = repmat(gpuArray(y),[1 nParticles]);
19
20  % compute deltaX, deltaY for all combinations of particles
21  dxmat = (xmat - xmat');
22  dymat = (ymat - ymat');
23
24  % compute squared distance between particles
25  dMat = gather(sqrt(dxmat.^2+dymat.^2));
26
27  % compute the angles between particles as well if called for.
28  if (b_angle==true)
29      angles = gather(atan2(dymat,dxmat));
30  end
31
32  end
```

A.4 Connectivity Matrix

The following function Matlab code to compute a connectivity matrix, as discussed in Section 3.2.2. This is ultimately included for completeness, as it is required for computing ψ_6.

```
function [ connMatrix ] = connMatrix( distanceMatrix, cutoff )
%CONNMATRIX Creates a connectivity matrix from a distance matrx
%  Using a provided distanceMatrix and a cutoff, output a
%  connectivity matrix.

connMatrix = distanceMatrix < cutoff;

% remove particles being connected with themselves
connMatrix = connMatrix & ~eye(size(connMatrix));

end
```

BIBLIOGRAPHY

[1] Bruce J. Ackerson and P. N. Pusey. Shear-induced order in suspensions of hard spheres. *Physical Review Letters*, 61:1033–1036, 1988.

[2] Sean B. Andersson. Localization of a fluorescent source without numerical fitting. *Optics Express*, 16(23):18714–18742, November 2008.

[3] Stephen M. Anthony and Steve Granick. Image analysis with rapid and accurate two-dimensional gaussian fitting. *Langmuir*, 25:8152–8160, 2009.

[4] Sho Asakura and Fumio Oosawa. Interaction between particles suspended in solutions of macromolecules. *Journal of Polymer Science*, 33(126):183–192, 1958.

[5] Stefan Auer and Daan Frenkel. Prediction of absolute crystal-nucleation rate in hard-sphere colloids. *Nature*, 409(6823):1020–1023, 2001.

[6] Jillian F. Banfield, Susan A. Welch, Hengzhong Zhang, Tamara Thomsen Ebert, and R. Lee Penn. Aggregation-based crystal growth and microstructure development in natural iron oxyhydroxide biomineralization products. *Science*, 289(5480):751–754, 2000.

[7] Jens Baumgartner, Archan Dey, Paul H. H. Bomans, Cécile Le Coadou, Peter Fratzl, Nico A. J. M. Sommerdijk, and Damien Faivre. Nucleation and growth of magnetite from solution. *Nature Materials*, 12(4):310–314, 2013.

[8] Matthew Bierbaum, Brian D. Leahy, Alexander A. Alemi, Itai Cohen, and James P. Sethna. Light microscopy at maximal precision. *Physical Review X*, in press, accepted August 2017.

[9] Daniel Blair and Eric Dufresne. *The Matlab Particle Tracking Code Repository*, 2005. http://site.physics.georgetown.edu/matlab/.

[10] Robert Brown. A brief account of microscopical observations made in the months of june, july, and august 1827 on the particles contained in the pollen of plants and on the general existence of active molecules in organic and inorganic bodies. *The Miscellaneous Botanical Works of Robert Brown*, 1, 1828.

[11] Sung-yoon Chung, Young-min Kim, Jin-gyu Kim, and Youn-joong Kim.

Multiphase transformation and ostwald's rule of stages during crystallization of a metal phosphate. *Nature Physics*, 5(1):68–73, 2009.

[12] J. S. Clunie, J. F. Goodman, and P. C. Symons. Phase equilibria of dodecylhexaoxyethylene glycol monoether in water. *Transactions of the Faraday Society*, 65:287–296, 1968.

[13] Megan Louise Mergo (Comins). *Planet Migration Around Young Magnetized Stars*. Ph.D. dissertation, Cornell University, 2015.

[14] Michael Connolly. Computation of molecular volume. *Journal of the American Chemical Society*, 107:1118–1124, 1985.

[15] John Crocker and Eric Weeks. *Particle Tracking Using IDL*. http://www.physics.emory.edu/faculty/weeks/idl/.

[16] John C. Crocker and David G. Grier. Methods of digital video microscopy for colloidal studies. *Journal of Colloid and Interface Science*, 179(1):298–310, 1996.

[17] Cleocir José Dalmaschio, Caue Ribeiro, and Edson Roberto Leite. Impact of the colloidal state on the oriented attachment growth mechanism. *Nanoscale*, 2:2336–2345, 2010.

[18] James J. De Yoreo, Pupa U. P. A. Gilbert, Nico A. J. M. Sommerdijk, R. Lee Penn, Stephen Whitelam, Derk Joester, Hengzhong Zhang, Jeffrey D. Rimer, Alexandra Navrotsky, Jillian F. Banfield, Adam F. Wallace, F. Marc Michel, Fiona C. Meldrum, Helmut Cölfen, and Patricia M. Dove. Crystallization by particle attachment in synthetic, biogenic, and geologic environments. *Science*, 349(6247):aaa6760, 2015.

[19] A.D. Dinsmore and P.B. Warren. Fluid-solid transitions on walls in binary hard-sphere mixtures. *EPL (Europhysics Letters)*, 40(3):337, 1997.

[20] Albert Einstein. Über die von der molekularkinetischen theorie der wärme geforderte bewegung von in ruhenden flüssigkeiten suspendierten teilchen. *Annalen der Physik*, 1905.

[21] L. Filion, M. Hermes, R. Ni, and M. Dijkstra. Crystal nucleation of hard spheres using molecular dynamics, umbrella sampling, and forward flux sampling: A comparison of simulation techniques. *The Journal of Chemical Physics*, 133(24):244115, 2010.

[22] Rajesh Ganapathy, Mark R. Buckley, Sharon J. Gerbode, and Itai Cohen. Direct measurements of island growth and step-edge barriers in colloidal epitaxy. *Science*, 327(5964):445–448, 2010.

[23] Yongxiang Gao and Maria Kilfoil. Accurate detection and complete tracking of large populations of features in three dimensions. *Optics Express*, 17(6):4685–4704, 2009.

[24] U. Gasser. Crystallization in three- and two-dimensional colloidal suspensions. *Journal of Physics: Condensed Matter*, 21(20):203101, 2009.

[25] Denis Gebauer, Antje Völkel, and Helmut Cölfen. Stable prenucleation calcium carbonate clusters. *Science*, 322(5909):1819–1822, 2008.

[26] Sharon Jane Gerbode. *Colloidal Crystals: Structure, Dynamics, and the Importance of Dimer Bonds*. Ph.D. dissertation, Cornell University, 2010.

[27] David G. Grier and Sven H. Behrens. The charge of glass and silica surfaces. *The Journal of Chemical Physics*, 115:6716–6721.

[28] Frederik Grüll, Manfred Kirchgessner, Rainer Kaufmann, and U. Kebschull. Accelerating image analysis for localization microscopy with fpgas. *2011 International Conference on Field Programmable Logic and Applications*, pages 1–5, September 2011.

[29] P. Anne Hiltner and Irvin M. Krieger. Diffraction of light by ordered suspensions. *The Journal of Physical Chemistry*, 73(7):2386–2389, 1969.

[30] Krister Holmberg, Bo Jönsson, Bengt Kronberg, and Björn Lindman. *Surfactants and Polymers in Aqueous Solution*. John Wiley & Sons, 2nd edition, 2003.

[31] Ian Hosein. *Particle Point Analysis*. Work done in Liddell Group at Cornell University, modifying Maria Kilfoil's code. Code can be found at https://www.mathworks.com/matlabcentral/fileexchange/42573-particle-point-analysis.

[32] Ian D Hosein and Chekesha M. Liddell. Convectively assembled nonspherical mushroom cap-based colloidal crystals. *Langmuir*, pages 8810–8814., 2007.

[33] V. K. Ivanov, P. P. Federov, A. Ye. Baranchikov, and V. V. Osiko. Oriented

attachment of particles: 100 years of investigations of non-classical crystal growth. *Russian Chemical Reviews*, 83(12):1204–1222, 2014.

[34] P. Kekicheff, C. Grabielle-Madelmont, and M. Ollivon. Phase diagram of sodium dodecyl sulfate-water system: 1. a calorimetric study. *Journal of Colloid and Interface Science*, 131:112–132, 1989.

[35] Christopher E. Killian, Rebecca A. Metzler, Y. U. T. Gong, Ian C. Olson, Joanna Aizenberg, Yael Politi, Fred H. Wilt, Andreas Scholl, Anthony Young, Andrew Doran, Martin Kunz, Nobumichi Tamura, Susan N. Coppersmith, and P. U. P. A. Gilbert. Mechanism of calcite co-orientation in the sea urchin tooth. *Journal of the American Chemical Society*, 131(51):18404–18409, 2009.

[36] Amy E. Larsen and David G. Grier. Melting of metastable crystallites in charge-stabilized colloidal suspensions. *Physical Review Letters*, 76:3862–3865, 1996.

[37] Robert G. Laughlin. *The Aqueous Phase Behavior of Surfactants*. Academic Press, 1996.

[38] Wolfgang Lechner, Christoph Dellago, and Peter G. Bolhuis. Role of the prestructured surface cloud in crystal nucleation. *Physical Review Letters*, 106:085701, 2011.

[39] Henk N. W. Lekkerkerker and Remco Tuinier. *Colloids and the Depletion Interaction*. Springer, Dordrecht, the Netherlands, 2011.

[40] Georg Christoph Lichtenberg. *De Nova Methodo Naturam Ac Motum Fluidi Electrici Investigandi*. 1777.

[41] Neil Y. C. Lin and Itai Cohen. Relating microstructure and particle-level stress in colloidal crystals under increased confinement. *Soft Matter*, 12:9058–9067, 2016.

[42] Peter J. Lu. *Gelation and Phase Separation of Attractive Colloids*. PhD thesis, Harvard University, 2008.

[43] Peter J. Lu, Peter A. Sims, Hidekazu Oki, James B. Macarthur, and David A. Weitz. Target-locking acquisition with real-time confocal (tarc) microscopy. *Optics Express*, 15:8702–8712, 2007.

[44] Xiang Ma, Shuai Zhang, Fang Jiao, Christina J. Newcomb, Yuliang Zhang, Arushi Prakash, Zhihao Liao, Marcel D. Baer, Christopher J. Mundy, James Pfaendtner, Aleksandr Noy, Chun-Long Chen, and James J. De Yoreo. Tuning crystallization pathways through sequence engineering of biomimetic polymers. *Nature Materials*, 16(7):767–774, 2017.

[45] Dominique Maes, Maria A. Vorontsova, Marco A. C. Potenza, Tiziano Sanvito, Mike Sleutel, Marzio Giglio, and Peter G. Vekilov. Do protein crystals nucleate within dense liquid clusters? *"Acta Crystallographica Section F*, 71(7):815–822, 2015.

[46] Julia Mahamid, Amnon Sharir, Lia Addadi, and Steve Weiner. Amorphous calcium phosphate is a major component of the forming fin bones of zebrafish: Indications for an amorphous precursor phase. *Proceedings of the National Academy of Sciences*, 105(35):12748–12753, 2008.

[47] David R. Nelson and B. J. Halperin. Solid and fluid phases in smectic layers with tilted molecules. *Physical Review B*, 21(11), June 1980.

[48] Thomas Palberg. Crystallization kinetics of colloidal model suspensions: recent achievements and new perspectives. *Journal of Physics: Condensed Matter*, 26(33):333101, 2014.

[49] Raghuveer Parthasarathy. Rapid, accurate particle tracking by calculation of radial symmetry centers. *Nature Methods*, 9(7):724–726, July 2012.

[50] R. Pavani and G. Ranghino. A method to compute the volume of a molecule. *Computational Chemistry*, 6:133–135, 1982.

[51] Vincent Pelletier, Naama Gal, Paul Fournier, , and Maria L. Kilfoil. Microrheology of microtubule solutions and actin-microtubule composite networks. *Physical Review Letters*, 102:188303–1–4.

[52] Yael Politi, Talmon Arad, Eugenia Klein, Steve Weiner, and Lia Addadi. Sea urchin spine calcite forms via a transient amorphous calcium carbonate phase. *Science*, 306(5699):1161–1164, 2004.

[53] P. N. Pusey and W. van Megen. Phase behaviour of concentrated suspensions of nearly hard colloidal spheres. *Nature*, 320(6060):340–342, 1986.

[54] S. Redner. *A Guide to First Passage Processes.* Cambridge University Press, 2001.

[55] Erin K. Riley and Chekesha M. Liddell. Confinement-controlled self assembly of colloids with simultaneous isotropic and anisotropic cross-section. *Langmuir*, 26:11648–11656.

[56] Salman S Rogers, Thomas A Waigh, Xiubo Zhao, and Jian R Lu. Precise particle tracking against a complicated background: polynomial fitting with gaussian weight. *Physical Biology*, 4:220–227, 2007.

[57] Matteo Salvalaglio, Claudio Perego, Federico Giberti, Marco Mazzotti, and Michele Parrinello. Molecular-dynamics simulations of urea nucleation from aqueous solution. *Proceedings of the National Academy of Sciences*, 112(1):E6–E14, 2015.

[58] J. R. Savage, D. W. Blair, A. J. Levine, R. A. Guyer, and A. D. Dinsmore. Imaging the sublimation dynamics of colloidal crystallites. *Science*, 314(5800):795–798, 2006.

[59] J. R. Savage and A. D. Dinsmore. Experimental evidence for two-step nucleation in colloidal crystallization. *Physical Review Letters*, 102:198302, 2009.

[60] John R. Savage, Stefan F. Hopp, Rajesh Ganapathy, Sharon J. Gerbode, Andreas Heuer, and Itai Cohen. Entropy-driven crystal formation on highly strained substrates. *Proceedings of the National Academy of Sciences*, 110(23):9301–9304, 2013.

[61] Peter Schall, Itai Cohen, David A. Weitz, and Frans Spaepen. Visualizing dislocation nucleation by indenting colloidal crystals. *Nature*, 440(7082):319–323, 2006.

[62] M. Schmidt and H. Lowen. Phase diagram of hard spheres confined between two parallel plates. *Physical Review E.*, 55:7228–7241, 1997.

[63] Carlas S. Smith, Nikolai Joseph, Bernd Rieger, and Keith A Lidke. Fast, single-molecule localization that achieves theoretically minimum uncertainty. *Nature Methods*, 7:373–375, 2010.

[64] M. M. Smoluchowshi. Sur le chemin moyen parcouru par les molécules d'un gaz et sur son rapport avec la théorie de la diffusion. *Bulletin International de l'Académie des Sciences de Cracovie*, 1906.

[65] Paul J. Steinhardt, David R. Nelson, and Marco Ronchetti. Icosahedral

bond orientation order in supercooled liquids. *Physical Review Letters*, 47(18), November 1981.

[66] Peter G. Vekilov. The two-step mechanism of nucleation of crystals in solution. *Nanoscale*, 2:2346–2357, 2010.

[67] Peter G. Vekilov and Maria A. Vorontsova. Nucleation precursors in protein crystallization. *Acta Crystallographica Section F*, 70(3):271–282, 2014.

[68] Yufeng Wang, Yu Wang, Dana R. Breed, Vinothan N. Manoharan, Lang Feng, Andrew D. Hollingsworth, Marcus Weck, and David J. Pine. Colloids with valence and specific directional bonding. *Nature*, 491(7422):51–55, 2012.

[69] Aaron L. Washington, Megan E. Foley, Soshan Cheong, Lieth Quffa, Christopher J. Breshike, John Watt, Richard D. Tilley, and Geoffrey F. Strouse. Ostwalds rule of stages and its role in cdse quantum dot crystallization. *Journal of the American Chemical Society*, 134(41):17046–17052, 2012.

[70] Steve Weiner and Lia Addadi. Crystallization pathways in biomineralization. *Annual Review of Materials Research*, 41(1):21–40, 2011.

[71] Ingrid Maria Weiss, Noreen Tuross, Lia Addadi, and Steve Weiner. Mollusc larval shell formation: Amorphous calcium carbonate is a precursor phase for aragonite. *Journal of Experimental Zoology*, 293(5):478–491, 2002.